# NMR studies on bulk Fe3O4 and electrodeposited Co/Cu multilayers

Colaris, A.H.J.

*Award date:*
1996

Eindhoven University of Technology
Department of Physics
Group Cooperative Phenomena

# NMR studies on bulk $Fe_3O_4$ and electrodeposited Co/Cu multilayers

*André H.J. Colaris*

August 1995

Report of a graduation research project carried out in the group Cooperative Phenomena at Eindhoven University of Technology. This research project is part of a collaboration of this group and Philips Research Laboratories Eindhoven.

Supervisor : *Ir. E.A.M. van Alphen*

Professor : *Prof. Dr. Ir. W.J.M. de Jonge*

# Abstract

*Nuclear Magnetic Resonance* (NMR) is an elegant method in obtaining information about the environment which confine atoms to resonate at specific hyperfine field values: a local probe succesfully used in solids during the last 50 years. Two current topics were studied: $^{57}$Fe NMR on magnetite ($Fe_3O_4$), preceded by a literature review, and $^{59}$Co NMR on electrochemically deposited Co/Cu multilayers and Co films.

Two magnetite samples are investigated: a non-stoichiometric, single crystal $Fe_3O_4$ cylinder and a thin film of 1150 Å $Fe_3O_4$ molecular beam epitaxy (MBE) grown on a MgO(100) substrate. NMR spectra are measured at room temperature and at 1.6 K by frequency scans in zero-field. At room temperature magnetite possesses a cubic inverse spinel structure with two equivalent A sites and four equivalent B sites per unit cell. The NMR spectrum of the cylinder showed a spin-echo intensity between 67.5 and 68 MHz due to the A sites and between 62 and 64 MHz two resonance lines due to the B sites. When magnetite is cooled, it undergoes at the so-called Verwey temperature $T_V$ ($\simeq$ 120 K) a metal-insulator transition causing the crystal symmetry to change from cubic to orthorhombic. At 1.6 K the cylinder showed a NMR spectrum with several A site lines between 69 and 71 MHz and B site lines spread over a frequency range from 68 to 75 MHz. The detection limit was reached in case of the thin film at 1.6 K due to the small amount of $Fe^{57}$. The $Fe_3O_4$ volume of the thin film is $2.2 \times 10^4$ times smaller than the volume of the cylinder.

Electrodeposition got itself a renewed interest as serious alternative for more conventional growing methods as sputtering and MBE due to its relative simplicity, improved accuracy, and low costs. Structural characteristics of electrodeposited Co films, several series of Co/Cu multilayers, and the influence of leveling agents on the nanostructure were studied by NMR. The experiments were performed with an applied field.

NMR spectra of Co films, varying in base layer (200 Å Cu or 500 Å Au), thickness (1000 Å or 7000 Å), and electrolyte composition (only $Co^{2+}$ ions or both $Co^{2+}$ and $Cu^{2+}$ ions), were obtained. The 7000 Å Co film grown on the Cu base layer (compared to the similar Co film grown on the Au base layer) showed the best structurally defined results: the smallest width of the fcc main line, the least hcp and stacking faults (sf), and a distinction of the first four satellite lines having an average distance $\Delta(\text{sat}) = 1.20 \pm 0.09$ T. The resonance lines of the 1000 Å Co film were less structurally informative by having

unexplainably larger line widths and no distinguishable satellites. A probable base layer dependency of the strain was detected, for both Co films grown in a Co bath and Co films grown in a Co-Cu bath having an Au base layer (compared to the films grown on a Cu base layer) caused a relative shift in the NMR spectra of 0.08 T towards lower hyperfine field.

Three Co/Cu multilayer series were studied: [111] and [100] textured with varying Co layer thickness $t_{Co}$ and [100] textured with varying Cu layer thickness $t_{Cu}$. For the [100] series with varying $t_{Co}$ the width of the main line decreased with increasing $t_{Co}/t_{Cu}$ ratio, while in case of the [100] textured series with varying $t_{Cu}$ the width increased with increasing $t_{Co}/t_{Cu}$ ratio. The [111] textured series had a fcc main line width which was approximately constant. The Co/Cu [100] multilayers showed an asymmetry in the main line resonance peak, probably due to the spin-echo intensity arising from the next nearest neighbour atoms. The relative amount of the fcc structure is dependent upon the $t_{Co}/t_{Cu}$ ratio in case of the [111] textured Co/Cu multilayer with varying $t_{Co}$ and the [100] textured Co/Cu multilayer with varying $t_{Cu}$, while the [100] textured Co/Cu multilayer with varying $t_{Co}$ is not dependent on this ratio. $\Delta$(sat) for the Co/Cu [100] series (1.15$\pm$0.05 T) differs from the [111] textured series (1.54$\pm$0.03 T). The first value is in accordance with the value found for electrodeposited Co-Cu alloys (Co films grown in a Co-Cu bath), while the latter value is in accordance with the literature values of Co/Cu [111] multilayers. The difference of $\Delta$(sat) between [100] and [111] textured Co/Cu multilayers is not understood. The interface roughness was independent of the just-mentioned textures and has a value of 5$\pm$1 Å Co attributed to two interface layers.

The use of leveling agents during growth (triton-X100 and thiourea were used as additives) caused a lowering of the magnetoresistance (from values of at least 3% to less than 1%), a huge disimprovement of the bulk structure (triton-X100 caused the largest relative amount of hcp and sf), and a much larger interface roughness. The interfacial spin-echo intensity of the thiourea treated multilayer was two times larger than the interfacial part of the NMR spectrum of a similar multilayer without leveling agent treatment.

# Contents

# Chapter 1

# Introduction

Within the group Cooperative Phenomena of the Eindhoven University of Technology (EUT) some of the current research is related to studies of the magnetic and structural properties of magnetic thin films and magnetic multilayers. This research has been (and still is) carried out in collaboration with Philips Research Laboratories Eindhoven. One of the aims is to understand and improve magnetic reading and writing (playing and recording) in order to use this way of storing data in current applied technology.

One does not doubt if magnetic materials play a crucial role in modern life, for magnetic materials are all around us. Permanent magnets drive the electric motors in all electrical appliances; transformers use magnetic cores to convert mains electricity to the exact requirements of electronic systems; and magnetic yokes steer the electron beam in the cathode ray display tubes of televisions and computer monitors. But the most far reaching property of magnetic materials has been their ability to store data on rigid and flexible disks for computer data, tapes for audio and video software, and magnetic strips on credit cards for personal data. This storage ability and its capacity caused indirectly the start of a new information age which could be considered as revolutionary as the invention of typography.

There are two possibilities in storing data magnetically: inductive magnetic recording and magneto-optic recording. We will limit ourselves in dealing only with the first method. Two items are essential in the inductive magnetic storage of data: (1) the recording medium which has to act as a *memory* and which will store information, and (2) the *sensor* (magnetic head) which enables one to write and read this stored information, see also figure 1.1. Head and medium are magnetically completely different. The head consists of soft magnetic material (figure 1.2a) while the medium is composed of some hard magnetic material (figure 1.2b). The head's material will show a small hysteresis and a large permeability. The sensitivity of the total will increase with decreasing coercivity $H_c$ of the storage medium. This coercivity is a threshold value above which the applied field has to be in order to change the magnetization in the storage medium. This medium, in contrast with the head, is made of hard magnetic material, for once a signal is recorded it has to stay clearly detectable, so a large remanence $M_r$ is prefered.

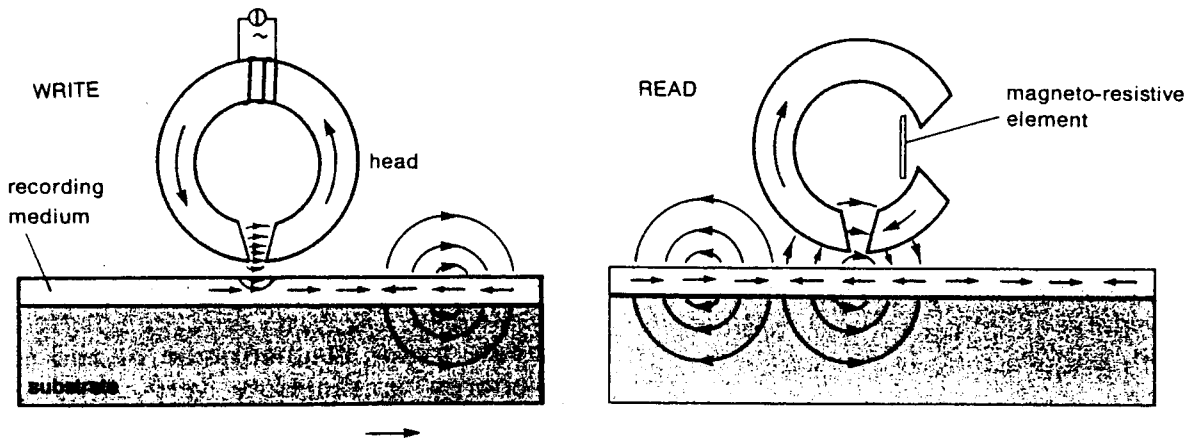


Figure 1.1: *The basic principles of writing and reading information in longitudinal inductive magnetic recording* [Smi92]. *The figures show the magnetization vectors in the recording medium. These vectors are parallel to the medium's plane and currents of field are used to* **write** *information. The fields are induced by pulses of currents in the coil surrounding the cylindrical part of the head. Information can also be* **read** *from current pulses or changes of resistance induced in the head.*

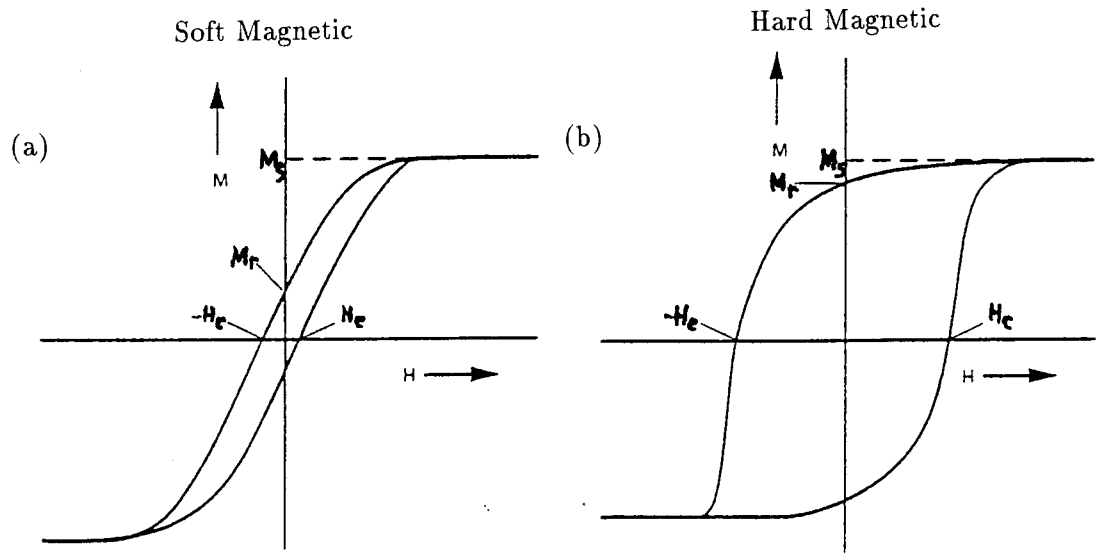


Figure 1.2: *(a) shows the characteristic M versus H curve for soft magnetic materials while (b) shows the same curve for hard magnetic materials. The magnetization M increases with increasing field H until it will reach a certain maximum called saturation magnetization $M_s$. If one decreases now the field H, the magnetization will also decrease but non-proportional with this field. At $H = 0$ a certain magnetization $M_r$ will remain. To get a zero magnetization one has to implement a certain negative field called coercitive field $H_c$. Further enlargement of the applied field H will again cause saturation magnetization but now for the anti-parallel situation in regard to a positive field. Thus the relation between M and H is described by a hysteris.*

For recording applications magnetic thin films are preferred to bulk materials for two reasons: (1) they are easy to mass-process, and (2) their composition (and hence properties) can be easily controlled and optimized for particular applications. Multilayers are made up of a stacking of layers, sometimes up to a hundred times. The layers normally consist of a repetition of two different metallic elements, of which one or both are magnetic. The thickness of one layer varies from a few to many monolayers. Before growing a multilayer on a substrate, a baselayer is often grown on the substrate. This layer determines the growth structure and texture of the multilayer which is likely to influence magnetic properties. The top of the sample is often covered with a layer to prevent the multilayer from oxidation. Some 'conventional' methods for producing magnetic multilayers are high vacuum evaporation, sputtering, and molecular beam epitaxy (MBE). Recently electrochemical deposition (ED) is added to this list. ED as a growing method is not new, but it has gained accuracy, specifically in growing multilayers.

During the last 15 years some of the interesting topics, which are investigated in order to improve the (inductive magnetic and magneto-optic) recording of data, are *perpendicular magnetization*, *interlayer coupling*, and *giant magnetoresistance* (GMR). The just-mentioned topics will be dealt with by discussing in the now following paragraphs data recording, coupling interactions in multilayers having alternating magnetic and non-magnetic layers, and GMR in Fe/Cr multilayers.

The present magnetic material in a video tape or a floppy disc consists of small magnetic particles ($\gamma$-$Fe_2O_3$ or $CrO_2$). These magnetic particles which are about 0.2 $\mu$m in length, are disperged in a thin (1-3 $\mu$m) coating which is deposited on a non-magnetic substrate [Lui93]. The magnetic particles posses magnetic moments causing a total magnetization parallel to the plane of the tape. This causes a large demagnetization field $H_d$ which will change the magnetization when it is larger than $H_c$ and this, among other properties, limits the maximum achievable storage capacity. In the early eighties discussions about gaining a higher storage capacity by *perpendicular* in stead of *parallel magnetization* got started. In this perpendicular situation like-poles belonging to different magnetized domains would not adjoin directly each other, and thus cause a sharper defined transition between those domains.

When a magnetic atom is placed in a non-magnetic host the magnetic moment of the magnetic atom, say cobalt, induces a polarization of the conduction electrons surrounding it. The spin of the conduction electrons oscillates rapidly between the majority spin ('spin up') and the minority spin ('spin down') with a characteristic wavelength $\lambda = \pi/k_F$ ($k_F$ is the wave vector at the spherical Fermi surface [Smi92]). A second magnetic atom will experience either a positive or a negative polarization field from the first atom; that is, the atoms will be respectively ferromagnetically or antiferromagnetically coupled. The strength of this so-called RKKY interaction is proportional to $d^{-3}$, where $d$ is the distance between the atoms. For magnetic multilayers, in which layers of magnetic atoms are separated by non-magnetic layers, one might expect a similar rapid oscillation between ferromagnetic and antiferromagnetic *coupling* as a function of the non-magnetic *interlayer* thickness. In this case the coupling should vary as $d^{-2}$ due to the pseudo-one-dimensional character of

the multilayers [Smi92].

Ferromagnetic coupling between magnetic layers is not easy to observe in M versus H loops as nothing significant happens when a magnetic field is applied. Ferromagnetic coupling can be quantified by ferromagnetic resonance (FMR). Antiferromagnetic coupling is easier to detect because for identical, alternatingly oppositely magnetised, magnetic layers the net moment would be zero! However, if an antiferromagnetically coupled film is placed in a sufficiently strong magnetic field the layers switch to the ferromagnetic orientation and the full magnetic moment is recovered. The strength of this so-called switching field is a measure for the antiferromagnetic coupling strength. In 1986 an antiferromagnetic coupling between layers of iron atoms was discovered in Fe/Cr multilayers [GSP+86]. Shortly after this discovery it was demonstrated that this coupling oscillates between ferromagnetic and antiferromagnetic as the thickness of the non-magnetic interlayers is increased [BBF+88]. Oscillating interlayer coupling was subsequently observed in many other multilayer systems and appeared to be a general property [PMR90]. Antiferromagnetic coupling is one of the ways to obtain an antiparallel orientation of the magnetic layers and thus making measurements of the change in electrical resistance between zero-field and large magnetic field. The relative change in this electric resistance is called *giant magnetoresistance* (115% at 4.2 K and 65% at room temperature for Co/Cu multilayers [PLS91]). Before this giant effect values of about 2% due to anisotropic magnetoresistance (AMR) were normal [Pri95]. The GMR-effect is based on the mechanism of spin dependent electron scattering in a multilayer, see also figure 1.3. In general, one can speak of two different kinds of scattering: scattering in the bulk and at the interface. In the just-cited figure only interface scattering is taken into account. Fe is ferromagnetic because the energy of the 'spin up' electrons is lower than that of the 'spin down' electrons. The 'spin down' bandstructure belonging to Fe is almost the same as the bandstructure of Cr in both kinds of spin. When following a 'spin down' electron passing all Fe/Cr bilayers, the electron will feel nearby both Fe and Cr atoms the same potential and thus will not scatter heavily at the interfaces. However, the 'spin up' electron will indeed feel the difference in potential, so extra scattering will be evident [Smi92]. More recent research projects study differences between current in plane (CIP) and current perpendicular to plane (CPP) GMR measurements [LSGdJ95] or the contributions of interface scattering (both theoretical [BF94] and experimental [SNG+93]) and bulk scattering to the GMR. The usual measurements of GMR with current flow in the layer planes have the advantage of being straight forward to make, but the disadvantage that it is difficult to separate and quantify bulk and interface scattering. In contrast, measurements with current flow perpendicular to the layer planes are more difficult to make, but can allow direct determination of the crucial bulk and interface parameters and cause in the case of Co/Cu multilayers a CPP-GMR of 170% [PLH+93] at liquid helium temperature. A recent review article dealing with most of the above-mentioned (and other) aspects in regard to *GMR in spin-valve multilayers* has been published by Dieny [Die94].

Beside information about magnetic properties of multilayers and other thin films one is also interested in the structural properties of those films, for the magnetic properties are tightly determined by the structural properties (of interface and of bulk). Thus, if one

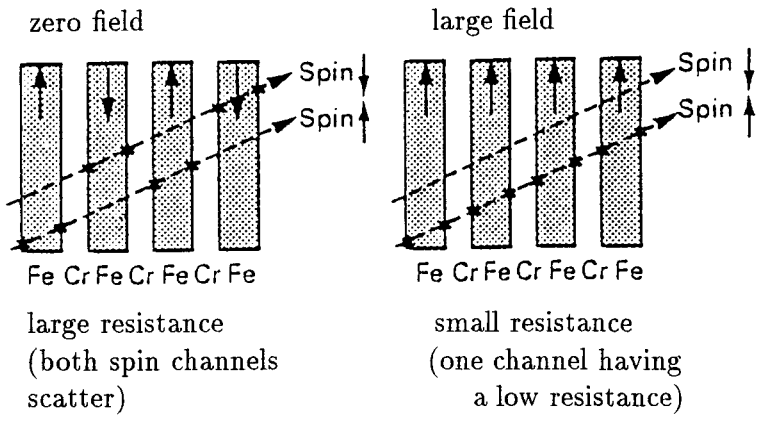


Figure 1.3: *Schematic presentation of a simple model of spin dependent scattering in a Fe/Cr multilayer* [Lui93]. *In zero external field the magnetic moments of the alternating Fe layers are antiparallel causing scattering in both spin channels and thus a large electric resistance. In large external field the magnetic moments of the same Fe layers are all parallel aligned causing scattering in only one channel and thus a small electric resistance.*

wants to optimize the magnetic properties, knowledge about the structural properties is indispensable. One example of such a relation is the interface roughness of a Ni-Fe/Cu multilayer [SNG+93] which influences the spin dependent scattering (and thus exerts influence on GMR). There are several methods of measuring structural properties, like X-Ray Diffraction (XRD), Transmission Electron Microscopy (TEM), and Conversion Electron Mössbauer Spectroscopy (CEMS). XRD might tell us more about the repetition of bilayers and lattice size in a multilayer structure. *Nuclear Magnetic Resonance* (NMR) is an elegant method to obtain more and/or exclusive information. NMR measures the hyperfine field and thus is an excellent example of a unique 'local probe measurement'.

The outline of this graduation report is as follows. Chapter two will treat with the different components of the hyperfine field, which is measured by NMR, and their relationship with the (atomic) local environment in a sample. In chapter three, the NMR experiment will be explained and the experimental setup will be described briefly.

Chapter four describes the findings of $^{57}$Fe NMR on bulk magnetite films, which are preceded by a NMR literature review, while chapter five shows results of $^{59}$Co NMR on electrodeposited thick Co films and Co/Cu multilayers.

# Chapter 2

# The hyperfine field

*With NMR the energy splitting, due to the total effective magnetic field at a nucleus, is measured. For magnetically ordered materials this magnetic field is generated by the interaction between nuclear and electronic magnetic moments. The first section of this chapter explains the energy splitting caused by the total magnetic field. Section 2.2 describes the fields, which contribute to the total field. Section 2.3 discusses the influence of the structure, strain and foreign neighbours on the hyperfine field. This chapter will end with section 2.4 which shortly deals with a new, more accurate manner of determinating the interface roughness.*

## 2.1 Interaction of the nuclear spin with the magnetic field at the nucleus

A nucleus possessing a magnetic moment experiences hyperfine interactions with the unpaired magnetic electrons in its surroundings. If a nucleus has a total spin angular-momentum $\vec{I}$, the magnetic moment $\vec{\mu}$ of the nucleus is related to the nucleus spin as:

$$\vec{\mu} = \hbar\gamma\vec{I} \tag{2.1}$$

with $\gamma$ the nuclear gyromagnetic ratio. The interaction between this moment and the total effective magnetic field $\vec{B}_{tot}$ at the nucleus is given by the Zeeman Hamiltonian ($\mathcal{H}_z$):

$$\mathcal{H}_z = -\vec{\mu} \cdot \vec{B}_{tot} \tag{2.2}$$

The contributions to the total field $\vec{B}_{tot}$ are:

$$\vec{B}_{tot} = \vec{B}'_{hf} + \vec{B}_{dip} + \vec{B}_{appl} + \vec{B}_{ind} \tag{2.3}$$

with the hyperfine field $\vec{B}'_{hf}$, the dipolar field $\vec{B}_{dip}$, $\vec{B}_{appl}$ being the external applied field, and $\vec{B}_{ind}$ being the induced field, which is caused by the applied field. Since in solids the flipping time for the electronic spin moment is usually very short compared to the time the nuclear spin would need for one Larmor precession, the nucleus normally "feels" an averaged or effective value of the total spin of the ion or atom. In magnetically ordered materials this average value deviates significantly from zero, and thus cannot be neglected, e.g. for $^{59}$Co and $^{57}$Fe, due to the fixation of the (relative) direction of the magnetic moments by the exchange interactions. $\vec{B}'_{hf}$ may attend values between 1 T and 100 T [dG93]. This implies that the just-mentioned induced field for magnetically ordered materials may, in general, be neglected since its contribution to the below-mentioned nuclear energy level Zeeman splitting is at least two or three orders of magnitude smaller than that of the other terms. These other contributions to $\vec{B}_{tot}$ will be discussed in the next section. The Zeeman Hamiltonian leads to the following energy splitting $\Delta E$ of:

$$\Delta E = hf = \hbar\gamma|\vec{B}'_{hf} + \vec{B}_{dip} + \vec{B}_{appl}| \tag{2.4}$$

with $f$ the NMR resonance frequency.

For $^{57}$Fe $\gamma/(2\pi) = 1.381$ MHz/T [Pan86] and the magnitude of $\vec{B}_{tot}$, without an external applied field is about 50 T. For $^{59}$Co $\gamma/(2\pi) = 10.054$ MHz/T [WWJ67] and the magnitude of $\vec{B}_{tot}$, without an external applied field is about 20 T. This leads to a NMR resonance frequency for $^{57}$Fe in the order of 70 MHz and for $^{59}$Co in the order of 200 MHz.

So far, we have considered only the *magnetic* interactions of the nucleus with its surroundings. However, for nuclei with spin $I \neq \frac{1}{2}$ in a non-cubic environment also the interaction between the nuclear quadrupole moment and the electric field gradient, produced by the electron clouds, may contribute to the nuclear energy splitting.

A nucleus with spin greater than 1/2 (which is the case for $^{59}$Co, but not for $^{57}$Fe) possesses an electric quadrupole moment, which causes an additional Hamiltonian splitting. This splitting, due to $^{59}$Co, is to be neglected [dG93], since:

1. the quadrupole splitting is very small compared to the hyperfine splitting (in frequency 0.2 MHz versus 220 MHz, respectively);

2. the electrochemically deposited Co/Cu multilayers and Co films consist of, besides a minor part of hexagonal-close-packed (hcp) structure, a mainly face-centered-cubic (fcc) structure.

Hence it wil, at most, show up as a line broadening not affecting the NMR resonance frequency.

## 2.2 Origin of the magnetic field at a nucleus

### 2.2.1 Hyperfine field

There are three main sources constituting the magnetic hyperfine interaction and thus the hyperfine field. These contributions are shortly discussed in this subsection. More information can be found in [dG93]. The three contributions are:

1. the contact field $\vec{B}_{cont}$, which arises from the Fermi contact interaction;
2. the dipolar hyperfine field $\vec{B}_{dip,at}$, which is due to the dipolar interaction between the nuclear magnetic moment and the spins of the $d$ shell electrons from the atom itself;
3. the orbital field $\vec{B}_{orb}$, which arises from the interaction between the nuclear magnetic moment and the unquenched part of the orbital angular momentum of the valence electrons.

Thus, in formula, $\vec{B}'_{hf}$ can be written as:

$$\vec{B}'_{hf} = \vec{B}_{cont} + \vec{B}_{dip,at} + \vec{B}_{orb} \tag{2.5}$$

#### The contact field

This is the main contribution to the hyperfine field. $\vec{B}_{cont}$ is proportional to the spin density of the electrons at the nucleus [Fer30]:

$$\vec{B}_{cont} = \frac{8}{3}\pi\mu_B m(0) \tag{2.6}$$

with $\mu_B$ the Bohr magneton and $m(0)$ the spin density at the nucleus. The $s$ electrons are the electrons with the largest spin density at the nucleus. The contributions of the inner electronic $s$ wave functions (the core $s$ electrons) are not cancelled in equation 2.6, despite the *pairing* of these electrons. This is due to the intra atomic exchange interaction between the $s$ orbitals of the core electrons and the magnetically polarized $d$ shell. The majority core $s$ electrons are pulled toward the $d$ shell and the minority electrons are repelled from the $d$ shell. This results in a net minority polarization of the core $s$ electrons at the nucleus, thus a $\vec{B}_{cont}$ contribution *antiparallel* to the electron magnetization.

In addition to the core polarization, also the valence $4s$ electrons are polarized and contribute to $m(0)$. Here this $s$ polarization originates mainly from two sources:

1. the polarization of the valence $4s$ electron is due to the $3d$ moment of the atom itself (more majority and less minority $4s$ states are occupied);
2. the hybridization of the valence $4s$ wave functions with the polarized $3d$ wave functions of the neighbouring atoms causes a weak $4s$ polarization, which is called the *transferred* contribution.

The sign and magnitude of the transferred contribution depend on the magnetic moment of the neighbouring atoms, which makes $B_{cont}$ sensitive to the local environment.

### The dipolar hyperfine field

The dipolar hyperfine field arises from the dipolar interaction of the nuclear magnetic moment and the magnetic moment of the unquenced $3d$ electrons of the same atom. The wave functions of these electrons are spatially deformed due to the local environment of the atom. In fact, the dipolar hyperfine field vanishes for sites with *cubic* symmetry (e.g. fcc). For non-cubic sites, e.g. hcp, $\vec{B}_{dip,at}$ yields a small anisotropy of $B_{hf}$ [PJM65].

### The orbital field

The orbital field is caused by the orbital angular momentum of the unquenched $3d$ electrons and can, in a simplified way, be described as proportional to the expectation value of the angular momentum operator $\vec{L}$ of the electrons, divided by the distance $r$ of the electrons to the nucleus, to the third power. In formula:

$$\vec{B}_{orb} = \mu_B \left\langle \frac{\vec{L}}{r^3} \right\rangle \tag{2.7}$$

in which $\mu_B$ is the Bohr magneton.

In a cubic environment the orbital moment is normally quenched and, therefore, no orbital field is expected. However, due to spin-orbit coupling a small orbital moment is induced, resulting in an orbital field which is antiparallel to the contact term.

For a lower symmetry, the orbital moment of the $3d$ electrons are unquenced, yielding an anisotropic contribution to $\vec{B}'_{hf}$. The contribution of $\vec{B}_{orb}$ depends on the direction of $\langle\vec{L}\rangle$ and via the spin-orbit coupling on the direction of the electron magnetization [PJM65].

## 2.2.2 Dipolar field

Apart from the dipolar interaction of the nuclear magnetic moment and the moment of the $3d$ electrons of the same atom, there is a dipolar field arising from the dipole-dipole interaction of the nuclear magnetic moment and the magnetic moments of all the other atoms in the sample. This dipolar field can be expressed by:

$$\vec{B}_{dip} = \frac{\mu_0}{4\pi} \sum_{i \neq j}^{n} \left[ -\frac{\vec{m}_i}{|\vec{r}_i|^3} + \frac{3(\vec{m}_i \cdot \vec{r}_i)\vec{r}_i}{|\vec{r}_i|^5} \right] \tag{2.8}$$

in which the sum runs over all (n) the moments ($m_i$) of the atom (i), *except* for the moment of the *own* atom (j). The relative position of $\vec{m}_i$ to the nucleus is given by $\vec{r}_i$.

The dipolar field can be viewed upon as the sum of an isotropic part: the Lorentz field ($\vec{B}_L = \frac{1}{3}\mu_0\vec{M}_s$) and an anisotropic part: the demagnetizing field $\vec{B}_{demag}$ [Col71].

In the following of this report $\vec{B}_{hf}$ is defined as the sum of $\vec{B}'_{hf}$ and the isotropic part of the dipolar field, the Lorentz field $\vec{B}_L$:

$$\vec{B}_{hf} = \vec{B}'_{hf} + \vec{B}_L \tag{2.9}$$

## 2.3 Relation between local environment and hyperfine field

In the previous section it appeared that the magnetic field at a nucleus depends on the local atomic environment. This sensitivity is caused by the spatial distribution of majority and minority spins. In figure 2.1, the influences of structure, strain, and foreign neighbours are illustrated in a hypothetical spectrum, in the case of $^{59}$Co. These influences will be discussed in the text below. The specific properties giving expression to the NMR spectrum of $^{57}$Fe in $Fe_3O_4$ will be dealt with in chapter 4.

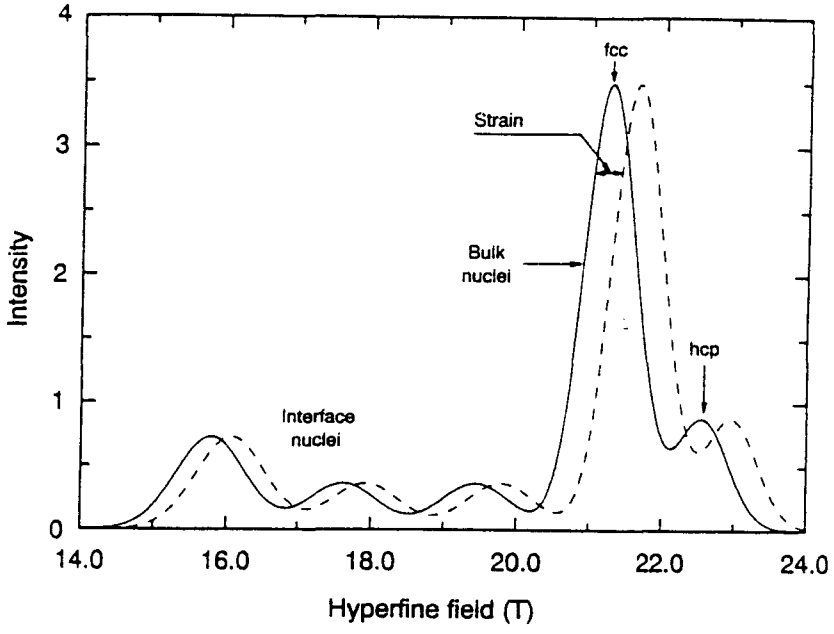


Figure 2.1: *A hypothetical spectrum of the intensity versus the hyperfine field (with the applied field parallel to the film plane). The intensity of a line is proportional to the number of atoms with a specific local environment. The figure shows that the hyperfine field of atoms in a fcc structure differs from atoms in a hcp structure. Resonance lines of atoms at the interface are shifted compared with the line of the bulk atoms. Uniform strain results in an overall shift of the spectrum.*

### 2.3.1 Structure

The local structure and symmetry determines the magnitude and the anisotropy in the hyperfine field. The valence electrons polarization and the $3d$ magnetic moment depend on the local structure, which determines the magnitude of the hyperfine field.

If the environment is non-cubic, there is an anisotropic contribution to the hyperfine field, which arises from the dipolar and orbital contribution to the hyperfine field.

This leads for hcp $^{59}$Co to an anisotropic hyperfine field of about 22.4 T [dG93]. Assuming uniaxial symmetry and thin film geometry, the anisotropy of hcp cobalt can be

determined by applying the external field parallel (//) and perpendicular ($\perp$) to the $c$-axis, which leads to [vS92]:

$$2\pi f = \gamma(B_{hf,//} - B_{appl,//}) \tag{2.10}$$

$$2\pi f = \gamma(B_{hf,\perp} + \mu_0 M_s - B_{appl,\perp}) \tag{2.11}$$

Measured values of $\mu_0 M_s$ for $^{59}$Co at 4.2 K are 1.79 T [RDR+87] and 1.85 T [Wij80]. If $B_{hf}$ is split into an isotropic $B_i$ and an anisotropic term $B_a$ ($B_{hf,//} = B_i - \frac{1}{2}B_a$ and $B_{hf,\perp} = B_i + B_a$) [vS92], the last two equations can be combined to:

$$B_{appl,\perp} = B_{appl,//} + \mu_0 M_s + \frac{3}{2}B_a \tag{2.12}$$

For hcp $^{59}$Co, $B_i = 22.60 \pm 0.01$ T and $B_a = -0.57 \pm 0.01$ T [FGS+76]. For fcc $^{59}$Co, $B_i = 21.6$ T and $B_a = 0$ T [dG93].

### 2.3.2 Strain

Strain means that the lattice is compressed or expanded, due to external stress. In a multilayer, strain can be caused by a difference in the lattice parameters of the different elements at the interface.

In the case of isotropic pressure on a crystal, the lattice will contract, which has two opposing effects on the hyperfine field. The magnetic moment will decrease. This leads to a decrease in the polarization of the core $s$ electrons, due to a decrease in the exchange polarization forces. Secondly, the spin density of the valence $4s$ electrons at the nucleus will increase, due to the slight squeezing of the electrons.

The change in the hyperfine field will be the net result of the two above-mentioned opposite contributions [Jan79]. In Co the hyperfine field decreases under pressure, whereas in Fe it increases. For cobalt the relation between strain and hyperfine field is given by [dG93]:

$$\frac{\Delta B_{hf}}{B_{hf}} = -1.17\frac{\Delta V}{V} \tag{2.13}$$

where $\Delta V$ denotes the change in atomic volume $V$.

In thin films and multilayers the strain is usually due to a lattice mismatch between film and substrate (or baselayer) òr between the neighbouring layers at the interfaces. The mismatch $\eta$ at the interface is defined as:

$$\eta = \frac{a_{Co} - a_X}{\frac{1}{2}(a_{Co} + a_X)} \tag{2.14}$$

where $a$ denotes the lattice constant. The relaxation of the strain $\epsilon$ due to this mismatch can be achieved in two ways [vAtVdG+94].

First, one layer can be stretched and the other compressed, so that both layers have the same in plane lattice parameter (figure 2.2a). The lattice parameter perpendicular to the plane will be compressed or stretched, the opposite way, according to the Poisson's

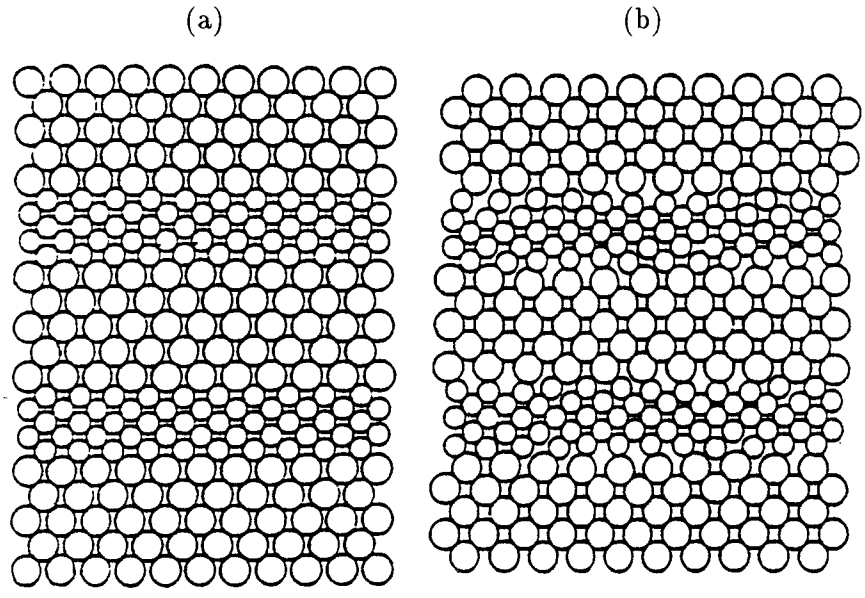


Figure 2.2: *A schematical display of (a) a coherent, and (b) an incoherente multilayer. At the interface, in which the diverse elements with different lattice constants of a multilayer will meet, the difference in lattice constants will, in some way or the other, be (partially) removed. When both different elements at the interface have gained a collective value for their lattice constants, then one has a coherent multilayer, in contrast with an incoherent multilayer.*

ratio $\sigma$. The energy to achieve this so called coherent strain is proportional to the volume (the lattice is continuous in all the layers): uniform strain.

Secondly, the strain can be partly relaxed by introducing interfacial dislocations (figure 2.2b). The lattice constants of the two layers are not the same, and at the interface the two different lattices are fit together by introducing dislocations. The energy to achieve this so called incoherent strain is proportional to the area of the filmplane (the dislocations are formed only at the interface area).

Because the coherent strain energy is proportional to the volume of the sample and the incoherent strain energy is proportional to the area of the film plane, it will be energetically favourable to have coherent strain below a certain thickness and incoherent strain above this thickness. This certain thickness is called the critical thickness, $t_c$. This $t_c$ depends on the lattice mismatch, the elastic constants, and the layer thicknesses of the two elements, e.g. for a (x Co + 20 Å Ag) multilayer $\eta = -14\%$, which gives a $t_c$ of about 2 Å [tV93]. If $t_{Co} \gg t_c$ the dependence of the strain is usually approximated by $1/t_{Co}$ [BR89].

### 2.3.3 Foreign neighbours

The hyperfine field will also change when an atom is surrounded by one or more "foreign" atoms. In general, an atom in the middle of a layer will be surrounded by the same kind of atoms, the bulk atoms. At the interface, layers of one kind of atoms (*host* atoms) are followed by layers of another kind of atoms (*foreign* atoms). The host atoms situated at the **interface** will have one or more foreign atoms in the nearest neighbour shell. In the special case of electrodeposited films and multilayers, the **bulk** also consists of impurities, i.e. the same foreign atoms as just-mentioned. Therefore the bulk can be seen as an **alloy** structure.

The foreign atom will change the hyperfine field of the host atoms in two ways. First, the foreign atom will have an other electrostatic potential (i.e. nuclear charge), which will be screened to maintain local charge neutrality. If the screening can not completely be performed by the foreign atom, the non-local $4s$ and $3d$ wave functions of the surrounding atoms (the host atoms) will slightly change to regain charge neutrality. The change in the spin density of the host atoms will change the hyperfine field. Secondly, the foreign atom will have a different magnetic moment and the hyperfine field of the host atoms is changed by the transferred polarization.

The magnitude of change in the hyperfine field of the host atoms depends on the foreign atom. Substituting more than one foreign atom in the nearest neighbour shell of the host atoms will give a change, which is approximately equal to the number of foreign atoms multiplied with the change for one foreign atom. This approximation should be seen as being of the first order, not taking the different spatial preferences into acount which exists in case of 2 or more foreign atoms. First order implies also a small ratio foreign neighbours to host atoms, i.e. 5, at most 6 [TM92], of the 12 nearest neighbours in case of fcc or hcp structure. In general, a foreign atom in the nearest neighbour shell will give rise to a satellite line separated from the bulk line, while foreign atoms in the next nearest neighbour shell merely give rise to a line broadening of the bulk line.

## 2.4 Determination of the interface roughness

After reading the previous sections, we are able to conclude that the hyperfine field spectra might give us a lot of structural information, such as: crystallographic structure (fcc, hcp, sf, ...), chemical inhomogeneities (i.e. the presence of foreign neigbouring atoms influenced by different growing conditions, different growing methods, etcetera), stacking faults, the average magnetization (proportionality), and stress.

Among these properties, *interface roughness* is an important one, especially in the case of multilayers (see chapter 1). Interface roughness in case of the electrodeposited Co/Cu multilayers is defined as the total amount (in Å) of Co atoms per Co layer which are surrounded by at least one Cu atom in the nearest neighbour shell. The contribution of the alloy structure of the Co bulk in the multilayers is assumed to be *negligible*. There are several ways to determine the interface roughness by means of a NMR spectrum. The

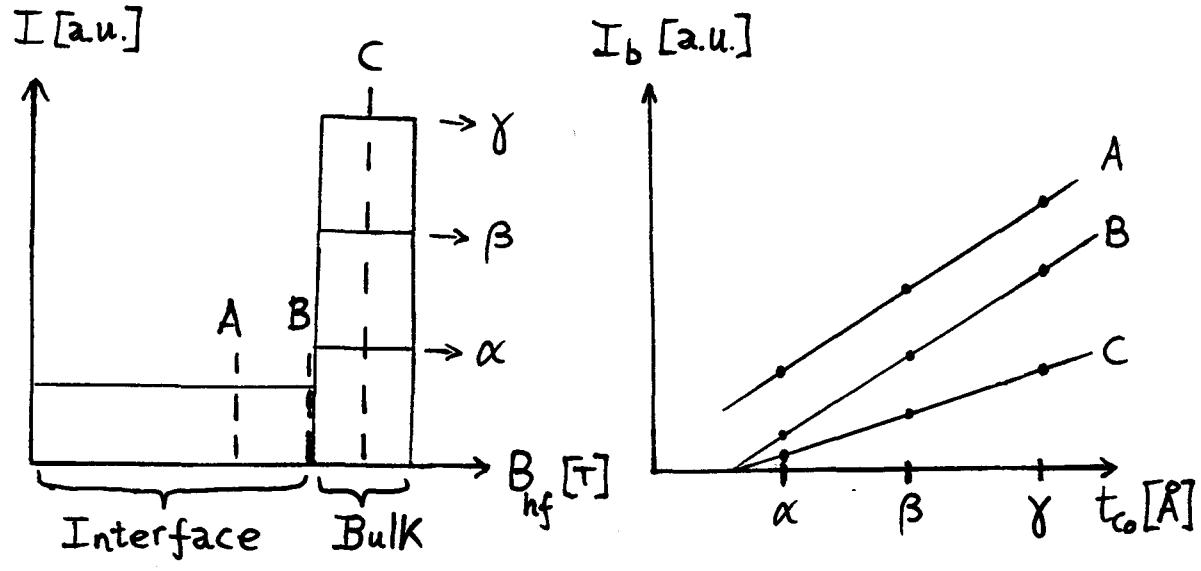


Figure 2.3: *The determination of the interface roughness by means of varying the 'splitting' hyperfine field value: A, B, and C. Three samples with varying Co layer thickness are taken: $\alpha$, $\beta$, and $\gamma$. The fitted line due to splitting value A contains an offset compared to the assumingly correct splitting value B. The fitted line due to splitting value C got as shortage of bulk, which is in percentages the same amongst all three samples $\alpha$, $\beta$, and $\gamma$.*

first - and most straight forward - method is assessing the hyperfine field value at which the intensity, mainly due to satellite lines, changes into a mainly bulk line contribution. This hyperfine field value splits the spectrum into two parts: an *interface* part and a *bulk* part. After normalizing the *total* spectrum on the Co layer thickness, one is able to determine the relative (and consequently absolute) portions of interfacial atoms and of bulk Co atoms. A disadvantage of this method is the incompleteness of measuring the whole NMR spectrum, i.e. measuring at hyperfine field values no smaller than about 15 T. But this method requires no series of multilayers with different Co layer thicknesses which have to be grown and measured under identical circumstances, in contradistinction with the two other methods shortly following. The 'uncertainty' of the contributions of higher satellite lines and the randomness of determining the 'splitting' hyperfine field value between interface and bulk make the first method to determine interface roughness not highly reliable.

A second manner of dealing with interface roughness is measuring the NMR spectra of a series of multilayers with varying Co layer thickness while interface *roughness* and *topology* are constant. These NMR spectra ought to be normalized on their different Co layer thickness causing the interfacial part to overlap. Only nearby the bulk portion the NMR spectra ought to differ in intensity. The interface roughness can be determined by plotting the bulk intensity as a function of the Co thickness. The straight line fitted through the measured values crosses the x-axis. In this point, the intensity of the bulk is

zero and so is this determined Co thickness a value for the interface roughness, i.e. two times the mixed region per interface.

The now following third manner is a slight variation of the second. One assumes in this case an identical interface spectrum, i.e. identical interface roughness and topology. This implies that the alloy structure of the bulk due to electrodeposition is again to be seen as negligible. The above-mentioned 'splitting' hyperfine field value is determined with a higher accuracy. The spectra are all normalized on the Co layer thickness of the samples. The splitting hyperfine field value is taken in steps per series and the bulk intensities (on the y-axis), although they might not be right, are to be shown as function of the Co thickness of the samples (on the x-axis) belonging to the same series. If the splitting value is too *low*, it means that beside bulk also a (small) part of interface intensity is taken into account. This implies that we have an *offset* value in our function. On the other hand, if the splitting value is too *high*, a certain percentage of the bulk intensity will not be considered. This percentage is the same for all above-mentioned samples belonging to the same series. This means that the *slope* of the straight line, in our case bulk intensity as a function of Co layer thickness, will vary proportionally to the just-mentioned percentage of the bulk intensity, but the x-axis will still be crossed in the (same) interface roughness value. See figure 2.3.

# Chapter 3

# Experimental methods and equipment

*NMR experiments are used to obtain the magnitude of the hyperfine field experienced by the nuclei. This year, it is exactly fifty years ago that NMR experiments were first carried out in bulk matter by two groups of people, independently and with a different approach. Section 3.1 is an introduction into these different approaches, which will follow in sections 3.2 and 3.3. In section 3.3 some experimental parameters influencing the NMR spectra will be shortly discussed. Section 3.4 closes the chapter by reviewing briefly the equipment.*

## 3.1 The NMR evolution

Actually the first nuclear magnetic resonance experiments have been performed in beams by Rabi et al. [RMKZ39] in 1939 using a beam deflection method (a modification of the method used by Stern and Gerlach in 1925) to measure the magnetic moment of *the proton.* However, the first succesful NMR experiments *in bulk matter* were achieved in 1945 by Purcell et al. [PTP46] and soon afterwards, independently, by Bloch et al. [BHP46a]. The groups used each a different approach. On the one hand Purcell et al. were concerned with the loss of the coil at resonance, while on the other hand Bloch et al. observed the electromotive force induced in the coil by the nuclear moments precessing around the magnetic field. This coil was wrapped around the sample and used for transmitting a high frequent signal and receiving the spin-echo signal, as furtheron in this chapter will be explained in detail.

The underlying idea of the former approach is directly related to the conventional description [TPP46] of a *spectroscopic method*, i.e. photon-energy absorption (considering only energy levels with in between photon-induced transition probabilities), while the latter idea of *nuclear induction* is related to a complete description [BHP46b] of the motion of nuclear moments in steady and alternating magnetic fields.

## 3.2 The Bloch equations

In equilibrium, the total magnetization of a system of nuclear spins, $\vec{M}$ ($M_x$, $M_y$, $M_z$), is directed parallel to the total effective field[1] experienced by the nuclei; $\vec{B} = B_0\vec{e}_z$, thus $\vec{M} = M_0\vec{e}_z$. The dynamic behavior of the magnetization can be described [Abr61, Sli78] by the so-called Bloch equations:

$$\begin{aligned} \dot{M}_z &= -\frac{M_z - M_0}{T_1} \\ \dot{M}_x &= -\frac{M_x}{T_2} + \gamma(\vec{M} \times \vec{B})_x \\ \dot{M}_y &= -\frac{M_y}{T_2} + \gamma(\vec{M} \times \vec{B})_y \end{aligned} \tag{3.1}$$

If, in equilibrium, a radio frequency (rf) field pulse is applied perpendicular to the $z$-axis, e.g. $\vec{B}_1 = 2B_1 cos(\omega t)\vec{e}_x$, with a pulse duration *much shorter* than the relaxation times $T_1$ and $T_2$, the relaxation can be neglected and equation 3.1 can be rewritten as:

$$\dot{\vec{M}} = \gamma\vec{M} \times [B_0\vec{e}_z + 2B_1 cos(\omega t)\vec{e}_x] \tag{3.2}$$

Introducing a frame rotating around the $z$-axis (denoted with $^*$ and $\vec{e}_{z^*} = \vec{e}_z$) with frequency $\omega$, the rf field with frequency $\omega$ can be decomposed into a right and a left circular polarized component, of which one is a static field and the other a high frequency ($2\omega$) field component. Neglecting the high frequency field component in this rotating frame, equation 3.2 transforms into:

$$\frac{\partial}{\partial t}\vec{M}^* = \vec{M}^* \times [(\gamma B_0 - \omega)\vec{e}_{z^*} + \gamma B_1 \vec{e}_{x^*}] \tag{3.3}$$

If the frequency $\omega \approx \gamma B_0$, called the Larmor frequency $\omega_L$, the magnetization mainly rotates around the $x^*$-axis. The angle of rotation, $\alpha$, is given by:

$$\alpha = \gamma B_1^{eff} \tau_p \tag{3.4}$$

where $\tau_p$ denotes the duration of the rf pulse and $B_1^{eff}$ the total effective radio frequency field experienced by the nuclei.

At the start of the NMR experiment, the magnetization is at equilibrium ($\vec{M} = M_0\vec{e}_z$). Then a sequence of two rf pulses is applied. The first rf pulse, e.g. $\vec{B}_1 = 2B_1 cos(\omega t)\vec{e}_x$, is applied for a time $\tau_p$, in which the nuclear spins turn $\pi/2$ around the $x^*$-axis: from the $z^*$-axis to the $y^*$-axis (the $\pi/2$ pulse). The spins start to dephase in the $x^* - y^*$ plane due to field inhomogeneities and the magnetization decrease to zero (*free induction decay*). After a delay time of $\tau$ from the start of the first pulse, again a rf pulse is applied with a duration of $2\tau_p$. This second pulse flips the spins in the $x^* - y^*$ plane (the $\pi$ pulse), so that after the same delay $\tau$ the spins will refocus again and the magnetization has its maximum value, the spin-echo, see figure 3.1.

[1] The total effective field $\vec{B}_{tot}$ given in chapter 2 is identical to the total effective field $\vec{B}_0$ used in this chapter.

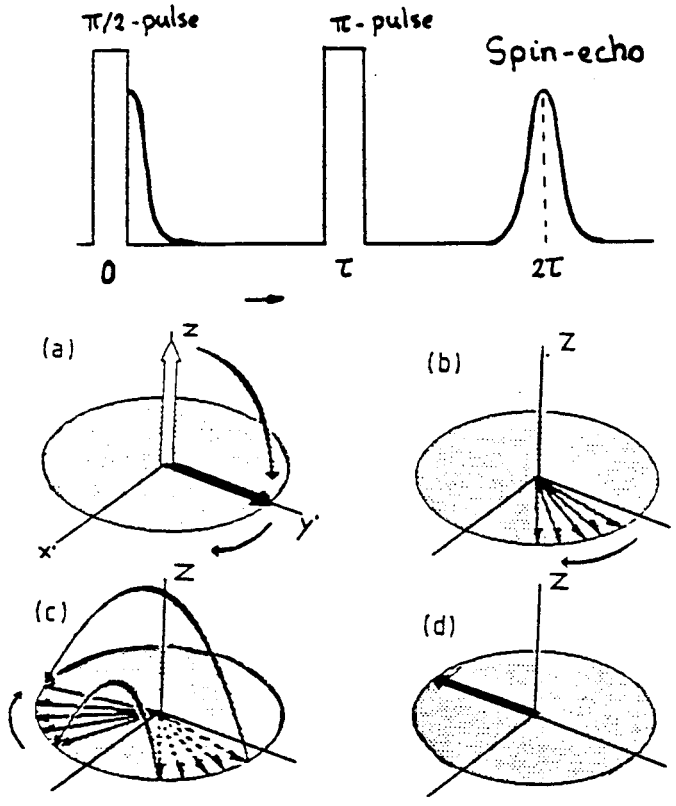


Figure 3.1: *In the upper picture the pulse sequence and spin-echo are given schematically. In the lower picture, a: the turning of the nuclear spins over $\pi/2$, b: the dephasing of the nuclear spins, c: the turning of the nuclear spins over $\pi$, and d: the spin-echo after the refocussing of the nuclear spins are shown.*

## 3.3 The resonance condition and some experimental parameters

In condensed matter and for temperatures above the milli-Kelvin range nuclear magnetism is dominated by spin paramagnetism [Pan86]. When a magnetic field $B_0$ is present at nuclei which possess a spin $I$ their ground state is split by the Zeeman interaction into $2I+1$ levels, indexed by the quantum number $m$ ($-I \leq m \leq +I$), the energy of which is $E_m = -m\hbar\gamma B_0$ (see chapter 2). Therefore the energy difference between two adjacent levels is $\Delta E = \hbar\gamma B_0$ and the NMR spectrum consists of only one absorption resonance line at the Larmor frequency $\omega_L = \gamma B_0$.

According to Boltzmann's law the population of the levels is proportional to $exp\left[\frac{m\hbar\gamma B_0}{k_B T}\right]$ which gives rise to the net nuclear magnetization:

$$M_0 = N\hbar\gamma \frac{\sum_{m=-I}^{I} m \cdot exp\left[\frac{m\hbar\gamma B_0}{k_B T}\right]}{\sum_{m=-I}^{I} exp\left[\frac{m\hbar\gamma B_0}{k_B T}\right]} \tag{3.5}$$

for a system of $N$ nuclear spins. Actually the Zeeman energy is almost always much weaker than the thermal energy and $M_0$ in equation 3.5 can be approximated by the Curie law:

$$M_0 = \frac{N\gamma^2\hbar^2 I(I+1)B_0}{3k_B T} \tag{3.6}$$

with $N$ nuclei per unit volume generating this total magnetic moment in thermal equilibrium at a temperature $T$.

If the static magnetic field is applied parallel to the film plane, the resonance condition given by equation 2.4 becomes:

$$2\pi f = \gamma(B_{hf} - B_{appl}) \tag{3.7}$$

From this equation, one can see that the hyperfine field distribution can be obtained in two ways, namely:

- *frequency*-scan: the applied field remains constant (usually 0 T) and the frequency is varied;
- *field*-scan: the frequency is constant and the applied field is varied.

All the spectra of the electrodeposited Co/Cu multilayers and Co films described in chapter 5 of this report are obtained by field scans at different frequencies. However, the bulk $Fe_3O_4$ spectra shown in chapter 4 are obtained partially by field scans and partially by frequency scans. For a spin-echo **field-scan** experiment, the sample is placed in a coil, which applies the rf field pulses and detects the induction signal of the spin-echo. The coil is incorporated in a tuned circuit as given in figure 3.2. At each frequency, the variable capacitors are tuned to obtain an impedance matching to the coax cable (50 $\Omega$) and the rest of the equipment. The Q factor is lowered by adding a resistor with a value of about 1 $\Omega$, which yields a broadening of the impedance versus frequency curve. The matching of the LC circuit is achieved by minimizing the reflected power. An electronic switch leads the pulse sequence from the transmitter to the LC circuit and the spin-echo signal to the receiver.

NMR spectra obtained by a **frequency-scan** experiment in zero-field have the advantage of an increase in spin-echo intensity, which arises from the nuclear spins situated in a domain wall, whose enhancement is often much larger than in case of spins in a domain. The LC circuit has also be tuned for each frequency to obtain the impedance matching the 50 $\Omega$ coax cable, but to save time in optimizing the circuit a *wideband* LC circuit is used. Such LC circuits use constant capacitors, thus the circuit is not tuned for each frequency and the detected spin-echo intensity decreases due to low quality factor of the LC circuit, but the zero-field enhancement will compensate this disadvantage. The LC circuit used for frequency scans is identical to the one used by Riedi in St. Andrews, England: a coil connected on the one end with an electronic switch and on the other end with a 50 $\Omega$ resistance. Around the coil a thin brass plate is wrapped which acts as a capacitor. The

capacitor's value depends upon the distance between the coil and the plate. Both the 50 Ω resistance and the brass plate are electrically earthed. This circuit tries to imitate an ideal transmission line by using compensating induction and capacity values and is called the transmission LC [vdH94]. The reflection as function of the frequency is not constant, thus the intensity given in the NMR spectra obtained with the wideband circuit are unreliable to use for comparing parts of one spectrum with each other.

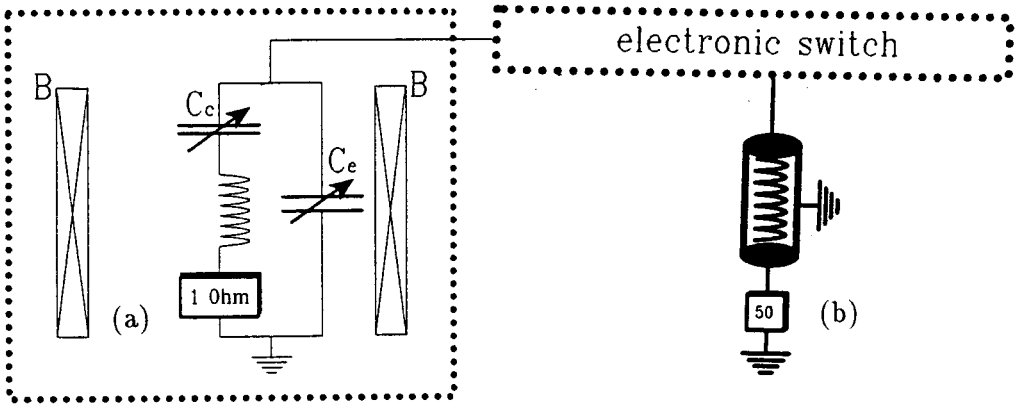


Figure 3.2: *The LC ciruits used to obtain the field-scans (a) and the frequency-scans (b) as described in the text. The sample is placed in the coil positioned in the middle of a magnet. In case of field-scans the direction of the magnetic field with respect to the film normal of the sample can be varied, while in case of frequency-scans no use is made of the magnet.*

### 3.3.1 Enhancement

When NMR is observed in ferromagnetic materials one will notice that the required rf power is much less and signal intensity is much larger than expected. The enhancement mechanism for both the applied rf field (*transmitting* enhancement) and the nuclear induction signal (*receiving* enhancement) arises from the presence of the large local fields at the nuclei of the magnetic atoms associated with the large magnitude of the electron spin magnetic moment $\langle S \rangle$.

Thus the in equation 3.4 mentioned $B_1^{eff}$ is larger than the applied $B_1$, because it is enhanced by the magnetization of the electron spin system. This magnetization will be directed along the total field, i.e. the sum of $\vec{B}_1$ and $\vec{B}_{appl}$, and thus also causes a rf field. The magnitude of the total radio frequency field is given by:

$$B_1^{eff} = |\vec{B}_1 + \vec{B}_{loc,\perp}| = B_1 - B_{loc,\perp} = |1 - \eta| B_1 \tag{3.8}$$

with $\vec{B}_{loc} = \vec{B}'_{hf} + \vec{B}_{dip}$ [dG93] and $\eta$ the enhancement factor [GP59]:

$$\eta = \frac{B_{loc,\perp}}{B_1} = \frac{B_{loc} \sin\theta}{B_1} \cong \frac{B_{loc}}{(B_{appl} + B_a)} \tag{3.9}$$

where the latter relation holds if $B_1 \ll (B_{appl} + B_a)$ with $B_a$ the effective electronic anisotropy field [dGdJ92], see also figure 3.3.

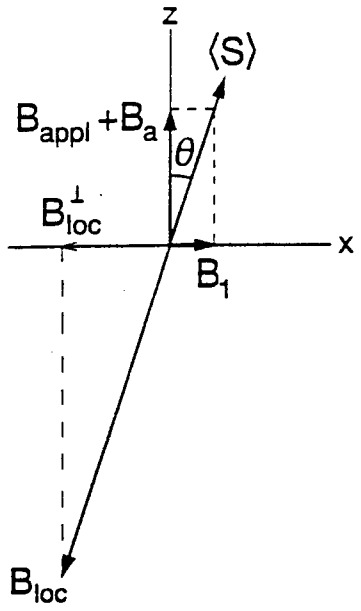


Figure 3.3: *Illustration of the determination of the enhancement factor* $\eta = \frac{B_{loc,\perp}}{B_1}$ *of the rf field.*

As quoted above, not only the rf field is enhanced but also the nuclear induction signal. Through the hyperfine interaction the precessing nuclear magnetization induces a coherent precession of the (entire) electronic magnetization. The total transverse magnetization is proportional to $(1-\eta)$ and therefore the induced signal in the receiver coil is also enhanced by $|1-\eta|$:

$$M_t \sim |1-\eta| \cdot M_0 \tag{3.10}$$

### 3.3.2 Relaxation

At the beginning of this chapter longitudinal relaxation and the free induction decay (characterized by $T_1$ and $T_2$ respectively) were neglected. In this part we want to discuss their influence on NMR spin-echo measurements.

The *spin-spin* or *transverse* relaxation gives rise to an irreversible dephasing of the nuclear spins, thus reduces the magnitude of the spin-echo. Because the hyperfine field has *time fluctuating* components, the Larmor frequencies of the individual spins fluctuate randomly, causing a free induction decay *homogeneous broadening* of a spin-echo resonance line. There are also *time-independent* causes for the spread of Larmor frequencies as field inhomogeneities obviously are (spatial fluctuations). These are responsible for the *inhomogeneous broadening* of the spin-echo resonance line.

If the spins were free, this signal would last forever but actually relaxation mechanisms take place and the *transverse* magnetization which is observed decays with a characteristic

time $T_2$:

$$M_t \sim M_0 \cdot exp\left[\frac{-2\tau}{T_2}\right] \tag{3.11}$$

This provides a means of measuring the transverse relaxation (by varying the time between the first and second rf pulse: $\tau$) even in the presence of strong inhomogeneous broadening.

Beside this transverse component of the total magnetization $M_t$, a longitudinal magnetization $M_l$ exists. When the nuclear spin system, originally being at thermal equilibrium ($M_l = M_0; M_t = 0$), obtains a $90^o$ pulse, it will cancel the *longitudinal* magnetization ($M_l = 0; M_t = M_0$). $M_l$ now relaxes towards equilibrium with a characteristic time $T_1$. After a time interval $t$ the longitudinal magnezation $M_l(t)$ is measured. If we repeat the experiment for various $t$ the full time recovery curve of $M_l$ from 0 to $M_0$ is obtained. This recovery is usually exponential and reads (see equation 3.1):

$$M_l(t) = M_0(t) \cdot \left[1 - exp\left(\frac{-t}{T_1}\right)\right] \tag{3.12}$$

This *spin-lattice* or *longitudinal* relaxation time $T_1$ depends upon the atom's environment and it is thus advisable to measure the spin-echo signal at all times $t \gg T_1$ in order to prevent the NMR spectrum from a $T_1$ dependence. $T_1$ varied for example in electrodeposited samples between approximately 5 and 40 ms, thus we used a long delay, i.e. the time between two successive spin-echo experiments, of 100 ms.

### 3.3.3 Frequency dependence

When measuring a NMR spectrum by means of a frequency scan, one needs to consider correction for the signal due to a frequency dependence. At resonance the spin-echo induces an oscillatory flux in the coil. The electromotive force (EMF) has got a maximum value when the flux through the coil is maximum and has the following relationship:

$$EMF \sim \omega_L \cdot M_0 \tag{3.13}$$

in which $\omega_L (= 2\pi f)$ is the Larmor frequency, i.e. the resonance frequency ($2\pi f = \gamma B_0$) and $M_0$ is the total magnetization. Due to equations 3.6 and 3.13 one may conclude that the spin-echo intensity is to be corrected for $f^2$.

Rubinstein [RS73], however, corrects the intensity at each point in the obtained NMR spectra by dividing by $f^3$ (f stands for the resonance frequency) to match the variation of the experimental spin-echo amplitude with frequency due to:

**1** Boltzmann distribution (with regard to the varation of the size of the nuclear moment);

**2** Faraday's law of induction (the voltage induced across the coil which results from magnetization precessing at frequencies close to the Larmor frequency);

**3** Enhancement effects (of a particular site within a section of a domain wall in a particular field).

A theoretical approach to explain enhancement correction for these three items was made by Dean et al. [DU70].

One can conclude from the above mentioned subsections that the spin-echo intensity depends on $T, T_1, T_2, |1-\eta|$, and the *frequency*. Here one has to state that *inhomogeneity of the rf field* due to imperfections of the coil (not being perfectly symmetric and infinite) and the *skin effect*, i.e. the effective penetration depth of $B_1$ and thus also of the spin-echo resonance, are not taken into account.

## 3.4 The equipment

In this section the hardware, which generates the pulses and detects the spin-echo, is only shortly described, for the used measuring equipment has already been described in detail [vdH94]. A global overview of the hardware setup is given in figure 3.4.

The controller's job is to set all the relevant parameters and to generate the control signals for the other modules. The input of the relevant parameters (like duration, strength, and interval between spin-echo pulses) is done via the terminal and the spin-echo data of the PhyDAS system are sent to the terminal. This system, which consists of interface units, a communication unit, and a processor and memory unit, performs the experiments and communicates between the terminal and interface units.

The main 'components' of the signal generator are a HP synthesizer to generate a continuous wave between 0.1 and 1040 MHz, an XMIT unit which transforms the continuous wave of the HP synthesizer into the desired pulse sequence and controls the amplitude of the pulses, and a wideband power amplifier to amplify the pulse sequence generated by the XMIT unit by 47.5±1.5 dB to at most 100 Watt RMS. The wideband amplifier has a frequency range between 0.1 and 500 MHz. The signal generator generates the puls sequence with the desired frequency, pulse durations, and power for the NMR experiment. The generated signal is led to the electronic switch.

In figure 3.5, the elements of the electronic switch: the direction coupler, reflection meter, and duplexer are given. The coil is used for both transmitting and receiving, thus an electronic switch is needed to lead the pulses to the coil and the spin-echo to the receiver. The reflection meter is used to optimize the matching of the LC circuit to the coax cable.

The receiver consists of a mixer, an intermediate frequency (IF) unit, a demodulator unit, and an oscilloscope. It transforms the rf spin-echo to low frequency voltage signals, after frequency independent amplifying of the spin-echo. The oscilloscope, a HP 54510A, which displays the low frequency voltage of the P and Q channel of the spin-echo as a function of time, is used during the magnetite measurements (chapter 4), but before measuring the electrodeposited samples (chapter 5), it was replaced by an Analog Singal Recorder (ASR).

In a large number of experiments analog periodic signals must be recorded and analyzed. To reduce the effects of background noise in the recorded signal, a number of subsequent

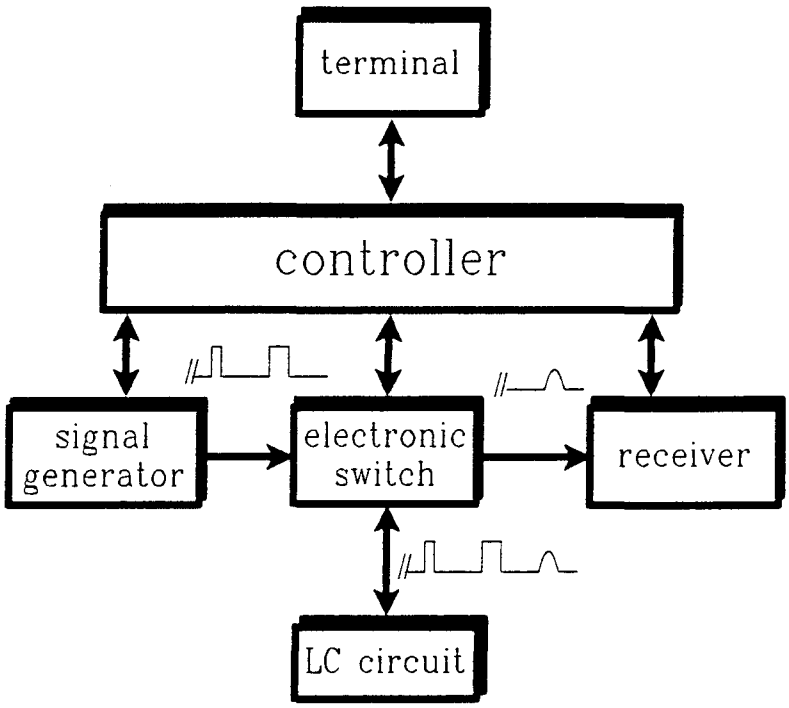


Figure 3.4: *The signal generator generates a rf pulse sequence of the desired frequency and amplifies the pulses to the desired power. Next the pulses are led to the electronic switch, which directs the pulses to the LC circuit and the spin-echo signal from the LC circuit to the receiver. The receiver detects the spin-echo. The controller controls the signal generator, the electronic switch, and the receiver and receives the spin-echo data. The terminal transfers the data from the controller to the PC and transfers all relevant parameters of the experiment to the controller.*

periods of this signal, i.e. spin-echo experiments, must be averaged. In order to minimize the dataflow, it is highly desirable that the averaging is performed *during* the recording of the analog signal.

The ASR performs an Analog-Digital conversion of M series of each N samples of an analog input signal, with M the number of periods to be averaged and N the number of samples taken by the ASR in each acquisition cycle of the analog input signal. The corresponding samples of each series are internally added and the results are stored in a local onboard static memory. After M times N samples are taken and averaged, this result becomes available via the PhyBUS. For more information about the ASR, see the user manual of the ASR [SvN94].

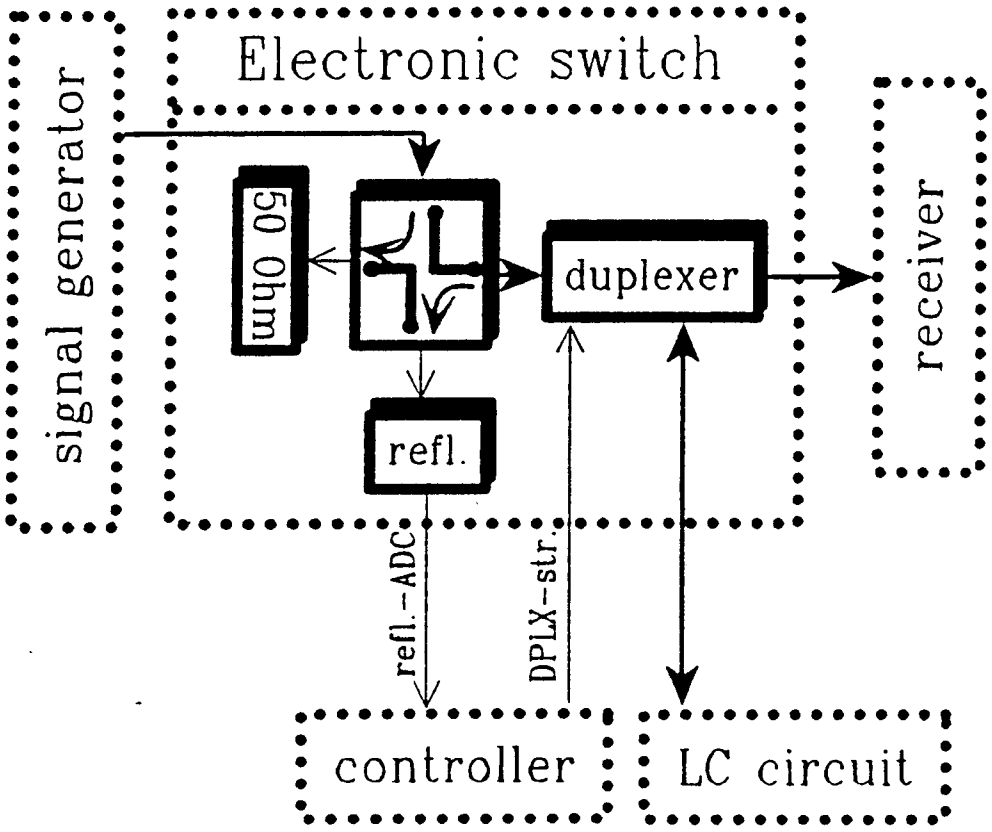


Figure 3.5: *The electronic switch consists of a direction coupler, reflection meter, and duplexer.*

# Chapter 4

# Magnetite ($Fe_3O_4$)

*In this chapter a literature review and some results of NMR experiments of magnetite samples will be shown. We will begin with an introductory section followed by section 4.2 explaining the structure of magnetite with the help of a literature review, based on NMR studies. Two samples were measured: a single crystal of magnetite shapen in a cylindrical form and a MBE grown 1150 Å layer of magnetite. Our purpose was to research the sensitivity in obtaining information about the future usefulness of NMR on even thinner magnetite layers. The NMR results of both samples are exposed in separate subsections (4.3.1 and 4.3.2). This chapter ends with discussing the NMR results in subsection 4.3.3.*

## 4.1 Introduction

Recently, there has been an increasing interest of studying transport properties, magnetic properties, and structural properties of artificially made oxides (especially $Fe_3O_4$ thin films) not only by our group Cooperative Phenomena at Eindhoven University of Technology (EUT) in cooperation with the group Magnetism at Philips Research Laboratories, but also worldwide by other persons like Terashima et al. [TB87], Fujii et al. [FTK+90a, FTK+90b, FTK+94], Lind et al. [LBC+92], Mishra et al. [MS93], and Margulies et al. [MPB94]. Several methods like electron spin resonance (ESR), Mössbauer spectroscopy, X-ray diffraction, etcetera are being applied to measure the above-mentioned properties.

Another method in obtaining (more) information concerning these properties is nuclear magnetic resonance (NMR). In the sixties, seventies, and early eighties many NMR studies were successfully carried out on magnetite *bulk films*, mostly single crystals. Frequently mentioned (co-)authors in articles about NMR experiments carried out on bulk films are: Boyd [BS62, Boy63], Ogawa [OM62], T. Mizoguchi [MT65, MI66], Rubinstein

| element | I | $\frac{\gamma}{2\pi}$ | N(%) | S(field) | S(zero-field) |
|---|---|---|---|---|---|
| H | $\frac{1}{2}$ | 43 | 100 | 100 | |
| Fe | $\frac{1}{2}$ | 1.4 | 2 | $8{\cdot}10^{-5}$ | 4 |
| Co | $\frac{7}{2}$ | 10 | 100 | 28 | $5.2{\cdot}10^{5}$ |
| Ni | $\frac{3}{2}$ | 3.8 | 1 | $4{\cdot}10^{-3}$ | 9 |
| Ag | $\frac{1}{2}$ | 2.0 | 49 | $5{\cdot}10^{-3}$ | |

Table 4.1: *NMR sensitivities (S) for different elements at a given temperature in case of an external magnetic field and zero field. Data are taken from Panissod* [Pan86] *and from de Gronckel* [dG93].

[RF71, RS73], Kovtun [KSS73, KS73a, KS73b], and M. Mizoguchi [Miz78a, Miz78b, MI80, IMU+80, YMI81, IMM+82, Miz85a, Miz85b]. The literature review in the next section is divided up according to the publications of the above-named (co-)authors.

Besides examining a bulk film magnetite sample, we will especially focuss in this chapter on the usefulness of NMR in obtaining information about the electronic ordering structure of an artificially made *thin film* magnetite sample. A thin film could give us information not only about the bulk structure, but also about strain.

Before being able to do so, one has got to consider the *sensitivity* of NMR for Fe nuclei. As we have seen in section 3.3.3, this sensitivity S is proportional to the EMF. The sensitivity is via equations 3.6 and 3.13 related to:

- T : temperature
- N : number of nuclei (natural abundance %)
- $\gamma$ : gyromagnetic ratio
- I : nuclear spin

The sensitivity of Fe is very small compared to, e.g. $^{59}$Co (I = 7/2), as shown in table 4.1. This is caused by the presence of *natural* iron in magnetite, the specific *gyromagnetic ratio*, and the magnitude of the *nuclear spin*. Natural iron in magnetite consists of *four isotopes* having each different relative contributions: 5.8 % $^{54}$Fe, 91.7 % $^{56}$Fe, 2.1 % $^{57}$Fe,

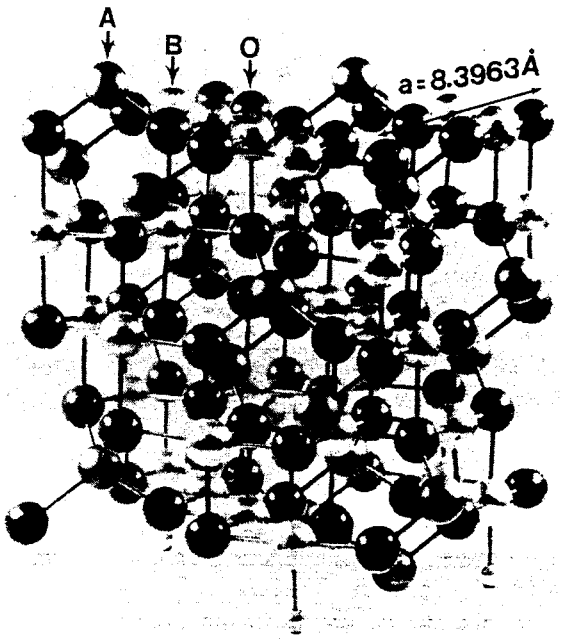


Figure 4.1: *Model of the spinel structure. This model contains one cubic unit cell. The A site, B site, and oxygen are indicated by arrows. In this notation a spinel, like magnetite, can be written as* $AB_2O_4$.

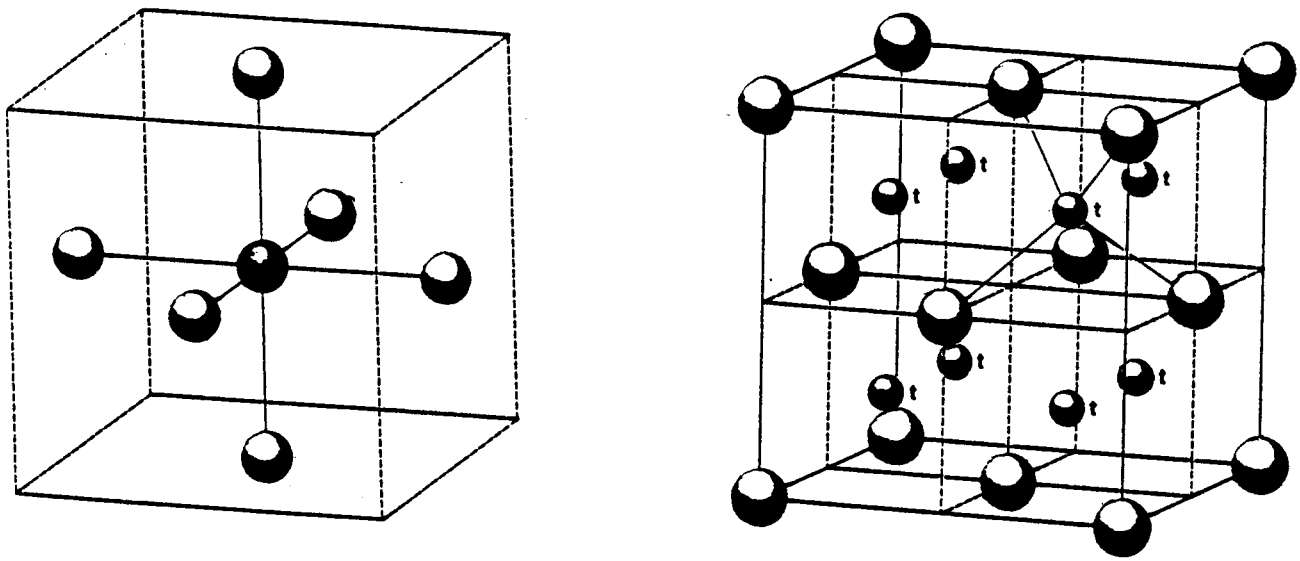


Figure 4.2: *Octrahedral (6 O neighbours) and tetrahedral (4 O neighbours) sites.*

and 0.4 % $^{58}$Fe. Of these natural isotopes only $^{57}$Fe has a nuclear spin (I = 1/2) and can be measured by NMR. Applying an external field decreases the NMR sensitivity: see table 4.1.

Magnetite ($Fe^{3+}[Fe^{2+}Fe^{3+}]O^{2-}{}_4$) is a ferrimagnetic oxide with an inverse spinel structure. It contains besides oxygen ions, both **ferrous** and **ferric** ions. The ferric ion $Fe^{3+}$ is a nearly spherical magnetic ion in which the 3d shell is just *half* filled causing a maximum spin magnetic moment. The ferrous ion $Fe^{2+}$ can be regarded as consisting of a ferric ion plus an *extra* electron [MI80].

At $T_V \simeq 120$ K magnetite undergoes a metal-insulator transition (the so-called Verwey transition). Verwey et al. [VH41] proposed that the transition is due to ordering of the $Fe^{2+}$ and the $Fe^{3+}$ ions on the octahedral sites and that above this transition temperature the material conducts by electron hopping between octahedral sites. The transition is assumed to be of the first order [RF71].

For temperatures well above the Verwey transition temperature, magnetite is built up of cubic unit cells, one shown in figure 4.1. This unit cell consists of eight magnetite molecules, and thus has eight ferric ions at the *tetrahedral* sites (**A sites**) which have four $O^{2-}$ atoms as nearest neighbours, and eight ferric ions and eight ferrous ions at the *octahedral* sites (**B sites**) which have six $O^{2-}$ atoms as nearest neighbours. See also figure 4.2. In respect to these different sites, a spinel like magnetite sometimes is written as $AB_2O_4$.

When magnetite is cooled down below the transition temperature the crystal symmetry will change from cubic to *orthorhombic*, but also other physical properties will change: the electrical conductivity drops sharply [CR73, KB79], the specific heat gets an anomalous peak at $T_V$ [BW73, KB76] and a second peak near 111−113 K [RMB83], and so on.

Since in 1941 Verwey has first tried to understand the structure of magnetite below $T_V$ by means of describing it by an electron ordering model, several adjustments have been made in order to remove discrepancies with experimental (also NMR) data.

## 4.2 The $Fe_3O_4$ structure: a NMR literature review

**Boyd** describes effects of anisotropy of the hyperfine interaction on NMR [BS62, Boy63] in a ferromagnetic or ferrimagnetic material. One sample he used for $^{57}$Fe NMR possesses a polycrystalline structure of magnetite, the other is a magnetite powder. Some of the samples are enriched with 90 % $^{57}$Fe. He obtained the NMR spectra of the cubic spinel structure of magnetite. The sharp line at 61.6 MHz he attributed to the hyperfine interaction on tetrahedral sites. The wide peak, found at 63.3 MHz, arises from Fe nuclei at the B sites. An iron nucleus on an octahedral site is exposed to a local crystal field of trigonal symmetry. The shape of the line is sensitive to the mode of nuclear excitation. Three limiting cases have been considered by Boyd:

1 *Discrete orientation:* the excitation is by domain rotation and the equilibrium orientation of the spontaneous magnetization is parallel to an axis of minimum crystalline anisotropy;

2 *Random orientation:* the crystalline anisotropy is overwhelmed by shape anisotropy (or some other random influence) and the excitation is through domain rotation;

3 *Domain wall excitation:* the situation in which the spontaneous magnetization is confined to the plane of a domain wall.

Therefore the A sites are caused by a hyperfine interaction where anisotropy is not expected from symmetry. However, the broad line (due to isotropic effects, i.e. the powdered structure) attributed to the B sites is caused by nuclei which are excited predominantly by domain rotation and thus an anisotropy term is expected.

Boyd also expresses that $Fe^{3+}$ and $Fe^{2+}$ ions occur in equal numbers in octahedral sites [Boy63]. The Verwey model holds in claiming that there is a rapid interchange of electrons among the iron ions in octahedral symmetry to explain the high conductivity of cubic magnetite. Since $Fe_3O_4$ is completely inverse, only $Fe^{3+}$ ions of a time average electronic spin of $\frac{5}{2}$ are present on the A lattice and an average spin of $\frac{4.5}{2}$ is assigned to each B ion. According to Boyd the spin-echo signal (and thus the sensitivity) comes from the nuclei in the bulk (domains) of the material rather than domain walls as in the case of the magnetic metals, while making no specific remarks about magnetic cooling[1] or obtaining NMR spectra by frequency scans or field scans. In his report [Boy63] Boyd attempted to fit the temperature dependence of the observed NMR frequencies for the two sublattices in magnetite to the measured temperature dependence of the magnetization. The measured magnetic moment, resonance frequency from tetrahedral sites, and distribution of resonance frequencies from octahedral sites, as function of the temperature T, are fitted with $T^{3/2}$.

**Ogawa** observed two resonances at room temperature in powdered magnetite, one (63.549 MHz) coming from the octrahedral sites and the other (67.621 MHz) from the tetrahedral sites [OM62]. He finds the values agreeing with two different effective magnetic fields obtained by NMR measurements done by Boyd [BS62]. The interpretation proposed by Verwey, that octahedral sites have equal amounts of trivalent irons and bivalent irons distributing randomly at high temperature and undergoing an ordered transition below about 110 K, has again been confirmed by Ogawa. The B site has a lower intensity than the A site because of the large line width which is considered to result from the electron diffusion between $Fe^{3+}$ and $Fe^{2+}$ in B site. By lowering the temperature resonance lines were followed to the transition temperature. Ogawa noticed that the intensity of A site resonance is gradually increased to about -120°C, and then it seems to decrease. At about -150°C the line diminishes in a short time. The resonance frequency at the disappearing point is 69.3 MHz. After the transition has finished a new line appears at somewhat higher frequency. The line has a smaller signal to noise ratio than that of high temperatures. Ogawa also followed the behaviour of the B site resonance by changing the temperature. In this case, however, after the line disappeared at the transition temperature, any new

[1]The definition of this term and its elaboration is dealt with in the literature review on M. Mizoguchi furtheron in this section.

resonance corresponding B site could not be found. Ogawa is sure that the resonance is mainly enhanced by domain wall excitation because an externally applied magnetic field reduced the intensity of these resonance lines and made them almost disappear at about 1 kOe (0.1 T).

**T. Mizoguchi** examined nuclear magnetic relaxation of $^{57}Fe$ on tetrahedral sites in polycrystalline magnetite [MT65] by spin-echo method with special interest in the relation to the low temperature transition and the electron diffusion among octahedral sites. Resuming earlier experiments described in and refered to by the above-mentioned articles of Boyd [Boy63] and Ogawa et al. [OM62], Mizoguchi remarked that the nuclear resonance of ferric ions on the A site gave a sharp resonance line and that the signal from B site ions showed a very broad distribution of resonance. The effect of the electron diffusion on the nuclear resonance of the B site at lower temperatures is more violent so that no resonance signal has been observed below the transition temperature, while the signal of the A site could be conveniently observed in the whole temperature range. Therefore, Mizoguchi investigated the nuclear relaxation of the A site in the temperature range between 4.2 and 335 K. The used specimen was prepared from stoichiometric $Fe_2O_3$ and Fe powder which were enclosed in evacuated silica tube and fired at 1100°C for about 10 hours. The low temperature transition at 118 K of this sample was confirmed by a magnetization measurement at low magnetic field. The relaxation Mizoguchi examined was not of a simple exponential type because nuclei in domain walls have additional shorter relaxation times. The slowest relaxation, however, is thought to be due to nuclei in domains because the intensity of the signal increased when an external field is applied perpendicularly to the rf field and a shift of resonance to a higher frequency is observed, according to [MT65]. The spin-lattice relaxation time $T_1$ increased with decreasing temperature from about 0.7 ms at room temperature to 9 ms at 130 K. At the transition point (118 K) $T_1$ decreased abruptly by the factor of about seven. It made a minimum of about 0.6 ms at 88 K, then increased with decreasing temperature up to 500 ms at 4.2 K. Above about 60 K, $T_1$ is equal to $T_2$, below this temperature $T_2$ becomes smaller than $T_1$ and is 10 ms at 4.2 K. An attempt to observe nuclear resonances of ferrous and ferric ions on the ordered B site at 4.2 K had not succeeded. The minimum of $T_1$ may be interpreted by the electron diffusion among B sites. This effect is considered to be dominant from the transition temperature to liquid-nitrogen temperature. According to Mizoguchi, the discontinuity of the relaxation time at the transition temperature suggests that the hopping frequency increases very rapidly as the order collapses and this mechanism becomes no more effective to the nuclear magnetic relaxation.

In another article [MI66] T. Mizoguchi refered to Ogawa et al.[OM62] and Boyd [Boy63] in reporting that the resonance line from the A ion is continuously detected below room temperature, while the line from the B ion disappeared at and below 120 K, in agreement with Mizoguchi's observation for the specimen with proper stoichiometry. In addition, Mizoguchi had observed the distinct resonance lines from $Fe^{2+}$ and $Fe^{3+}$ on the B sites below 14 K. These results however contradict with that of Boyd [Boy63], who found that the resonance lines from the A and B ions continue through the transition point persisted down to

temperatures of about 90 K. Mizoguchi reproduced similar data as Boyd with the use of the oxidized samples which do not show a sharp transition around 120 K in the magnetization measurement. The resonance frequency for the $^{57}Fe$ nuclei on the A site changed almost continuously from room temperature (about 67.8 MHz) to 4.2 K (70.2 MHz), though the signal intensity decreased abruptly just below the transition point. The two resonance lines Mizoguchi observed at about 69.6 and 64.7±0.5 MHz at 4.2 K are assigned respectively to the nuclei of $Fe^{3+}$ and of $Fe^{2+}$ on the B sites. Above the transition temperature of about 120 K a single line at approximately 66.4 MHz is observed for the B site, which is considered to arise from $Fe^{2+}$ and $Fe^{3+}$ narrowed by the rapidly exchanging electrons between the two valence states. At the A site, $T_1$ as function of the temperature had a minimum of about 30 ms at about 80 K, and $T_2$ had a sharp minimum of 0.4 ms at about 40 K. Above 80 K, $T_1$ and $T_2$ are roughly of the same order of magnitude. Above the transition, both $T_1$ and $T_2$ showed a magnetic field dependence. They varied nearly as the square root of the effective magnetic field, at 130 and 170 K, but at 296 K the field dependence of $T_2$ was less marked. Below the transition temperature $T_1$ and $T_2$ were independent of the field. For the B site, however, both $T_1$ and $T_2$ increased with increasing temperature from the transition temperature to about 200 K and then became almost constant, while the ratio of $T_1$ to $T_2$ stayed nearly constant ($\simeq 2$). The field dependence of the relaxation times was not observed for the B sites. The article is ended by a very elaborated theoretical interpretation of relaxation rates in the tetrahedral and the octahedral sites.

**Rubinstein** used several samples being natural single crystals of magnetite, from various localities [RF71]. All crystals examined gave identical spectra, and a synthetic powder displayed the same features, although with much less resolution. In the NMR study, besides a zero-field frequency scan, a scan at 8 kOe (0.8 T) was applied along the [100] cubic axis as the crystal was cooled through the Verwey transition to prevent c-axis twinning in the low temperature phase. Rubinstein concluded that there are obviously many more resonance lines than predicted by the Verwey model and many more than have been found in previous experiments. Since the A and B site spins are anti-aligned, the A site resonance field will shift upward in the presence of a magnetic field, and the B site resonance downward. The octahedral sublattice in the spectrum moves down in frequency when an external field is applied. The narrow intense four-fingered part of the spectrum near 70 MHz moves up in frequency with external applied field and is associated with nuclei at tetrahedral sites. The four A site peaks are unequal in both width and amplitude. According to Rubinstein this implies the existence of more than 4 inequivalent A sites in the unit cell. These four peaks can be decomposed into eight components. The B site spectrum is a complicated affair, seen as consisting of three main groupings of each having a number of inequivalent resonances. The total number of expectable resonances is 24: eight inequivalent A sites (ferrous lines) and sixteen inequivalent B sites (eight 'ferrous-like' and eight 'ferric-like' lines). It shows us the largeness and complexity of the magnetite unit cell which was earlier measured with electron diffraction in the low temperature phase[2]. Rubinstein found

[2]Rubinstein made this remark without refering to a specific publication or other kind of report.

two quite similar spectra (aside from a uniform shift) in comparing zero-field with external field NMR measurements. He stated that the complex lineshape of magnetite, therefore, cannot be attributed to a powder pattern caused by a random alignment of magnetic moments which occured in the case of a few other magnetic compounds.

Rubinstein also compared the hyperfine field spectra of magnetite in zero-field at helium temperature (4.2 K) and at room temperature (300 K) [RS73]. Several powdered samples, natural single crystals, and synthetic single crystals were used in obtaining NMR spectra. Aside from a sharper spectrum from the synthetic crystals, no differences were found between these and the best natural crystals. The function of the powders or the usefulness of their obtained spectra is not (clearly) explained in the above-cited article. Rubinstein noticed that spectra obtained from samples of poorer quality show a typical bigger spread into the gap between B site spectral segments; in extreme cases the gap was completely closed.

The resonance spectrum at 4.2 K was resolved into at least 24 lines and compared with a computer generated spectrum composed of 24 Gaussian lines of which line positions and widths are variable, though having an equal area, and are tabulated in the above-mentioned article[3]. Rubinstein concluded that when a $f^3$ correction was taken into account, it appeared that the B site spectrum is divided into two main parts of equal intensity and thus corresponds to Verwey's separation of ferrous and ferric ions. The low temperature unit cell should contain at least eight $Fe_3O_4$ molecular units.

Well above $T_V$, at 300 K, magnetite has the cubic spinel structure with two crystallographically equivalent A sites and four equivalent B sites per unit cell [RS73]. Considering the sample magnetization, however, the B sites become magnetically inequivalent and the anisotropy hyperfine fields at the trigonal B sites will according to Rubinstein split into two lines, with an intensity ratio of 3 : 1.

**Kovtun** also remarked [KS73b] the electron exchange taking place between $Fe^{3+}$ and $Fe^{2+}$ in octahedral sites above the electron ordering temperature of 119 K. In this case the symmetry of the environment of the $Fe^{3+}$ ions at the A sites is cubic, whereas the ions in the octahedral sublattices have a trigonal environment. Therefore Kovtun assumed the nuclei of the ions at the A sites to be acted upon by an isotropic field, whereas the nuclei at the B sites are acted upon by an anisotropic local field. This anisotropy is due to a hyperfine interactions and dipole fields generated at a nucleus by other dipoles in a sample. In a temperature range (from 119 K to 130 K) near the crystallographic phase transition (the Verwey transition) there should be two symmetric lines in the NMR spectrum of $Fe^{57}$ in magnetite: one due to the ions at the A sites and the other due to the ions at the B sites. Above 130 K Kovtun detected three lines using a natural single crystal of magnetite. The NMR signals due to nuclei in domains were studied because NMR spectra of nuclei in domain walls were broadened and the anisotropy of the dipole fields was difficult to detect. If the domain magnetizations coincide with the $\langle 100 \rangle$ axis the NMR spectrum of $Fe^{57}$ at the B sites should consist of a single symmetric line. If however the domain

[3]The computed A sites will later be used in discussing our own results.

magnetizations coincide with the ⟨111⟩ axis, the anisotropic field term is nonequal to zero, and the B sites should consist of two lines, whose intensities should have the ratio 1 : 3. The broadening of the NMR spectrum of the B sites in the 141-160 K range may possibly result from the superposition of three resonance lines: one line predominates at lower temperatures, whereas at higher temperatures the other two lines are stronger. From this result Kovtun concluded that the transition from one phase to the other is of the first kind. The inhomogeneous broadening of the B site lines could not be explained by the presence of electron exchange between the $Fe^{3+}$ and $Fe^{2+}$ ions at these sites for it is then impossible to explain the narrow symmetric NMR line of the cubic phase with the ⟨100⟩ easy magnetization axis.

The above-cited article only dealt with the electron ordering structure of magnetite in the temperature range 119-160 K. Another NMR investigation of electron ordering in magnetite [KSS73] in the range 77-125 K has also been published by Kovtun. This range is divided in 3 sections: above 119 K, the 117-119 K range, and below 117 K. Kovtun measured NMR spectra of the $Fe^{57}$ nuclei in a natural crystal of magnetite which consisted of two lines above 119 K and of seven lines below 117 K; in the 117-119 K range nine lines were observed. Four of the seven above-named lines were assumed to be A site positions. Of the other three two lines would correspond to $Fe^{3+}$ B sites and the remaining line to $Fe^{2+}$ B sites[4]. Kovtun showed that in the temperature range 117-119 K the spectra belonging to two phases (cubic and orthorhombic) coexist. Therefore one can conclude that the transition from the cubic (above 119 K) to the orthorhombic (below 117 K) phase and, consequently, the transition from the disordered to the ordered state is a phase transition of the first kind. An interesting feature observed by Kovtun is that the NMR frequency of the nuclei of the ions at B sites in the cubic phase is less than at A sites. This is explained by assuming a larger distance between the ions of iron and oxygen in an octahedron than the corresponding distance between the same ions in a tetrahedron. So the degree of covalent bonding of the $Fe^{3+}$ ion with the nearest oxygen ions in a tetrahedron is greater than in an octahedron. Consequently, the admixture of the s electrons to the 3d shell of $Fe^{3+}$ increases the positive contribution to the hyperfine field at the iron nuclei located at the A sites and this reduces the absolute value of the field, i.e. it lowers the NMR frequency. The hyperfine field reduction at the nucleus of $Fe^{2+}$ is assumed to have the two causes: (1) the greater degree of covalent bonding for $Fe^{2+}$ compared to $Fe^{3+}$, and (2) the incomplete freezing of the orbital moment of the $Fe^{2+}$. Therefore, the NMR frequency of the $Fe^{2+}$ nuclei is not only less than that of the $Fe^{3+}$ nuclei at the B sites, but is also less than that of the $Fe^{3+}$ at the A sites. NMR signal of the $Fe^{2+}$ nuclei could not be recorded at temperatures exceeding 85 K caused by a considerably shorter (when the temperature is raised) transverse relaxation time $T_2$ of the $Fe^{2+}$ ions than that of the $Fe^{3+}$.

Another article published by Kovtun dealt with the magnetite $Fe^{57}$ NMR spectra data obtained at several temperatures[5] in the range 4.2-200 K [KS73a]. Both natural and synthetic single crystal samples were examined. Furthermore, the temperature dependences of

[4]The matching resonance frequencies are not given in this short review but were mentioned as function of the temperature nearby the phase transition in the above-cited article [KSS73].

[5]Only the NMR spectra of nuclei in domains at T = 185 K, T = 130 K, and T = 4.2 K were shown in

some magnetite NMR frequencies were obtained and the signals as from nuclei in domains and so from domain walls were investigated and their attribution was defined from the study of the *enhancement factor* and *relaxation times.* According to Kovtun the enhancement factor of signals from nuclei in domain boundaries is about 11 times higher at T = 4.2 K and about 117 times higher at T = 125 K and the spin-lattice relaxation time is 40 times lower at T = 4.2 K and 120 times lower at T = 125 K than those of the signals from nuclei in the domain. One line from tetrahedral A site ion nuclei and two lines with the intensity ratio 1 : 3 from octahedral B site nuclei were observed at temperatures higher than 160 K. This intensity ratio tells us that the magnetization direction in domains coincided with the ⟨111⟩ axis. In the temperature range 119-136 K only one line from ion nuclei of A site were observed and one line from ion nuclei of B sites. At 136-160 K the octahedral site spectrum consisted of an unhomogeneously broadened line. The form of this line changed from almost symmetrical at 141 K up to strongly asymmetrical at higher temperatures. The broadened line was presented by Kovtun as a possible superposition of three lines, two of which were observed at temperatures higher than 160 K and the third one at a temperature lower than 136 K. When using a long enough time interval (10 ms) between excited pulses, lines in parts of the measured spectrum were not observed. B site ions ($Fe^{3+}$) of the nonhomogeneously broadened line have a transverse relaxation time much longer ($T_2$ = 20 ms) than that of the rest ($Fe^{2+}$) of the B ions (1.5 ms). The determination of the total amount of $Fe^{2+}$ lines caused by nuclei in A sites was claimed by Kovtun to be 16 when one compares the intensities of all lines to each other and might consider that each of the eight observed lines is a doublet. The frequencies and line widths of the lines arising from iron atoms at the A sites given in the article [KS73a] will here not be discused for they will be used furtheron in this chapter for comparing our own measured NMR spectra. The ion ordering of bivalent and trivalent Fe ions took place not only along the crystal c-axis (as proposed by Verwey) but also along a- and b-axes. Kovtun ended his conclusions with the remark that the magnetite unit cell must have at least 16 $Fe_3O_4$ molecular units in orthorombic phase.

**M. Mizoguchi** intensively studied NMR spectra of the *low* temperature phase [Miz78a] (at liquid helium temperature and at 1.4 K). In a later publication [MI80] the findings from the just mentioned article were resumed. The Verwey model could not be correct according to Mizoguchi[6]. A single crystal specimen was cut and shapen into a cylinder (18 mm diameter and 41 mm in length) with its axis parallel to the $\langle 12\bar{1} \rangle$ direction. For the low temperature phase the indices of the pseudo-cubic unit cell of a spinel structure in which the magnetically easy axis (c-axis), the intermediate axis (b-axis), and the hard axis (a-axis) are taken along the [001], [110], and [$1\bar{1}0$] directions, respectively. Mizoguchi did use two different magnetic coolings. The first one was to cool the crystal through the Verwey transition temperature with a magnetic field of 15 kOe (1.5 T) along [113]; the second one

the above-mentioned article.

[6]To emphasize this incorrectness Mizoguchi refered to unpublished neutron diffraction study and Mössbauer studies, and also to the just-discussed articles of NMR studies done by Rubinstein and Kovtun.

was carried out in the same manner as described for the first one with exception of the field axis which was in this case [$\bar{1}$23]. The first cooling caused the a-, b-, and c-axes to be [1$\bar{1}$0], [110] and, [001] respectively, whereas in the second case they were [110], [$\bar{1}$10], and [001] respectively. Mizoguchi stated that the enhancement factor in domain walls is much stronger than that in a domain and the spin-lattice relaxation time of the nuclei in the domains is much longer than those in the domain walls, as Kovtun already had confirmed. The signal from domain walls can be eliminated by applying an external magnetic field (for the A sites at least 0.3 T). In this circumstance the field dependence of the NMR frequency of the $Fe^{3+}$ ions on A sites corresponds to the gyromagnetic ratio for free $Fe^{57}$ nuclei: 1.38 MHz/T). The specimen has the unique a-, b-, and c-axes established by field cooling. Mizoguchi tabulated 7 trivalent A site spin-echo resonance frequencies and 14 (5 trivalent and 9 bivalent) B site resonance frequencies. The A site data are used to compare with our own results in the oncoming section. The field dependences of most of the lines on B sites were reported as non-linear. The line widths of trivalent iron ions in B site lines were not broadened by upon applying an external field in contrast with the behaviour of the rest of the B site lines which is similar to that of A site lines. While applying an external field of 6 kOe Mizoguchi rotated this field 360°. A dependence of the resonance frequency upon the direction of the external field (at 1.4 K) was seen for the frequencies of the $Fe^{3+}$ ions on B sites ($1 \sim 3$ MHz) and on A sites (less than 0.2 MHz) and splittings were seen of the 5 trivalent B sites being 3 quartets and 2 doublets. But the variations of the resonance frequencies of the $Fe^{2+}$ ions on B sites are far most the largest (about 5 MHz). The signals from $Fe^{2+}$ ions were weak and the width of the lines increased with the increase of external magnetic field. The magnetic energy and its components (the applied field energy, the magnetocrystalline anisotropy, and the demagnetization energy) were also discussed. In respect to the magnetocrystalline anisotropy component Mizoguchi introduced the term monoclinic twinning. This is the case when magnetocrystalline anisotropy is so large that the magnetization cannot smoothly follow the external field but flips near the a-axis. Resonance lines will not split under the presence of this monoclinic twinning, because the difference of the directions of the magnetization in two regions is expected to be less than 5°. The above-discussed angular dependence led M. Mizoguchi to the following [Miz78b] conclusions:

**1** Five inequivalent sites exist for $Fe^{3+}$ ions on the octahedral sites;

**2** Each resonance line associated with the $Fe^{3+}$ ions in the inequivalent B sites splits into two or four lines under the external magnetic field, owing to the different directions of the principal axis of the anisotropic internal field.

Furthermore, Mizoguchi has attempted to describe the ordering structure [Miz78b] (with some minor adjustments and supplements by later publications, like in [IMM+82] and [Miz85b]) by posing the following 4 assumptions:

**I** The principal component of the anisotropic hyperfine fields is the magnetic dipole field from the cations in the crystal (experimental evidence: [Miz78a]);

**II** For $Fe^{3+}$ ions on B sites, the electron distribution on the six nearest neighbour B sites determines the *symmetry* and the *magnitude* of the internal magnetic field;

**III** Every unit tetrahedon of B sites always has two $Fe^{2+}$ and two $Fe^{3+}$ ions (due to the strong Coulombic interaction between electrons: [ZSP90]);

**IV** Equal populations of $Fe^{2+}$ ions and $Fe^{3+}$ ions are present on every c-plane (hard magnetization plane).

The anisotropic part of the hyperfine field of $Fe^{3+}$ ions will be produced both by the dipole fields of the other ions and the dipole field of itself (assumption I). Assumption II means that the dipole fields both from other ions and from itself are determined entirely by the symmetry of the nearest neighbour electron assignment. Assumption III is also known as the Anderson condition due to the large shielding effect of the electrostatic interaction in magnetic oxides.

Zuo et al. [ZSP90] intend to describe the electron ordering by using besides this Anderson condition the monoclinic symmetry of the low-temperature structure of magnetite. So, although the ionic arrangement remains according to the just-cited article (experimentally) unknown, ten models for ionic arrangements (one of which is the Verwey model !) are being found by combining these two assumptions. However, none of these satisfy the additional assumptions (I, II, and IV) of Mizoguchi.

These four assumptions lead to the essentially unique electron ordering along the c-plane. But according to Mizoguchi, other electron orderings, e.g. $Fe^{2+}$ ion and $Fe^{3+}$ ion align alternately on the a-line and the b-line, cannot be eliminated at the present stage [Miz85b] by the NMR study alone. Mizoguchi further remarked that no anomaly was found in measurements of lattice constants and NMR frequencies and in the differential thermoanalysis. In summary, the atomic positions below the transition temperature are now approximately known and the Verwey model has been disproved (by Mizoguchi [Miz85a]) while this model is one of ten possibilities in an article of Zuo et al. [ZSP90].

Since the so-called Verwey order model was disproved in the low temperature phase of magnetite, many studies have been carried out to reveal a true structure model of the low temperature phase. In this process, anomalies were reported at about 10 K in measurements of magnetiziation, specific heat, magneto-electric effect, etc. So among other things the temperature dependence of several resonance lines of magnetite [YMI81] (with [IMU+80] as a short preliminary article with regard to the study of the low temperature phase) was investigated from 4.2 to 20 K. Kovtun's measurements indicated no abrupt change of the NMR frequencies at about 10 K. The data, however, were according to Mizoguchi insufficient because of the lack of special attention which should have been paid to this problem at about 10 K. A second reason for NMR measurements on magnetite was that one of the five assumed $Fe^{3+}$ (B) lines (B-4 line in Mizoguchi's terminology[7]) was not

[7]This line has a resonance frequency at 69.36±0.01 MHz between 4.2 and 20 K [YMI81]. It is situated in the left slope of the A sites spectrum which can be a cause of a less detectability.

reported. In the above-cited article a single crystal rod was grown and had a cylindrical form 15 mm in diameter and 40 mm in height with its axis parallel to the [210]. A part of the experiments were performed after the specimen was annealed for about 11 days at 720°C in an evacuated quartz tube. Verwey temperatures, determined by the magnetization or the electric conductivity measurements, before and after the annealing, were 119 K and 121.5 K, respectively. On cooling the specimen through the Verwey temperature, a magnetic field of 14 kOe (1.4 T) was applied in the (210) plane at an angle of 35° from the [001] axis. The resonance lines became sharper and stronger by this cooling treatment with the magnetic field. In magnetite, as was already known, one can clearly distinguish the spin-echo signals in the domain from those in the wall by adjusting the amplitude and/or the width of exciting pulses, since the enhancement factor in the domain is considerably different from that in the wall. Thus one could observe the spin-echo signals in the domain even when the measurements were made without an external magnetic field. Yanai et al. [YMI81] reported an almost identical spectrum as the one observed by Mizoguchi [Miz78a]. The line shapes were just slightly different. Yanai concluded that line shapes are dependent upon each specimen. Actually, after the specimen was annealed, the resonance lines became narrower. The center of lines, however, didn't change before and after the annealing. All the measurements, except for the so-called B-4 line, were performed without an external magnetic field. When the B-4 line was measured, an external field of 4 kOe (0.4 T) was applied to the [001] axis in order to separate it clearly from $Fe^{3+}$ (A site) lines. For narrow lines (all A site lines and the so-called B-1 and B-2 lines) the frequency decreased gradually by about 0.015 MHz (0.02 %) from 4.2 to 19 K. For all other lines, any change couldn't be detected due to the broader line width which caused the accuracy of the measurement to be a minor influence. The half width decreased slightly as temperature rose. It is not clear whether this decrease is essential or not, i.e. merely due to the reduction in signal to noise (S/N) ratio, but no abrupt change in the line width was found at about 10 K. Temperature dependence of the spin-echo signal was also investigated and measurements were made with fixing the frequency at the peak of each line at 4.2 K. Yanai concluded that the intensity of a spin-echo signal is proportional to the nuclear magnetization (because the echo intensity decreased approximately as $\frac{1}{T}$, which is proportional to the reduction in the nuclear magnetization) so that the amount of resonant nuclei and thus the amount of the ions that belong to each different site did not change remarkably through about 10 K. Yanai also measured relaxation times after annealing at 4.2 K. The spin-lattice relaxation time ($T_2$) for the 5 measured $Fe^{3+}$ B site lines (B-1 to B-5) vary from 5.2 to 36.6 ms. For the $Fe^{3+}$ A site line (at 69.605 MHz) and $Fe^{2+}$ B site line at 48.86 MHz (the by Yanai called B-$II_L$ line) $T_2$ has the value of 32.4 ms and 10.6 ms, respectively. Only the spin-lattice relaxation time of the B-$II_L$ line was also measured before annealing: 5.7 ms. All other lines were compared with $T_2$ values gained by Kovtun et al. [KS73a], although Yanai later stated that the spin-lattice relaxation is dependent upon each specimen. The relaxation times ($T_1$ and $T_2$) of the annealed samples were also obtained as a function of the temperature between 4.2 and 19 K. Yanai described the temperature dependence of the spin-spin relaxation time ($T_1$) as, roughly spoken, being an activation type (with activation energy 4±1 K) and almost similar for different sites while $T_2$ seemed to be proportional to

$T^{\alpha}$ with $\alpha = 1 \sim 1.5$ for different sites.

It is thus concluded that the frequencies of all the lines observed by Yanai had no anomaly from 4.2 to 19 K within the accuracy of 0.05%. The decrease of the frequencies by 0.02% for the narrower lines could be attributed to the temperature reduction in the electronic magnetization. The five inequivalent $Fe^{3+}$ B sites found at 4.2 K, which are crucial to the ionic ordering model proposed by Mizoguchi, were also observed above 10 K. The echo intensity of each of these lines also had no abrupt change at about 10 K. From this it is concluded that the ionic ordering is not effected by the anomalies at about 10 K.

## 4.3 Results and discussion

Two magnetite samples have been investigated with NMR (see table 4.2). We first have measured the sample with the largest volume of $Fe_3O_4$ to ensure optimization of experimental parameters, like puls widths ($p_1$ and $p_2$), delay times ($d_1$, $d_2$, and long delay), frequency (f), rf power, and so on.

Sample SP698 is grown at EUT. It is a single crystal and non-stoichiometric, i.e. oxidized, specimen. It is shapen into a [100] oriented cylinder 15.9 mm in length and 4.9 mm in diameter. The atmosphere used in the oven to grow the sample consisted of nearly pure (99.9 %) $N_2$.

Sample RW1280 is made at Philips Research Laboratories and has a length of 13 mm, a width of 9 mm and a total thickness of 1.5 mm. It consists of a MgO [100] substrate on which a thin layer of 1150 Å magnetite is grown at 250°C using Molecular Beam Epitaxy (MBE) in an oxide atmosphere of $2.8 \cdot 10^{-5}$ mbar.

| sample number | description (shape) | dimensions [mm] | volume $Fe_3O_4$ [$mm^3$] | composition |
|---|---|---|---|---|
| SP698 | cylinder | l = 15.9<br>d = 4.9 | 300 | $Fe_3O_4$ |
| RW1280 | thin film | l = 13.0<br>w = 9.0<br>h = 1.5 | 0.0135 | MgO(100) + 1150 Å $Fe_3O_4$ |

Table 4.2: *Some characteristics of the magnetite samples which have been measured with NMR. In this table l stands for length of each sample, d for the diameter of the cilinder, w for the width, and h for the height (total thickness) of the thin film.*

### 4.3.1 Cylinder $Fe_3O_4$

Figure 4.3 (a) shows the NMR spectrum of the cylindrical magnetite sample obtained at **room** temperature (293 K). The peaks between 62.0 MHz and 64.0 MHz are due to octahedral (B) sites ($Fe^{2+}$ and $Fe^{3+}$). These B sites are in agreement with the interval from 62.8 to 63.6 MHz found by Boyd [Boy63] and also correspond to the frequencies and shape (3 : 1 intensity ratio caused by coincidation of the magnetizations with the $\langle 111 \rangle$ axes according to Kovtun et al. [KS73b] at T = 185 K, and thus above the Verwey transition) of the B sites measured by Rubinstein et al. [RS73]. One should keep in mind, however, that our NMR measurements are frequency scans in a small frequency range, and optimized in only one (central resonance) frequency. Furthermore, our own measured spectrum, shown in figure 4.3, is corrected for (transmitting) enhancement but the obtained datapoints are not smoothed nor frequency-corrected. Between 59 and 61 MHz the NMR spectrum shows an unexplainable large noise fluctuation. The NMR spectrum also shows an increase in intensity at room temperature nearby the resonance frequencies 67.6 and 67.9 MHz due to the A site environments. Only the latter frequency is also found in early magnetite NMR experiments [Boy63, RS73].

In figure 4.3 (b) the same NMR spectrum of sample SP698 at room temperature is shown. The only two changes are the limited frequency interval (61 to 69 MHz) and the additional datapoints and lines from (bulk) magnetite NMR measurements of some of the above-cited (co-)authors. The width of the A site line is relatively sharp determined when one compares it with the B site signal. The echo signal caused by octrahedral ions is a very broad distribution of resonances, principally being due to a dipolar magnetic field acting on these ions due to the rest of the magnetic lattice and anisotropy of the hyperfine field interactions [BS62, KS73b].

Ogawa et al. observed on the other hand also two resonances at room temperature (300 K): the A site and the B site at frequencies of 67.621 MHz and 63.549 MHz respectively [OM62]. In this paper it is said that the A site has a very good (not specified) signal to noise ratio and that the B site has a lower intensity because of the large line width (also not specified), which is considered to result from the electron diffusion between $Fe^{3+}$ and $Fe^{2+}$ in B site.

Figure 4.4 (a) shows the NMR spectrum of the cylindrical magnetite sample obtained at **liquid helium** temperature (4.2 K). The measured spectra shown in figure 4.4 are corrected for (transmitting) enhancement but their obtained datapoints are not smoothed nor frequency-corrected. The intense peaks are caused by A site nuclei. The A sites are described in literature[8] as a superposition of 8 lines. B sites are also detected and widely spread over the frequency range. In figure 4.4 (b) the A and B site lines are only an enlarged representation of (a). The upward pointing arrows in the figure are NMR data taken from an article of Mizoguchi [Miz78a]. The NMR spectra are also compared with other magnetite spectra obtained by spin-echo experiments at 4.2 K. The spectra of Kovtun et al. [KS73a] and Rubinstein et al. [RS73] are simulated by the intensities, widths

[8]See the literature review in the preceding section.

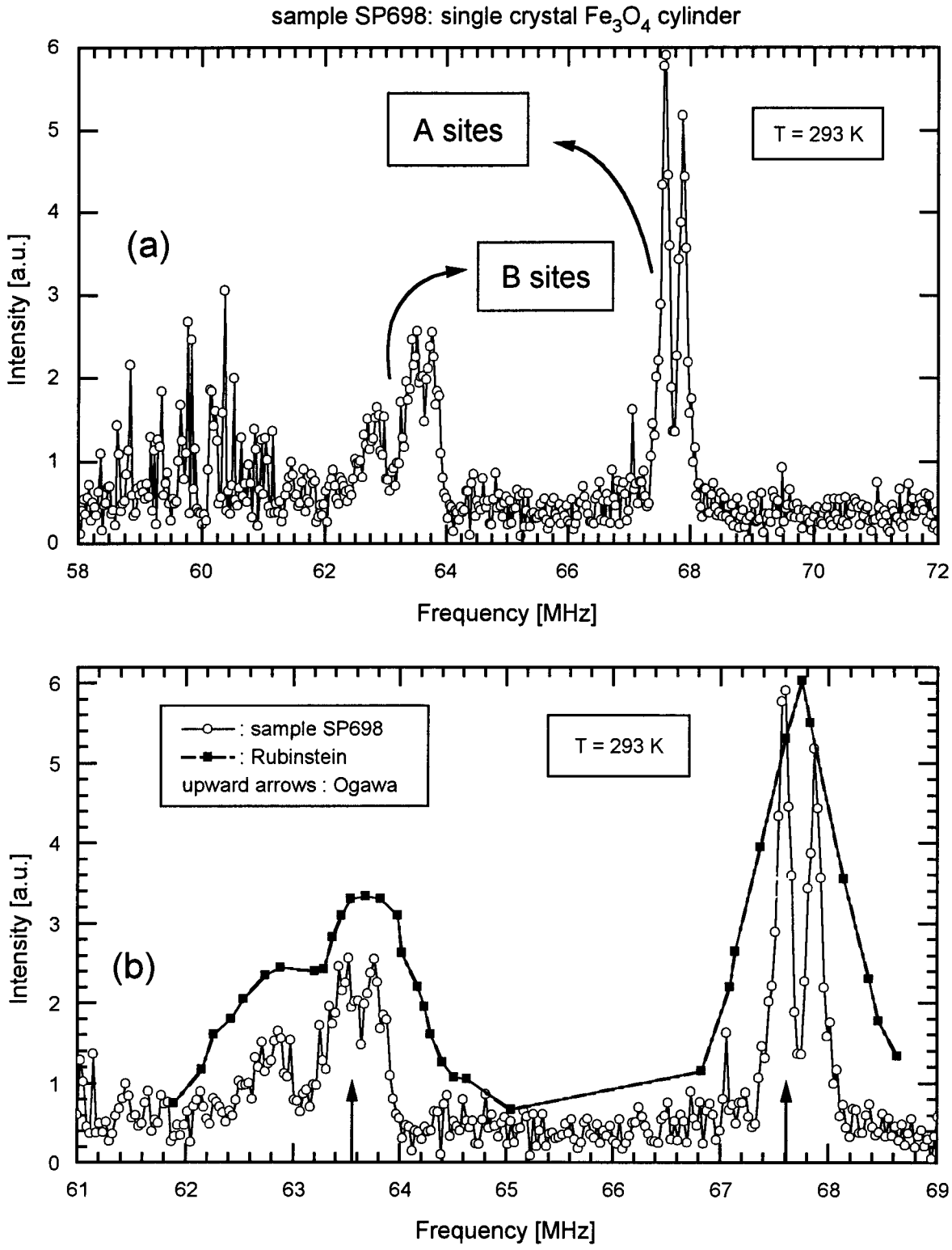


Figure 4.3: *A NMR spectrum of magnetite sample SP698 at $T = 293$ K. This sample has a single crystal structure. The spectrum is obtained by a frequency scan as described by section 3.3. The upper spectrum is a respresentation of the total scan, the lower spectrum is a segment of the upper. Ogawa et al.* [OM62] *found resonance peaks at 63.5 and 67.6 MHz while Boyd* [Boy63] *measured peaks at 63.3 and 67.9 MHz.*

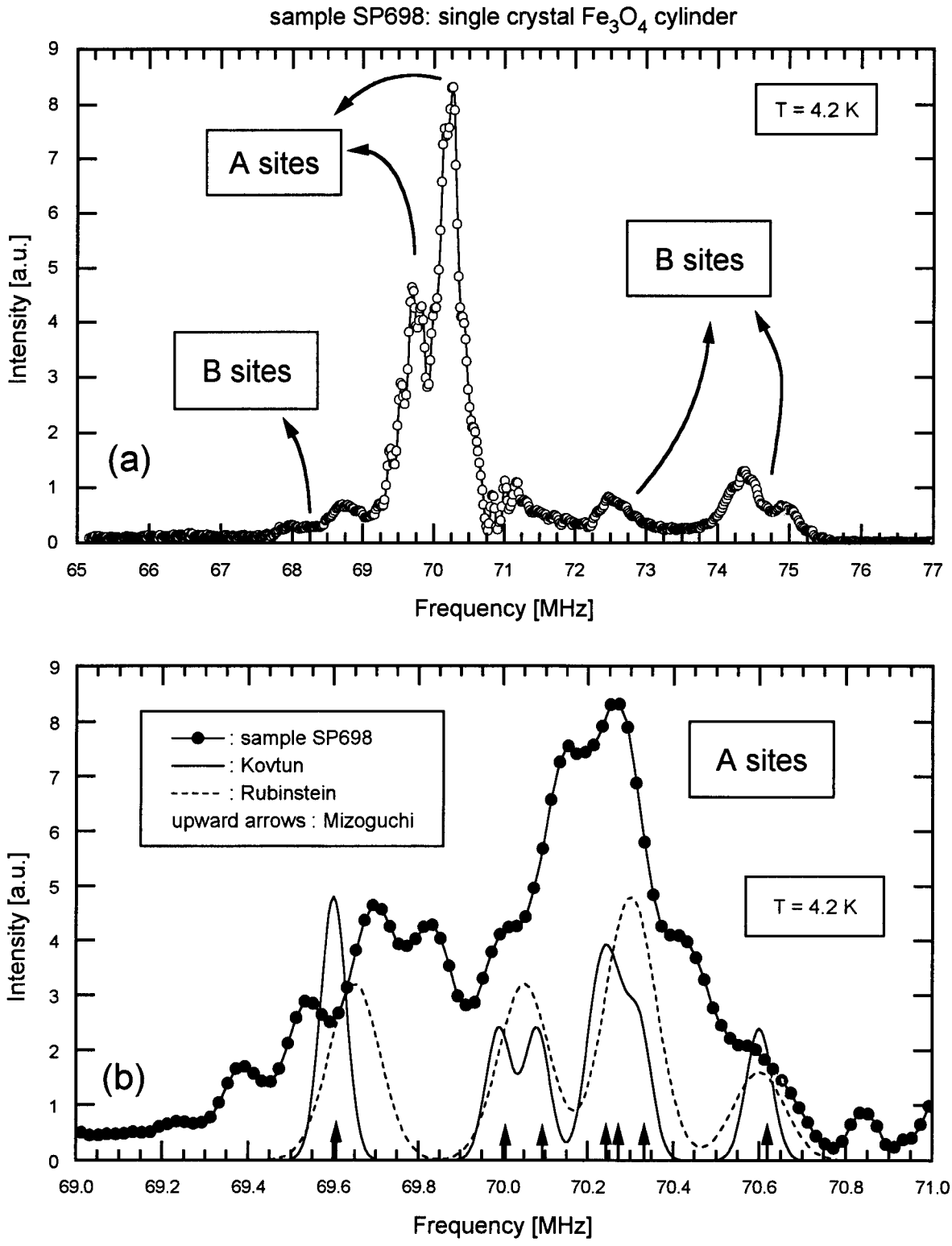


Figure 4.4: *The NMR spectrum of magnetite sample SP698 at $T = 4.2$ K. This sample has a single crystal structure. The spectrum is obtained by a frequency scan as described by section 3.3. The upper spectrum is a representation of the total scan, the lower spectrum is an enlargment of the upper spectrum showing the A sites and comparing experimental NMR spectra obtained by Mizoguchi* [Miz78a], *Rubinstein et al.* [RS73], *and Kovtun et al.* [KS73a].

and positions given in their articles. In figure (b) there is a discrepancy between the NMR spectrum of the present sample and the A site spectra of Kovtun et al. and Rubinstein et al. Part of the differences are caused by the fact that the experimental spectrum also contains contributions of B sites. Besides the theory of superposition of 8 lines (forming the total A site) also B site lines influence the spectrum by overlapping at least partially the A site spectrum at 69.51 and 70.89 MHz ($Fe^{3+}$: $B_4$ line and $Fe^{2+}$ respectively [Miz78a]) and at 69.8 and 70.8 MHz ($Fe^{3+}$ assumed [RS73] for both lines). Another cause is possibly the non-stoichiometry of the sample invoking a difference in the expected intensity ratio between the specific resonance lines. The reflection of the LC circuit was furthermore minimized at 70.2 MHz and is plotted as a function of the frequency in appendix A. The used method for measuring the spectra gave us positions of resonance frequencies but no reliable information about intensity ratios.

| publication | $T_2$ [ms] | frequency [MHz] | remarks |
|---|---|---|---|
| [MT65] | 10.0 | A site | |
| [MI66] | $2 \cdot 10^1$ | A site | extrapolation |
| [YMI81] | 32.4 | 69.605 | after annealing |
| SP698 cylinder | 8.4±0.6 | 70.22 | |
| $Fe_3O_4$ | 6.9±0.4 | 70.20 | |

Table 4.3: *Spin-spin relaxation time ($T_2$) at T = 4.2 K obtained by NMR spin-echo.*

The spin-spin relaxtion time ($T_2$) is measured at T = 4.2 K for A site nuclei at 70.20 MHz: $T_2 = 8.4 \pm 0.6$ ms and at T = 102 K for A site nuclei at 69.83 MHz: $T_2 = 6.9 \pm 0.4$ ms. In table 4.3 we compare our measurements with values from the literature. Due to a lack of $T_2$ measurements by T. Mizoguchi [MI66] for $T \leq 20$ K, one has to extrapolate the measured data between helium temperature and 40 K in a semi logaritmic figure, causing a deviation of about 50%, i.e. 10 ms. The different value of 32.4 ms obtained by Yanai et al. [YMI81] is probably due to the annealing treatment which might have caused a change in structure and consequently a change in spin-spin relaxation time.

### 4.3.2 MgO + 1150 Å $Fe_3O_4$

In figure 4.5 a NMR spectrum at T = 1.6 K of thin film sample RW1280 having a magnetite volume of 12.3 mm × 8.9 mm × 1150 Å (0.013 $mm^3$) is plotted. Compared to the NMR

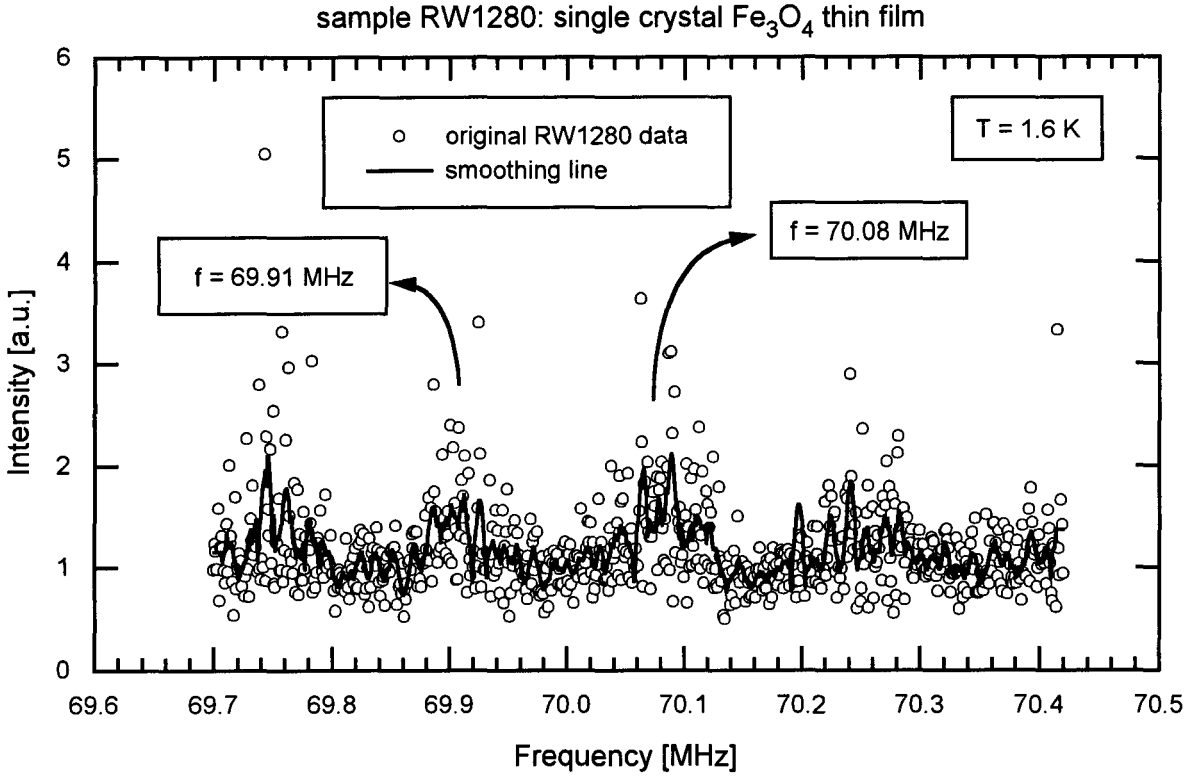


Figure 4.5: *The NMR spectrum of magnetite sample RW1280 at T = 1.6 K. This sample has a 1150 Å thin layer of magnetite. The spectrum is obtained by a frequency scan as described in section 3.3. Only two of four 'visible' lines (at 69.75, 69.91, 70.08, and 70.24 MHz) are most likely to be real lines due to the A site of magnetite: 69.91 and 70.08 MHz.*

magnetite spectrum of the cylinder sample SP698 shown in figure 4.4 only two (probably) A site lines at 69.91 and 70.08 MHz were detectable in the NMR spectra of the magnetite thin film.

The signal is of the same order of the noise. Therefore, we distinguish, although it might be very difficult, the A site resonance lines at 69.91 and 70.08 MHz of the total of four assumed lines due to the knowledge of figure 4.4 and of some articles mentioned in the literature review [RF71, RS73, KSS73, KS73b] dealing with temperature dependence of the several resonance lines nearby 70 MHz due to nuclei in A and B sites. A signal to noise (S/N) ratio of about 1 means that we have acquired a measure for the detection limit of our experimental setup in obtaining $Fe^{57}$ NMR in magnetite: a magnetite volume of 0.013 $mm^3$ at T = 1.6 K having a natural iron composition (2% $Fe^{57}$).

The NMR spectra obtained by Mizoguchi [Miz78a] are carried out at T = 4.2 K with a single crystal cylinder having a magnetite volume of 10,400 $mm^3$. This information indicates that we likely will have less signal (several orders at least) from our two samples compared to the Mizoguchi sample. We therefore first experimented with the sample RW1280 (containing the largest amount of magnetite): a cylinder having a volume of 300

$mm^3$. A clear NMR spectrum of magnetite was succesfully obtained.

Because magnetoresistance, Mössbauer spectroscopy, electron spin resonance, and other experimental methods are used for studying magnetite multilayers our task was to determine the dectectability of a similar multilayer having a magnetite volume of only 0.013 $mm^3$ in 1.6 K (which is simular to a magnetite volume of 0.034 $mm^3$ at 4.2 K !). This means that the S/N ratio of sample SP698 is about $8.8 \cdot 10^3$ times larger than that of sample RW1280.

### 4.3.3 Discussion

The sensitivity of NMR spectra has reached its limit by using a thin film magnetite (sample RW1280). Improving the S/N ratio the echo signal by lowering the temperature is not an option, because the 1.6 K is the thermal limit for our NMR equipment. One solution might be obtaining enriched magnetite. This magnetite consist of iron having a much higher abundance than that of natural iron (for example 90% $Fe^{57}$ [Boy63] in stead of 2%). Another - very time consuming - option is to average more identical spin-echo experiments.

Besides combining these solutions to improve the signal noise to ratio, there is perhaps a serious alternative: NMR experiments on $Co_xFe_{3-x}O_4$ [DMI+81, KKPS82, TOY74]. Its advantage is the measurement of the spin-echo signal of $Co^{59}$ having a much larger sensitivity than $Fe^{57}$ (see table 4.1).

In spite of the above-named improvements in order to enlarge the detection of magnetite like structure it will always be a challenge to get as much information as possible from a ($Fe_3O_4$) structure having 24 (8 $Fe^{3+}$ A site lines, 8 $Fe^{3+}$ B site lines, and 8 $Fe^{2+}$ B site lines) different surroundings. Besides the small dimensions of the sample, this diversity of the magnetite structure causes a difficulty in detecting interfaces influences but does not need to destruct information to determine the quality of the researched thin film.

One also should keep in mind that the surroundings can be discriminated from each other not only by the magnitude of the resonance frequency but also by various other things such as: relaxation values $T_1$ and $T_2$ [YMI81], external field dependencies (i.e. gyromagnetic ratio) [RF71], anisotropy, and temperature dependency of the hyperfine field [Miz78a].

# Chapter 5

# Electrodeposited Co/Cu multilayers

*In this chapter results of NMR experiments of electrodeposited Co/Cu multilayers and Co films will be shown. We will begin with an introductory section explaining the background of the renewed interest in electrochemical deposition. Section 5.2 deals with NMR measurements on thick Co films giving us information about the alloy structure of the Co bulk part in Co/Cu multilayers. Section 5.3 deals with NMR measurements on [100] textured (15 Å Co + y Cu) and both [100] and [111] textured (x Co + 40 Å Cu). Section 5.4 contains NMR measurements on Co/Cu multilayers grown with the addition of leveling agents to the electrolyte and discusses its effects on the multilayer structure. This chapter ends with section 5.5 summarizing and discussing the main conclusions and results.*

## 5.1 Electrodeposition

In the past years magnetic multilayers have been the subject of intense scientific effort, which is mainly due to the interesting magnetic and electrical phenomena of which some are dealt with in chapter 1. To obtain these properties, specific artificially layered structures are wanted and a fair control over the deposition parameters is needed. That is why most of the samples exhibiting interesting properties have been prepared by sputtering, molecular beam epitaxy (MBE), and other (high) vacuum-based techniques [BH94]. These growing methods give us qualitatively good results, but are expensive and complicated. A promising alternative has been elaborated: electrochemical deposition in an electrolyte.

Electrodeposited multilayers were first made in 1921 [Blu21]. The smallest reproducable thickness in the Cu/Ni multilayers was 6.3 $\mu$m for one Ni layer and 63 $\mu$m for one Cu layer. Although one principally should speak of thick films in stead of multilayers, these first electrodeposited samples were structurally well defined. Due to a renewed interest in electrodeposited multilayer results (an improvement of growth homogeneity and thickness control has been established) [RCdB91, HCR92], Philips Research Laboraties and EUT,

amongst others, have started recently improving electrodeposition equipment, experimenting with electrolytes of all sorts of mixtures, and finally growing electrodeposited Co/Cu multilayers showing large magnetoresistance values [LSGdJ95, Met95]. Furthermore, electrodeposition offers the promising possibility of growing wire-like multilayer structures with very large height-to-width aspect ratios [BMDA94, PGD+94], which enables the study of the current perpendicular to plane (CPP) GMR effect.

Electrodeposition (also called electroplating) is carried out with several techniques, which one might roughly split up into two methods: (1) the *single bath* method and (2) the *double bath* method. The former method is deposition of two different materials in one and the same bath (electrolyte) by a periodic variation of a deposition parameter. The latter method implies a deposition of two different materials by submerging the substrate in two separate baths. There are a large number of growth parameters which can be varied, such as the substrate texture, growth rate (by changing the deposition voltage and/or $Cu^{2+}$ and $Co^{2+}$ ion concentrations), and the use of additives (leveling agents).

The magnetic Co/Cu multilayers, measured in the following sections, are grown in an electrolyte containing both $Co^{2+}$ and $Cu^{2+}$ ions (single bath method) with the composition controlled by periodically switching the potential of the substrate. This process is called *pulsed potentiostatic deposition.* The aqueous electrolyte is based on $CoSO_4$ and $CuSO_4$. The copper concentration is relatively small compared with the amount of cobalt in the electrolyte. Electroplating is done in a teflon cell with the substrate (cathode) facing upwards. There is no separate compartment for the counter electrode (anode) which is a Pt plate of about 10 $cm^2$. A saturated-calomel electrode (SCE) was used as a reference for the applied potential. This electrode is placed about 7 mm above the substrate. The center part of the substrate is exposed to the electrolyte via an O-ring seal of size 9 mm in diameter which determines the growth area. The effective growth diameter is somewhat smaller (about 7.5 mm) because of boundary effects. All substrates used originate from 4-inch Si(100) wafers which are segmented by grooves into pieces of size 14 $\times$ 14 $mm^2$. The multilayers used differ in base layer which has been evaporated onto Si wafers prior to electroplating: a 500 Å Au film electron-beam evaporated at a rate of 3 Å/s and a 200 Å Cu film magnetron sputtered at a rate of 2 Å/s. During sputtering or evaporation of the base layer the Si wafer remains at room temperature. The major difference between the two base layers is a difference in crystallographic orientation. The Au base layer exhibits a strong [111] texture in contrast to the Cu base layer which is predominantly [100] oriented.

The growth procedure for, specifically, the Co/Cu multilayers is as follows. First the potentiostat is turned on at the electrode potential $U_{Cu}$. After a delay of about 30 s the Cu-diffusion layer has been built up. The "delay" of 30 s is caused by the non-equilibrium in the beginning of the redox reaction and the low concentration of $Cu^{2+}$ ions limiting the reduction rate by mass transport (diffusion and convection). The total charge due to $Cu^{2+}$ reduction during this initial phase corresponds to an initially grown Cu layer of approximately 100 Å in thickness. Secondly, the procedure is continued with a pulse at potential $U_{Co}$ during a time $\tau_{Co}$ to deposit the Co layer followed by a longer period $\tau_{Cu}$ at potential $U_{Cu}$ to plate the Cu layer. This Co/Cu-cycle is repeated 50 times. The individual

thicknesses of the Co and Cu layers are controlled by the integration of the charge $Q_{Co}$ and $Q_{Cu}$ during the time intervals $\tau_{Co}$ and $\tau_{Cu}$, respectively. An extra check for determinating these thicknesses is a combined use of a Vibrating Sample Magnetometer (VSM) and X-ray Diffraction (XRD). The first determines the total magnetic moment, the latter gives us the average thickness of the Co/Cu bilayer repetition. For more information about the growing conditions, structural qualities, and magnetic properties of some of the examined samples see [LSGdJ95].

## 5.2 Thick Co films

The basis for the use of NMR in structural investigations of ferromagnetic materials lies in the fact that the hyperfine field experienced by a nucleus, hence its resonance frequency, is strongly dependent on the nature and number of atoms (or moments) in its neighbourhood. However it is quite hard, if not impossible, to achieve *ab initio* calculations of hyperfine fields for given atomic configurations of elements in a solid material and particularly in metallic alloys [MPL92]. Therefore, one has to rely on reference measurements on samples of known structure and composition which are hopefully close to the one under investigation. Thus, in order to analyze the spectra in terms of local structure, we have first measured bulk Co-Cu alloys, i.e. Co films grown in a Co-Cu bath, as references.

Though magnetic Co/Cu multilayers only might produce the desired magnetic and electric properties (like GMR), our purpose of examening thick Co films is obtaining more information about the alloy structure of the bulk part of the Co layers in the just-mentioned Co/Cu multilayers. To achieve this, samples have been made which allow us to examine the influences of *three different parameters* by NMR separately:

**1** Different base layers (200 Å Cu or 500 Å Au);

**2** Varying Co film thickness (1000 Å or 7000 Å);

**3** Electrolytes containing only $Co^{2+}$ ions or both $Co^{2+}$ and $Cu^{2+}$ ions (Co bath or Co-Cu bath respectively).

### 5.2.1 The base layer

In figure 5.1 (a) the NMR spectra of two samples, which differ only in base layer, are shown. The samples consist of a Si(100) substrate, a base layer of either 200 Å Cu or 500 Å Au, and have an approximately 7000 Å thick Co layer on top of the base layer. The samples are grown in an electrolyte containing both $Co^{2+}$ and $Cu^{2+}$. We see that the bulk part, i.e. Co surrounded by 12 Co nearest neighbours and causing resonance peaks at hyperfine fields larger than about 21 T, consists of two phases: mainly fcc Co (about 21.5 T) and a small part hcp Co (about 22.6 T). Besides these phases, stacking faults (sf) are also present (around 22.1 T). The non-zero intensity at hyperfine fields lower than 21 T is caused by satellite lines, i.e. a Co atom surrounded by some Cu atoms in the nearest

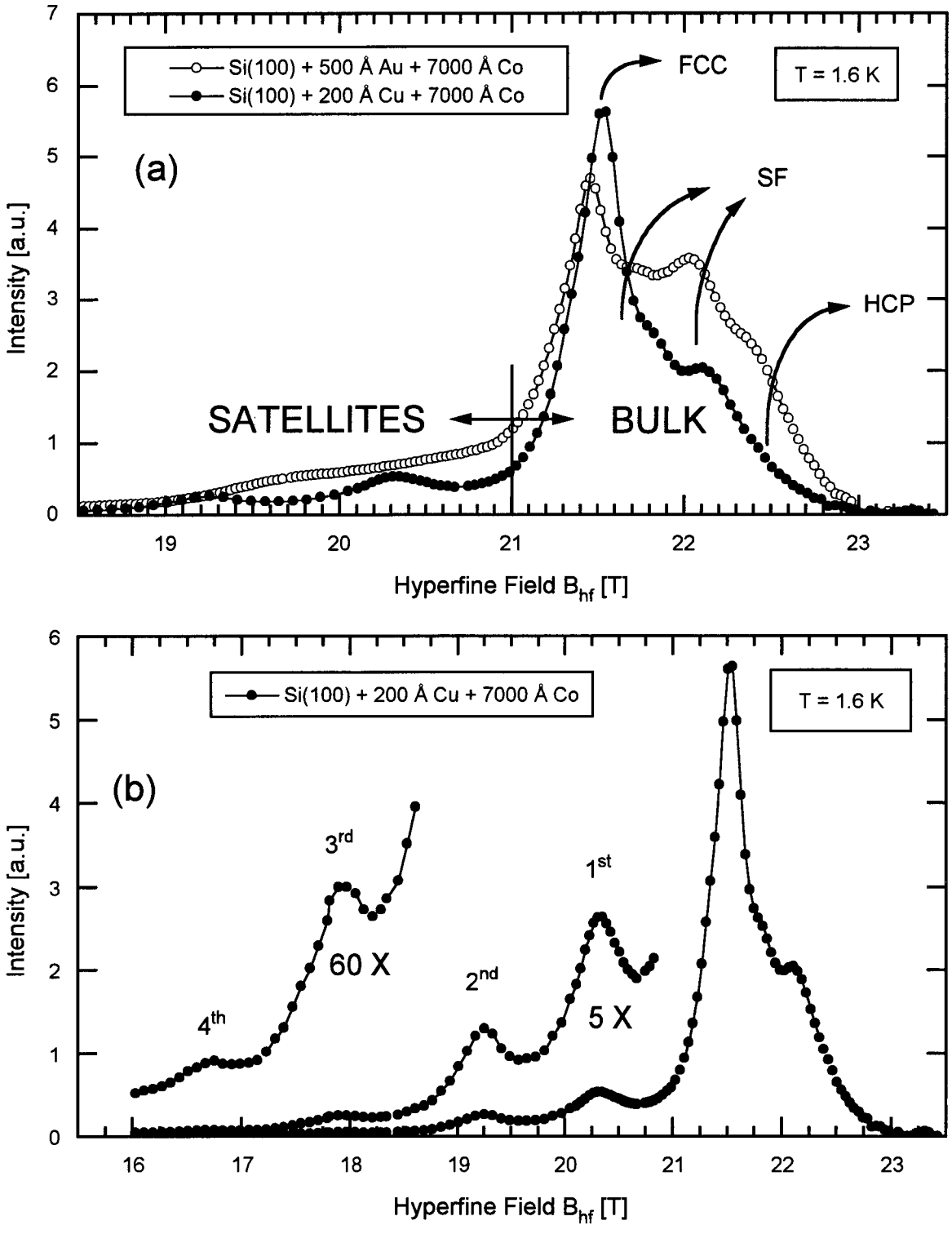


Figure 5.1: *In (a) the NMR spectra of thick Co films are shown. The spectra are corrected for enhancement and normalized between 16 and 23.5 T on their Co layer thickness (7000 Å). Only the base layers are different: 200 Å Cu or 500 Å Au. In (b) only the NMR spectrum of the sample having the Cu base layer is plotted showing the first 4 satellite lines. The satellite intensities are enlarged and the hyperfine field is shown in a wider range.*

| base layer | line | Hyperfine Field $B_{hf}$ [T] | $\Delta B_{hf}$ [T] | FWHM [T] | $\frac{I_a}{I_b}$ [%] |
|---|---|---|---|---|---|
| 200 Å Cu | hcp | – | | | |
| | sf | 22.11 ± 0.04 | | | |
| | fcc | 21.53 ± 0.04 | | 0.4 | 20.7 |
| | | | 1.20 | | |
| | $1^{st}$ sat. | 20.33 ± 0.04 | | | |
| | | | 1.08 | | |
| | $2^{nd}$ sat. | 19.25 ± 0.08 | | | |
| | | | 1.32 | | |
| | $3^{rd}$ sat. | 17.93 ± 0.08 | | | |
| | | | 1.18 | | |
| | $4^{th}$ sat. | 16.75 ± 0.08 | | | |
| 500 Å Au | hcp | 22.40 ± 0.06 | | | |
| | sf | 22.03 ± 0.03<br>21.73 ± 0.03 | | | |
| | fcc | 21.45 ± 0.03 | | 0.5 | 27.5 |

Table 5.1: *The samples mentioned both have the same Si(100) substrate layer and a 7000 Å Co layer. In between these layers a base layer is situated. In the table above, this base layer, peak positions ($B_{hf}$), hyperfine field differences of successive satellite lines ($\Delta B_{hf}$) of main and satellite lines, full widths at half maximum (FWHM), and the intensity ratio alloy (satellites) to bulk $\frac{I_a}{I_b}$ are shown. All data are taken from figure 5.1.*

neighbour shell. If this shell of 12 nearest neighbours inhabits n Cu atoms (and thus 12−n Co atoms), a resonance line due to this surrounding of a Co atom is called the $n^{th}$ satellite.

In the case of the 200 Å Cu base layer the first 4 satellite lines (their positions are given in table 5.1) are clearly visible, which is shown in figure 5.1 (b), in contrast to the Co film possessing the 500 Å Au base layer, which shows only a constant decreasing intensity (but no separate satellite lines are distinguisable), going from 21 T to 19.5 T and a sharp decrease at approximately 19.5 T. For hyperfine field values lower than 19.5 T the intensity has the same constant decrease in intensity, which is already negligibly small compared to the intensity of the fcc main line at 21.5 T. This (and also the difference in FWHM of the peaks of the two films) might be explained by the smaller lattice mismatch of Co with the fcc Cu base layer ($\eta = -2\%$) compared to the mismatch of Co with the fcc Au base layer ($\eta = -14\%$). See also table 5.1.

From this table and figure 5.1 one might conclude that the Cu base layer causes a better crystallographic structure in the Co layer. First a better one phase structure, i.e. more fcc compared to hcp, is obtained; secondly the FWHM of resonance peaks becomes smaller. The fact that satellite lines can be seen separately in NMR spectra of Co films grown on Cu base layers is mainly due to presence of a better one phase structure, i.e. a relatively larger fcc participation. The fact that the FWHM of resonance peaks are smaller (than in case of an Au base layer) is circumstantial. The average hyperfine field distance between the successive satellites is 1.2±0.1 T. The intensity ratio $\frac{I_a}{I_b}$ of the bulk between 21.0 and 23.5 T and the alloy between 15.0 and 21.0 T are both about 1 : 4. Assuming that the Cu impurities had spread themselves homogeneously over the Co layer, we might determine the percentage Cu in the Co layer by using the *binomial distribution.* The intensities of those lines (both satellite lines and bulk lines) have a mutual ratio which is dependent upon the concentration Cu in Co. With this knowledge one can compare the ratio of the total intensities to the theoretical (binomial) results by separating the NMR spectrum in an alloy part below 21 T and a bulk part above 21 T, i.e. integrating the measured NMR spectrum below and above 21 T respectively: 1.6±0.1 % (at.) Cu in the Co layer in case of the Cu base layer and 2.0±0.1 % (at.) Cu in the Co layer in case of the Au base layer. This difference in atomic Cu percentage might be caused by the electrolyte which had in both cases not an identical (Co and/or Cu) ion solution. However, X-ray Fluorescence (XRF) showed that about 4% Cu should be expected between the Co atoms [LSGdJ95]. Furthermore, the intensity ratios of the mutual satellite lines are not in accordance with the expected values obtained in case of binomial distribution, i.e. the Co-Cu alloy structure deviates from the binomial distribution towards segregation (the probability for a Co atom to be surrounded by 12 Co atoms stays quite high) which is in agreement with the well known low miscibility of Co and Cu as had been refered to by Meny et al. [MJP93b].

### 5.2.2 The thickness of the Co film

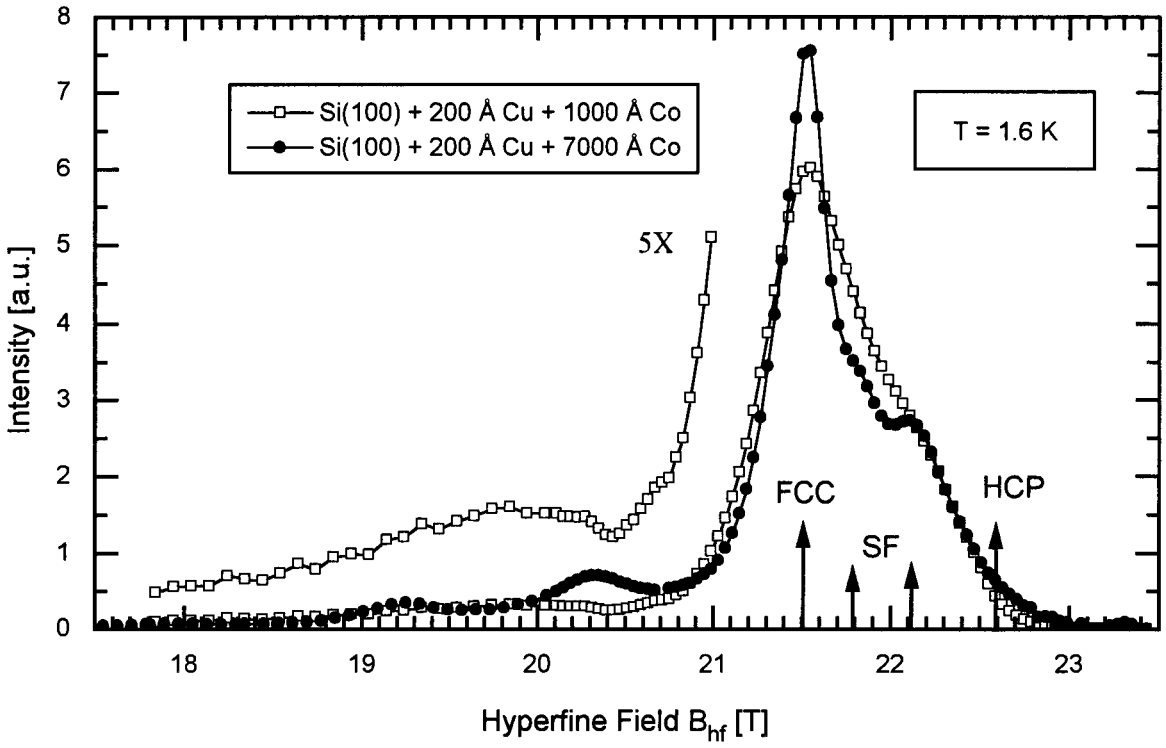


Figure 5.2: *NMR spectra of thick Co films grown in a Co-Cu bath. The samples consist of a Si(100) substrate, a 200 Å Cu base layer, and are grown in a Co-Cu bath. The spectra are normalized between 14.8 and 23.4 T on 1000 Å and 7000 Å Co. The NMR spectrum of the 7000 Å Co layer is the same as shown in figure 5.1.*

A smaller Co layer (1000 Å) is chosen to examine in addition to the 7000 Å Co layer, because the prefered structure (fcc) in relation to the presence of hcp and stack faults should be more prevailing in thinner layers [BH94]. In figure 5.2 the NMR spectra of two samples, which differ only in Co layer thickness, are shown. The samples both consist of a Si(100) substrate, a base layer of 200 Å Cu, and have an approximately 1000 Å respectively 7000 Å thick Co layer on top of the base layer. The samples are grown in an electrolyte containing both $Co^{2+}$ and $Cu^{2+}$ ions. Again due to the use of Cu as a base layer in both NMR spectra, the hcp structure is negligible compared to the presence of fcc. The fcc peak position of the 1000 Å Co layer is almost the same as in the case of the 7000 Å Co layer: 21.55±0.04 T. However, the peak width of the fcc main line of the 1000 Å Co layer is estimated to be at least 0.6 T, and thus astonishingly broader than the 7000 Å Co layer peak. This broadening also causes the resonance line due to stacking faults (at 22.11 T in case of the 7000 Å Co) to be only distinguishable as an asymmetry in the main fcc line and satellite lines to be undetectable. In the case of the 1000 Å Co layer only a wide peak at 19.8±0.1 T is recognizable. Its FWHM is at least 2 T while in case of the 7000 Å Co the line widths of the first and second satellite are each roughly 1 T.

### 5.2.3 The composition of the electrolyte

In the now following part, we show NMR spectra of 7000 Å Co films, which vary in base layer (200 Å Cu or 500 Å Au) and in electrolyte composition (possessing a certain concentration of $Co^{2+}$ with $Cu^{2+}$ or without $Cu^{2+}$ ions). Figure 5.3 shows the influence of the presence of $Cu^{2+}$ ions (amongst $Co^{2+}$ in the electrolyte) on NMR spectra of the Au base layer (a) and the Cu base layer (b).

| base layer | line | Hyperfine Field $B_{hf}$ [T] | FWHM [T] |
|---|---|---|---|
| 200 Å Cu | hcp | 22.47 ± 0.08 | |
| | sf | 22.15 ± 0.04<br>21.83 ± 0.04 | |
| | fcc | 21.55 ± 0.04 | 0.3 |
| 500 Å Au | hcp | 22.39 ± 0.04 | |
| | sf | 22.07 ± 0.04<br>21.75 ± 0.04 | |
| | fcc | 21.47 ± 0.04 | 0.4 |

Table 5.2: *The samples both consist of: Si(100) + base layer + 7000 Å Co and are grown in a Co bath. In the table above, this base layer, peak positions ($B_{hf}$), and full widths at half maximum (FWHM) are shown. All data are taken from figure 5.3.*

The NMR Co films grown in a Co-Cu bath, are the same as shown in figure 5.1 (a). All four spectra shown are normalized on the same Co layer thickness: 7000 Å. The samples grown in a Co bath clearly distinguish them selves from those grown in a Co-Cu solution by showing an almost neglible spin-echo at hyperfine fields lower than 21 T, and thus having no satellite intensities due to absence of $Cu^{2+}$ in the electrolyte. Both Co bath and Co-Cu bath grown samples show a uniform shift at the bulk part of the NMR spectrum if one compares the Au base layer to the Cu base layer in each case. The shift due to the Au base layers is 0.08 T lower than the hyperfine field shift due to the Cu base layers. This difference might be explained by the larger lattice mismatch of Co on Au (-14%)

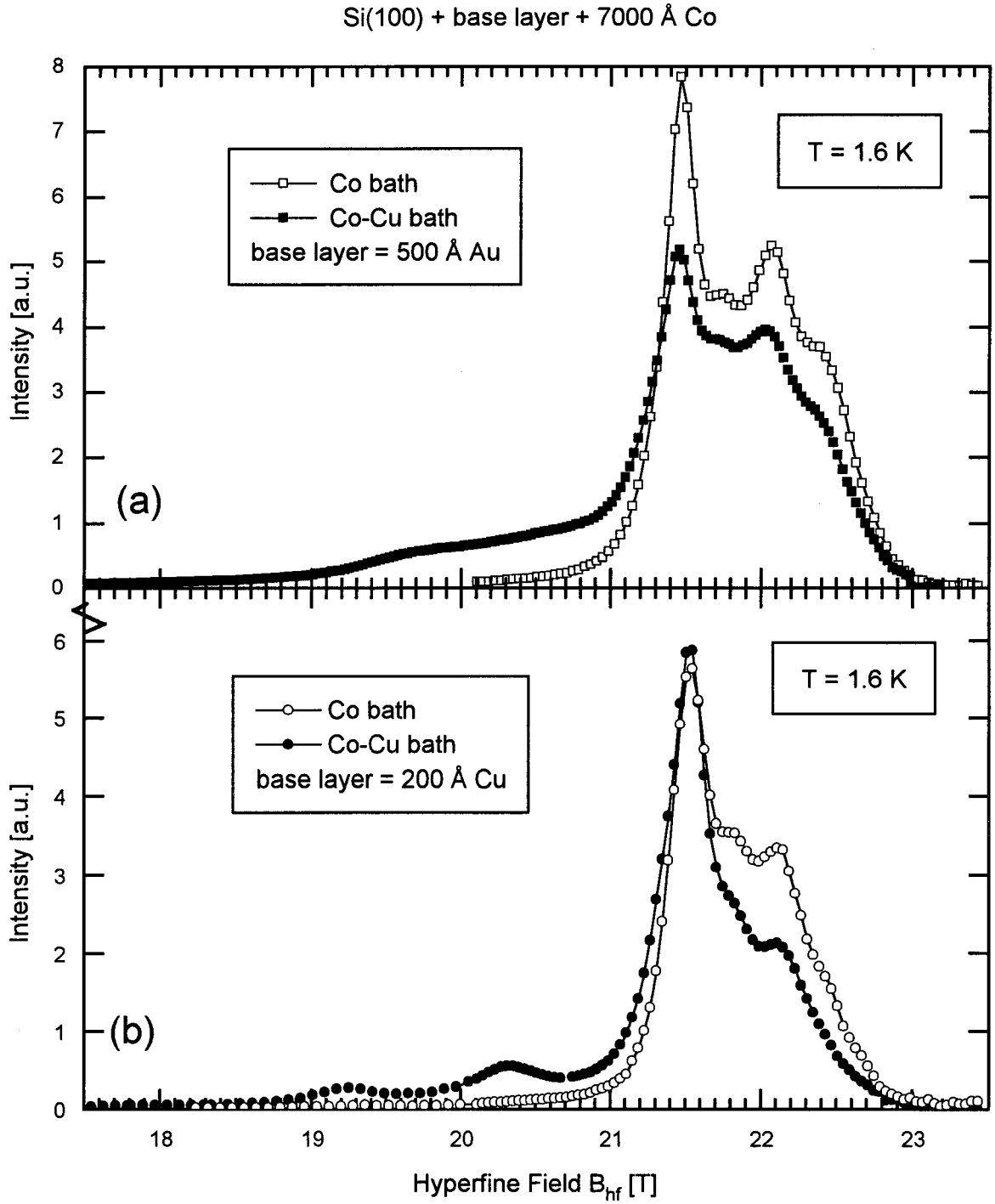


Figure 5.3: *In (a) the NMR spectra of two Co films are shown having an Au base layer and in (b) having a Cu base layer but in both (a) and (b) the two films vary in electrolyte composition, i.e. with and without $Cu^{2+}$ ions. The spectra are normalized between 17.5 and 23.5 T on their Co layer thickness (7000 Å). The NMR spectra of the samples grown in a Co-Cu bath (i.e. $Cu^{2+}$ presence in the electrolyte) are already shown and discussed in sections 5.2.1 and 5.2.2.*

compared with Co on Cu (-2%). However, the amount of $Cu^{2+}$ (about 4 at. %) is not of any noticeable influence on the strain.

In case of the Co bath grown samples, both the Au base layer and the Cu base layer cause the Co layer to posses two phases: mainly fcc Co (about 21.5 T) and a small part hcp Co (about 22.6 T). The Cu base layer invokes the best results in obtaining a dominating fcc structure. Besides these phases, stacking faults are also present (around 22.1 T). This behaviour is identical to the Co-Cu bath grown samples in section 5.2.1.

### 5.2.4 Earlier NMR results on Co-Cu alloys

In the now following part, we will compare our Co film NMR measurements with some earlier NMR results on Co-Cu alloys. We only use the 7000 Å Co film, which is grown on a Cu base layer and mentioned in table 5.1, for comparison. The NMR spectrum of this Co film (using field scans at 1.6 K) contained the most information (in regard to the satellite structure) due to the Co-Cu bath (4 at. % Cu) and due to the base layer (causing a mainly fcc presence and narrow lines).

| publication | Hyperfine Field $B_{hf}$ [T] | | | | | $\Delta$(sat) [T] |
|---|---|---|---|---|---|---|
| | main | satellites | | | | |
| | fcc | $1^{st}$ | $2^{nd}$ | $3^{rd}$ | $4^{th}$ | |
| own measurements | 21.53 | 20.33 | 19.25 | 17.93 | 16.75 | 1.20±0.09 |
| [MJP93b, MPL92] | 21.5 | 19.9 | 18.2 | – | – | 1.6 ±0.1 |
| [DV90] | 21.62 | 19.8 | 17.9 | 16.2 | – | 1.8 ±0.1 |
| [NYNM74] | 21.57 | 19.8 | 17.9 | – | – | 1.8 ±0.1 |
| [KAI66] | 21.4 | 20.1 | – | – | – | 1.3 |

Table 5.3: *Our own hyperfine field values for fcc main line and satellites of a (Cu polluted) Co film compared to those of Co-Cu alloys found by Kobayashi et al.* [KAI66], *Nasu et al.* [NYNM74], *Le Dang et al.* [DV90], *and Meny et al.* [MJP93b, MPL92]. *$\Delta$(sat) stands for the* **average** *distance of the successive resonance lines.*

The reference data were taken from Kobayashi et al. [KAI66], Nasu et al. [NYNM74], Meny et al. [MJP93b, MPL92], and Le Dang et al. [DV90]. All above-refered NMR

measurements were frequency scans at zero (external) field. The first two were measured at 77 K ($LN_2$), while the NMR spectra of the last two were obtained at 4.2 K (LHe). The atomic percentages of Cu were also different in each case: Kobayashi et al.: 3%; Nasu et al.: 0.93%, 2.8%, 4.7%, and 7.5%; Meny et al.: 2%, 6%, and 10%; and Le Dang et al.: 3%.

Kobayashi et al. had prepared their samples by melting, and after homogenizing and filling, by annealing or quenching. Nasu et al. used samples made by induction melting electrolytic cobalt and oxygen-free copper. After being homogenized for 3 days at 1000°C in a high vacuum environment, those alloys were filed into fine powders which were mixed with fine aluminia powders to avoid sintering during the anneal treatment for 1 day at 800°C and finally quenched into water (to obtain fcc phase). An anneal treatment is avoided by Meny et al. [MJP93b], because it would *demix* Co-Cu alloys. They prepared the samples by quenching from the melt, then ground and heat treated appropriately to stabilize a solid solution and, as far as possible, a single phase. Finally, Le Dang et al. reported of a diluted Co-Cu alloy having a NMR spectrum consistent with a *random* distribution.

As one can see in table 5.3, only Kobayashi et al. have found an almost corresponding value for the average distance $\Delta$(sat) between *successive* satellite resonance lines: 1.3 T in accordance to 1.20±0.09 T found for the present electrodeposited alloy. But it should be remarked that Kobayashi et al. only detected the $1^{st}$ satellite, while the other 3 references, although finding a higher value of about 1.6 and 1.8 T for $\Delta$(sat), show at least (the first) 2 satellites. The hyperfine field values of their satellite lines show each separately a value between successive lines, almost identical to their average $\Delta$(sat). The fcc hyperfine field values vary among all references and our measurements which is mainly due to the different atomic percentages copper in the Co-Cu alloys (and thus different strain) and the preparation and/or growing methods (causing alloy structures which vary from being a random distribution to clusterlike Cu demixtures surrounded by bulk Co).

## 5.3 Co/Cu multilayers

In this section, the NMR spectra of three series of Co/Cu multilayers are shown. Earlier NMR measurements of similar[1] Co/Cu multilayers will precede our own NMR results in each subsection. The first two series are (x Co + 40 Å Cu) multilayers, which differ in base layer (500 Å Au or 200 Å Cu) and have a different growth texture ([111] or [100] respectively). Due to the varying Co layer thickness, several structural properties (like interface roughness, topology, and strain) can be determined. Varying the Cu layer thickness in the (15 Å Co + y Cu) series, determinating the FWHM and the positions of the main (fcc) line of each sample in the series should tell us, amongst other things, more about strain, interface roughness, and conditions to obtain one phase. Magnetic and electrical characterizations of some samples are already reported [LSGdJ95]. Some structural characterizations (XRD measurements) are also given in the just-mentioned

[1]Though NMR spectra of **electrodeposited** Co/Cu multilayers have never been published, our electrodeposited Co/Cu multilayer results are compared with sputtered, MBE grown, etc. Co/Cu multilayers dealt with in the review subsection.

report. All spectra are normalized on the Co layer thickness of the samples. This implies that, wherever the interface structure is the same amongst all samples within a series, the spectra should overlap, while the contributions from the bulk increase proportionally to the Co layer thickness $t_{Co}$. In this 'model' we neglect the alloy contribution to the satellite lines (mainly $1^{st}$ satellite, because the portion of higher satellites in the NMR spectra are undetectable due to the low percentage of Cu impurities in the bulk Co), which is also proportionally to $t_{Co}$. Whether or not this neglection is justifiable will be discussed in the following sections.

### 5.3.1 (x Co + 40 Å Cu) [111]

#### NMR literature review

In table 5.4 some earlier reported NMR and experimental characteristics are tabulated. Further details (mainly about the characteristics of the sample) will follow hereafter.

Renard et al. [RBD+92] examined UHV evaporated multilayers: $glass$+250 Å $Au(111)$+ $m \times (x$ Å $Co + y$ Å $Cu)$. The total thickness for the multilayer part $m \times (x + y)$ is about 500 Å, with $(x, y) \in \{(6,6); (6,10); (10,6); (10,10); (20,20)\}$. The base layer was annealed at 150°C during 30 minutes and a deposition rate of 1 Å/s for both Co and Cu was used.

Le Dang et al. [DV90] used MBE grown multilayers: $GaAs(110) + m \times (t_{Co} + t_{Cu})$ with $t_{Cu} = (23 \pm 3)$ Å, $t_{Co} \in \{20, 30, 40, 65$ Å$\}$, and a total superlattice thickness of 1500 Å. The substrate was annealed.

Nakamura et al. [NSS+93] prepared the sample by successively depositing permalloy ($Ni_{80}Fe_{20}$), Cu, Co, and Cu in ultrahigh vacuum (UHV) on a 50 Å $Cr$ buffer (i.e. base) layer deposited on a *Mylar* substrate at room temperature. The nominal structure of the multilayer, used in the zero-field broad-band experiment, is $20 \times [15$ Å $NiFe + 35$ Å $Cu +$ 15 Å $Co + 35$ Å $Cu]$.

Y. Suzuki et al. [SMY+87] examined Co/Cu superlattices grown on 300 $\mu$m $Si(111)$ single crystal substrates with 1500 Å $Ag(111)$ buffer layers at 50°C by UHV electron beam evaporation, using a growth rate of 0.4 Å/s. The zero-field spin-echo spectra were taken from 33 Å/33 Å and 8 Å/8 Å $Co/Cu$ multilayers, which were taken out of a series of Co/Cu superlattices with layer thicknesses varying from 8 to 33 Å for both Co and Cu separately. The repetition rate was adapted in order to obtain always a 2000 Å thick multilayer.

Schreiber et al. [SdGG+94] measured two $10 \times (x$ Å $Co + y$ Å $Cu)$ multilayers: $(x, y) = (47, 26); (31, 20)$. No further sample characteristics were specified. In both cases the NMR spectra were recorded by scanning the external field at a fixed frequency showing peaks due to stacking faults (sf) and hcp (the relative amount of these properties is increased for thicker Co layers), fcc (which still dominates and for both above-mentioned multilayers found at 21.3 and 21.2 T, respectively), and the $3^{rd}$ satellite. This distinct satellite line indicated the presence of a flat interface and was found at 16.6 T (!) in contrast with 17.3 T which is the claimed position of the $3^{rd}$ satellite in case of allmost all frequency scans at zero-field.

Clarke et al. [CBT+94] used samples grown by MBE on *Ge - buffered* (110) *GaAs*

| publication | Characteristics | | | |
|---|---|---|---|---|
| | NMR | | experimental | |
| | $\Delta$(sat) [T] | resonance lines | scan (f/B) | growth method |
| [RBD+92] | 1.4 | main fcc; $3^{rd}$ sat. | f | UHV evaporation |
| [DV90] | 1.5 | sf; main fcc; $3^{rd}$ sat. | f | MBE |
| [NSS+93] | 1.5±0.4 | main fcc; $1^{st}$, $2^{nd}$, $3^{rd}$ sat. | f | UHV deposition |
| [SMY+87] | 1.4 | main fcc; $3^{rd}$ sat. | f | UHV electron beam evaporation |
| [SdGG+94] | 1.6 | sf; main fcc; $3^{rd}$ sat. | B | – |
| [CBT+94] | 1.5 | main fcc; bcc; $3^{rd}$ sat. | f | MBE |
| [TRG94] [LKRW93] | 1.5±0.1 | main fcc; $1^{st}$ sat.(?); $3^{rd}$ sat. | f | MBE |
| [PM93] | 1.7±0.1 | hcp; sf; main fcc; $1^{st}$, $2^{nd}$, $3^{rd}$ sat. | f | various: see paper |

Table 5.4: *Earlier NMR results on Co/Cu [111] multilayers. The first column shows the references, the second the (average) distance of successive satellites, the third column shows the sort of peaks (fcc, stacking faults: sf, hcp, and sitellites) one is able to see in the NMR spectra dealt with in the citations, the fourth column determines whether it had been a frequency (f) scan or a field (B) scan, and finally the growth method is reported in the fifth column. The NMR measurements were performed at either 2 K or 4.2 K. Details about the characteristics of the samples is to be found in the papers.*

substrates. The buffer layers consisted of 15 Å (110) *bcc Co*, followed by 20 Å (111) *Au*. The Co/Cu superlattices were [111] oriented and the Co/Cu layers were grown alternatingly which was repeated 30 times. In growing the multilayer a Co deposition rate between 0.15 and 0.25 Å/s, and a Cu deposition rate of 0.33 Å/s were used (causing a deviation of 1 Å in the determination of the thickness of the Co - and also the Cu - layer). In examining the spectrum of a (15 Å $Co$ + 6 Å $Cu$) superlattice, only two characteristic NMR peaks were observed (main fcc line and $3^{rd}$ satellite line), while a third at 19.8 T was *assumed* to be present due to the 15 Å bcc Co buffer layer!

Thomson et al. [TRG94, TKL+94] examined two 20 × (15 Å $Co$ + 7 Å $Cu$) multilayers deposited by MBE onto a $GaAs$ substrate varying only in a part of the three layered buffer: 500 Å $Ge$ + 15 Å $Co$ + (10 Å $Au$ or 200 Å $Cu$) and a 20 × (15 Å $Co$ + 9 Å $Cu$) multilayer deposited onto a *Sapphire* substrate containing a 30 Å $Nb$ + 20 Å $Cu$ base layer. The films were capped with Au to inhibit oxidation. Lord et al. [LKRW93] studied similar MBE grown films under UHV conditions. As substrate $GaAs(110)$ was used and the buffer layer consisted of 500 Å $Ge$ + 15 Å *bcc Co* (110) and either 10 Å $Au$ or 200 Å $Cu$. The supperlattices were 20 × (15 Å $Co$ + k Å $Cu$) and again capped with a thin layer of gold. The value of k was 7 or 18.

The publication of Panissod and Mény [PM93] is an overview or a compilation of several other studies like [VGJ+93, MPL92, MPH+93, MJP+93a, dGKdJ+91]. Due to the diversity of the samples (all kinds of substrates, base layers, and multilayer combinations), growing methods (like UHV evaporation, dc magnetron sputtering, and rf diode sputtering), and growing conditions the cited publications are refered to for more information.

### Results

In figure 5.4 NMR spectra of Co/Cu [111] multilayers, which vary only in Co layer thickness, are shown. The spectra are in general characterized by three peaks: the fcc main line (at about 21.3 T) and two (19.4 and 16.7 T: probably the first respectively the third) satellite lines. For more detailed data, see table 5.5. The FWHM of the main line does surprisingly not change with varying Co layer thickness $t_{Co}$ and has an average of 1.25±0.04 T, for one would expect its spin-echo intensity to be dependent on $t_{Co}$ and the ratio $t_{Co}/t_{Cu}$ due to *2 influences*. On the one hand the nnn-line, which is supposed to be present between the first satellite and the fcc main line for a small $t_{Co}$. On the other hand the increase in relative presence of sf and hcp with increasing $t_{Co}/t_{Cu}$. The average distance of successive satellites is found to be (determinating the average distance between main line and third satellite line and dividing by three): 1.54±0.03 T. The average distance between main line and first satellite (1.94±0.14 T) differs remarkably from the former value.

Furthermore, due to the large difference in interface topology (see the different values found for the intensity ratio $\frac{I_1}{I_3}$ in table 5.5) amongst the samples, shown in figure 5.4, it will not be possible to determinate a reliable value for the interface roughness by the method described in section 2.4. A plausible cause for this difference is the presence of the alloy structure in the bulk, causing (parts of) the interface to be proportional to the Co layer thickness $t_{Co}$. To get an estimate of the interface roughness we assumed the division

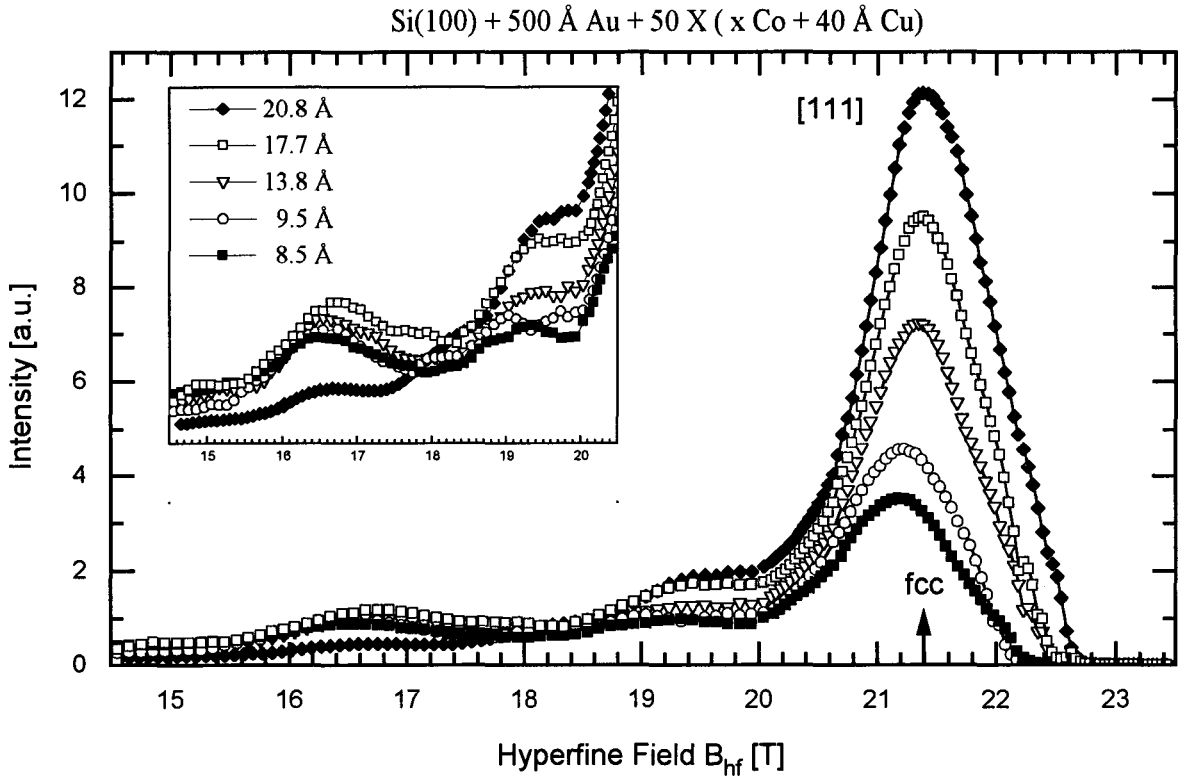


Figure 5.4: *The samples have a Si(100) substrate and a 500 Å Au base layer causing a [111] texture. The spectra belonging to the samples of the (x Co + 40 Å Cu) [111] series are corrected for enhancement and normalized between 14.5 and 23.5 T on their Co layer thicknesses (x).*

of interface and bulk part in the NMR spectrum to be between 20.0 and 20.5 T. Due to normalization of the total spectrum on $t_{Co}$, one is able to determine the interface roughness by integrating the interface part of the spectrum. At 20.0 T the interface roughness (i.e. the total amount of Co in the interfaces on *both* sides together) varies from 3.9 Å for a Co thickness $t_{Co}$ = 8.5 Å to 5.5 Å for $t_{Co}$ = 17.7 Å, while at 20.5 T it differs from 4.5 Å for a Co thickness $t_{Co}$ = 8.5 Å to 6.6 Å for $t_{Co}$ = 17.7 Å. Thus, the interface roughness of both interfaces together is varying from 4.2±0.3 Å for $t_{Co}$ = 8.5 Å to 6.0±0.5 Å for $t_{Co}$ = 17.7 Å.

The measured NMR spectra of the (x Co + 40 Å Cu) [111] series can roughly be divided into three parts: (i) the main line due to bulk fcc Co at about 21.4 T; (ii) the tail below 20 T, mainly due to the Co at the interface; and (iii) the shoulder of the main line at lower hyperfine field between 20 and 21 T. The peak width of the main line does not change as function of Co layer thickness, the hcp structure is absent, and the contribution of stacking faults is negligible, so the quality of the bulk structure in the multilayers is unchanged. The peak position changes as function of $t_{Co}$: 21.21±0.04 T in case of 8.5 and 9.8 Å and 21.36±0.03 T in case of 13.8, 17.7, and 20.8 Å, which is probably not due to strain, but due to the presence nnn-line though this line has only been observed in the Co/Cu [100]

| x [Å] | main line | | satellites | | |
|---|---|---|---|---|---|
| | fcc [T] | FWHM [T] | $1^{st}$ [T] | $3^{rd}$ [T] | $\frac{I_1}{I_3}$[%] |
| 8.5 | 21.18±0.05 | 1.30 | 19.33±0.09 | 16.6±0.2 | 112 |
| 9.8 | 21.23±0.05 | 1.26 | 19.0 ±0.2 | 16.7±0.2 | 113 |
| 13.8 | 21.35±0.04 | 1.22 | 19.4 ±0.2 | 16.6±0.1 | 121 |
| 17.7 | 21.34±0.04 | 1.21 | 19.44±0.09 | 16.8±0.1 | 146 |
| 20.8 | 21.39±0.04 | 1.25 | 19.54±0.09 | 16.7±0.2 | 415 |

Table 5.5: *The samples consist of: Si(100) + 500 Å Au ([111] texture) + 50 × (x Co + 40 Å Cu). Shown are the position and full width half maximum (FWHM) of the fcc main line, the position of the first and third satellite line, and the ratio of their heights* ($\frac{I_1}{I_3}$).

multilayers as reported in subsection 5.3.2. The interface part of the spectra show two satellite lines: a probably $3^{rd}$ satellite at 16.7 T and a presumably $1^{st}$ satellite at 19.4 T which are both about 0.6 T lower than the values found for frequency scans in zero-field in above-cited articles, but the value for the $3^{rd}$ satellite is very much in agreement with the field scan NMR results ($3^{rd}$ satellite: 16.6 T and fcc main line: 21.2 and 21.3 T) of Schreiber et al. [SdGG+94].

For the spin-echo intensities between roughly 19 and 21 T, seven possibilities can be brought up: (1) Co atoms with 1 Cu nearest neighbour (i.e. $1^{st}$ satellite due to the interface) at about 19.6 T [GBDV92, GBH+93], (2) metastable bcc Co at about 19.7 T in Co/Fe multilayers [BGH+92, DJML93] but also in Co films having partially a 15 Å bcc Co buffer layer [CBT+94], (3) the alloy structure of the electrodeposited bulk layer causing an extra contribution in the intensity nearby the first satellite, (4) grain boundaries at about 20.5 T [DVV+93], (5) $1^{st}$ hcp satellite line at 20.8 T [Kaw76], (6) the weak signal near 20 T caused by broadening of the main line due to strain or interfacial defects [LKRW93, TRG94], and (7) a next nearest neighbour (nnn-)line at 21 T (the peaks of which are seen in our measurements for Co/Cu multilayer [100] in subsection 5.3.2).

In discussing now these possibilities, we see that the presence of the first satellite line is evident around 19.4 T (1). The difference in intensity as function of the Co layer thickness

nearby this line is not due to a presence of metastable bcc (2) dependent upon the Co layer thickness, but most likely caused by the alloy structure of the bulk due to electrodeposition of the samples (3).

The shoulder of the main peak (between roughly 20.2 and 21.0 T) is very likely caused by grain boundaries (4) due to the low miscibility of Co and Cu [MJP93b]. These granular parts in the Co bulk might explain the non-randomness of the alloy structure, as was noticed in section 5.2. There is virtually no hcp (5) present in the main line, thus no hcp satellites are to be expected around 20.8 T. The broadening of the main line near 20 T might be caused by strain or interfacial defects (6) and also the presence of a nnn-line (7), which has already been discussed in detail. The presence of $SO_4$ in the multilayer responsible for causing a spin-echo intensity between 19.5 and 21 T is difficult to discuss, due to the lack of information (like the proof of presence by other measurements, the hyperfine field values of the $SO_4$ satellite lines, and so on) of determinating its contribution to the spectrum. One can neither confirm nor deny the presumed influence of these satellites on the spectrum.

### 5.3.2 (x Co + 40 Å Cu) [100]

In this subsection, we will deal with an electrodeposited Co/Cu multilayer series in which only the thickness of the Co layer varies. This series, however, differs from the previous one by having a [100] texture caused by a different base layer: 200 Å Cu (instead of 500 Å Au). We again will begin with showing the few NMR publications of Co/Cu [100] multilayers in a short literature review. This is followed by showing and discussing our NMR results.

#### NMR literature review

In literature only a few articles (see also table 5.6) dealing with *NMR results on Co/Cu multilayers having [100] texture* are published by: **(1)** Giron et al. [GBDV92, GBH+93], **(2)** Y. Suzuki et al. [SKY92], and **(3)** M. Suzuki et al. [STGY93]. Giron et al. analysed a sample prepared by diode-rf sputtering. It had a 30 × (12.6 Å $Co$ + 20.9 Å $Cu$) multilayer structure and was deposited on a 300 Å $Cu$ buffer layer epitaxially grown on a $Si(100)$ substrate. The thicknesses of cobalt and copper are given within 1 Å. The NMR measurements were carried out at 2 K using frequency scans in zero-field and in 2 kOe (0.2 T) parallel either to the [011] easy axis or to the [001] hard axis in the film plane. The hyperfine field was measured between 17.5 and 22.5 T, and only two peaks are seen: at 19.6 T due to Co sites having only one Cu nearest neighbour and between 21.0 and 21.3 T caused by fcc bulk Co. Y. Suzuki et al. studied samples grown by UHV electron beam deposition. The substrate $MgO(100)$ was chozen and its temperature was 50°C during deposition. On the substrate a buffer layer of 2000 Å $Au$ was grown, followed by a seed layer of 200 Å $Cu$. The Co/Cu superlattices were itself 2000 Å thick. Two kind of supperlattices were studied by zero-field NMR frequency scans at liquid helium temperature: 122 × (8 Å $Co$ + 8 Å $Cu$) and 61 × (16 Å $Co$ + 16 Å $Cu$). The fourth satellite is seen at 11.1 and 11.6 T for the 8 Å Co and the 16 Å Co multilayer respectively, while the average distance of successive satellites is found to be 2.5±0.9 T.

| publication | line | hyperfine field $B_{hf}$ [T] | $\Delta B_{hf}$ [T] |
|---|---|---|---|
| [GBDV92] [GBH+93] | main fcc | 21.0 / 21.3 | 1.4 / 1.7 |
| | $1^{st}$ sat. | 19.6 | |
| [SKY92] | main fcc | 20.7 / 21.2 | 1.5 / (2.0) |
| | $1^{st}$ sat. | 19.2 / – | 2.0 / (2.0) |
| | $2^{nd}$ sat. | 17.2 / 17.2 | 2.0 / 2.0 |
| | $3^{rd}$ sat. | 15.2 / 15.2 | 4.1 / 3.6 |
| | $4^{th}$ sat. | 11.1 / 11.6 | |
| [STGY93] | main fcc | 21.2 | 1.6 |
| | $1^{st}$ sat. | 19.6 | 1.3 |
| | $2^{nd}$ sat. | 18.3 | 1.6 |
| | $3^{rd}$ sat. | 16.7 | |

Table 5.6: *Earlier NMR results on Co/Cu [100] multilayers. The first column shows the references, the second the sort of line seen, the third column shows their positions, and in the fourth column the distances between the successively sighted lines are written. The data taken from Y. Suzuki et al.* [SKY92] *are divided as "x/y" per column, meaning: the value in "x" is due to the 8 Å Co sample while the value in "y" is taken from the 16 Å Co NMR spectrum.*

M. Suzuki et al. had the Co/Cu superlattices prepared on *oxidized Si* substrates in a magnetron sputtering system. After deposition of a $Fe$ buffer layer of variable thickness $t_{Fe}$ (between 0 and 150 Å), 200 Å $Cu$ + 16 × (10 Å $Co$ + 20 Å $Cu$) multilayers were grown at room temperature in Ar at deposition rates of 2-3 Å/s. To obtain the NMR spectra, frequency scans at 4.2 K in zero-field were carried out. For $t_{Fe} \geq 35$ Å XRD measurements determined a [100] texture in the multilayers. For $t_{Fe} = 50$ Å a NMR spectrum is shown having an average distance of successive satellites of 1.5±0.2 T.

**Results**

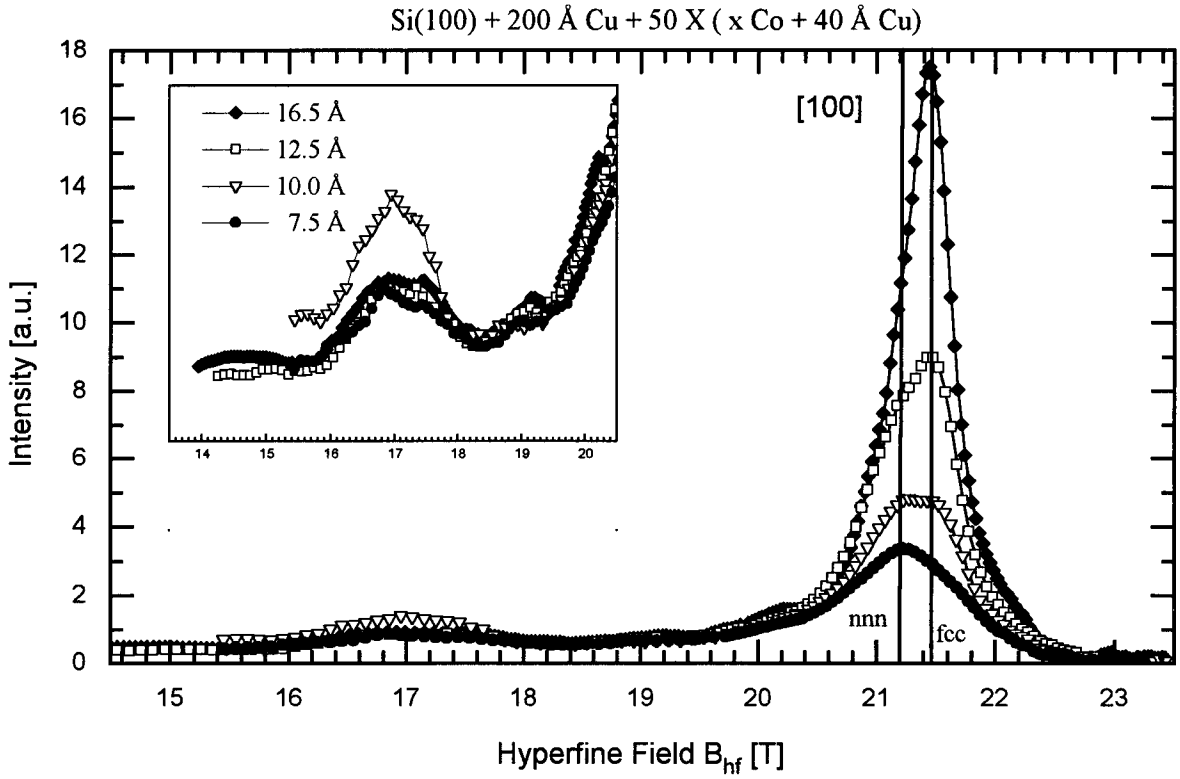


Figure 5.5: *NMR spectra of (x Co + 40 Å Cu) [100] Co/Cu multilayers. The samples have a Si(100) substrate and a 200 Å Cu base layer causing a [100] texture. The spectra are corrected for enhancement and normalized between 15.4 and 23.0 T on their Co layer thicknesses (x). The lines at 21.2 and 21.4 T indicate a presence of next nearest neighbours (nnn-line) beside the bulk Co (fcc main line).*

When we take a look at figure 5.5 we immediately see the striking overlap of the interface part of the NMR spectra (below a hyperfine field of 20.6 T). Around the peak at 17.0±0.1 T of the Co/Cu multilayer with $t_{Co}$ = 10.0 Å merely differs by having a considerably larger intensity. The bulk part (between 20 and 23 T) shows us the presence of two separate lines: a probable nnn-line (at 21.23±0.05 T) and a fcc main line (at 21.45±0.03 T). The peak width (one value for both above-mentioned lines) varies here as function of the Co

layer thickness, in contradiction to the previous [111] series. See also table 5.7.

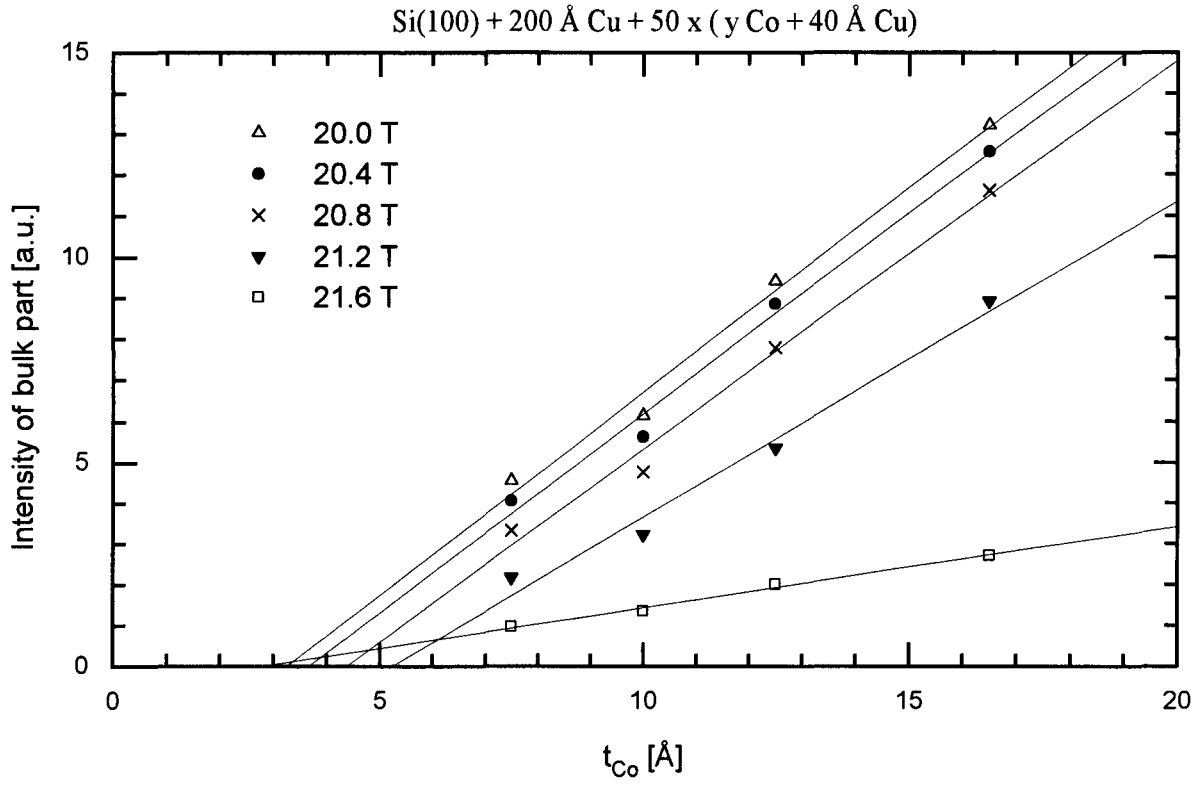


Figure 5.6: *Bulk Co intensity versus Co layer thickness for various values of the boundary between bulk and interface intensity of the NMR spectra of figure 5.5. The determination of the interface roughness is explained by the method shown in section 2.4. From this figure the interface roughness is estimated to be 5±1 Å per two interfaces (top plus bottom).*

Around 19.19±0.04 T some of the spectra show another interface peak, most probably caused by Co nuclei having 2 Cu atoms as nearest neighbours. Only the Co/Cu multilayer having $t_{Co}$ =16.5 Å shows another, extra, interface peak (probably due to Co nuclei having 1 Cu nearest neighbour) at 20.22±0.04 T. Assuming that we have 3 satellite lines seen, i.e. the first, second, and fourth, we find 1.15±0.05 T for Δ(sat)!

Due to the uniform (and almost identical) interface roughness and topology it is possible to determine the interface roughness by the method explained in section 2.4. In figure 5.6 the intersection of the line due to the 21.6 T boundary between bulk and interface occures more than 2 Å lower than the crossing of the 21.2 T boundary line. This can be explained by two facts: (1) offset signals measured in the NMR spectrum influence the crossing by shifting the boundary line upwards and (2) the relative intensity percentage of stacking faults in the bulk as function of the Co layer thickness is not constant which will influence the slope of the fitted line. Therefore, the interfaces (both top and botom interface taken together) in this series were estimated to have an average roughness of 5±1 Å.

| x [Å] | bulk | | satellites |
|---|---|---|---|
| | fcc/nnn [T] | FWHM [T] | $4^{th}$ [T] |
| 7.5 | 21.23±0.06 | 1.24 | 16.85±0.09 |
| 10.0 | 21.28±0.05 | 1.08 | 16.95±0.09 |
| 12.5 | 21.48±0.05 | 0.86 | 17.1 ±0.2 |
| 16.5 | 21.45±0.03 | 0.55 | 17.1 ±0.1 |

Table 5.7: *Positions of the different lines of the NMR spectra of figure 5.5. The samples consist of: Si(100) + 200 Å Cu (causing the [100] texture) + 50 × (x Co + 40 Å Co). Shown are the position and full width half maximum (FWHM) of the combined nnn- and fcc main line, and the position of the presumably fourth satellite line.*

| y [Å] | main line | | satellites | | |
|---|---|---|---|---|---|
| | fcc [T] | FWHM [T] | $2^{nd}$ [T] | $4^{th}$ [T] | $\frac{I_2}{I_4}$[%] |
| 16 | 21.43±0.04 | 1.61 | 19.54±0.09 | 17.3±0.1 | 171 |
| 24 | 21.51±0.04 | 1.05 | – | 17.1±0.2 | 74 |
| 35 | 21.51±0.04 | 1.39 | 19.3 ±0.1 | 17.2±0.3 | 143 |
| 40 | 21.48±0.05 | 0.87 | 19.14±0.09 | 17.1±0.2 | 90 |
| 60 | 21.47±0.04 | 0.76 | 19.24±0.05 | 17.1±0.2 | 117 |

Table 5.8: *Positions of resonance lines in the NMR spectra of figure 5.7. The samples consist of: Si(100) + 200 Å Cu ([100] texture) + 50 × (15 Å Co + y Co). Shown are the position and full width half maximum (FWHM) of the fcc main line, the position of the second and fourth satellite line, and the ratio of their heights ($\frac{I_2}{I_4}$) respectively.*

### 5.3.3 (15 Å Co + y Cu) [100]

We also measured with NMR a Co/Cu [100] multilayer series, which varies only in Cu layer thickness $t_{Cu}$. In measuring the magnetoresistance, it was concluded [LSGdJ95] that pinholes were likely to be present. This was the reason to examine the just-mentioned series by NMR, for an expected change in the spectrum (due to these pinholes) was hoped to be seen. Furthermore, a change of the NMR spectrum was expected due to the change of the initial stacking of Co layers, which is fcc, to a mixed stacking of fcc, hcp, and stacking faults by decreasing the Cu layer thickness. The relative hcp stacking contribution to the bulk part of the NMR spectrum is expected to develop with increasing Co layer thickness or decreasing Cu layer thickness [DVBC91, MPL92].

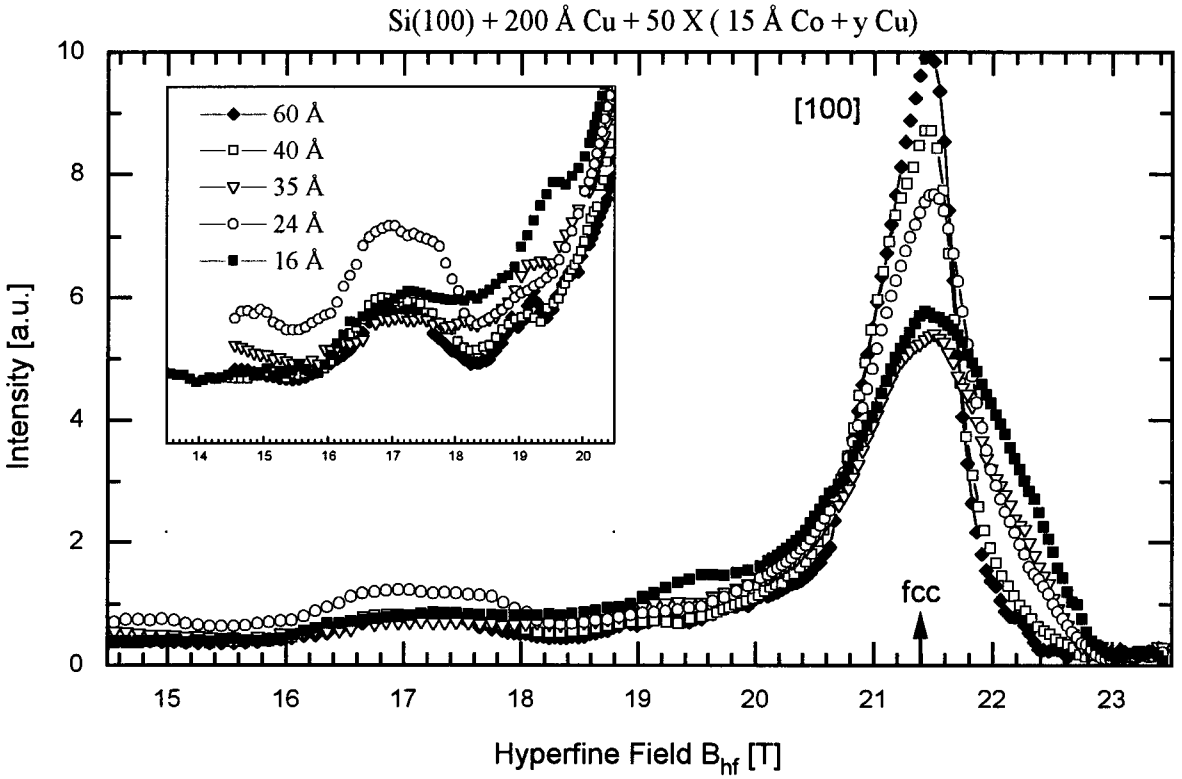


Figure 5.7: *NMR spectra of a Co/Cu [100] multilayer series which varies only in Cu layer thickness. The samples have a Si(100) substrate and a 200 Å Cu base layer causing a [100] texture. The spectra belonging to the samples of the (15 Å Co + y Cu) [100] series are corrected for enhancement and normalized between 14.5 and 23.5 T on their Co layer thickness.*

In figure 5.7 the NMR spectra of the (15 Å Co + y Cu) [100] multilayer series are shown. The Cu layer thickness (y) varies between 16 and 60 Å. The spectra can be divided into two parts: a bulk and an interface which are roughly separated at 20.6 T. The bulk part of the spectrum shows a resonance line at 21.48±0.03 T due to the fcc main line. The full width

at half maximum (FWHM) of these bulk peaks becomes smaller with increasing Cu layer thickness with the exception of $t_{Cu}$ = 35 Å. An asymmetry of the fcc main line is noted for smaller hyperfine field values, probably due to the nnn-line, mentioned in section 5.3.2. The interface part of the NMR spectrum shows two resonance lines: a second satellite at 19.3±0.2 T and a presumably fourth satellite at 17.2±0.1 T. The interfacial spectrum of the 2 samples having the thinnest Cu layer differs by not overlapping with the rest, see $\frac{I_2}{I_4}$ in table 5.8. The sample having a 24 Å Cu layer differs in more aspects: the FWHM is a bit smaller than one would expect, the first satellite has vanished, and the fourth satellite is roughly two times larger compared with other spectra.

## 5.4 Leveling agents

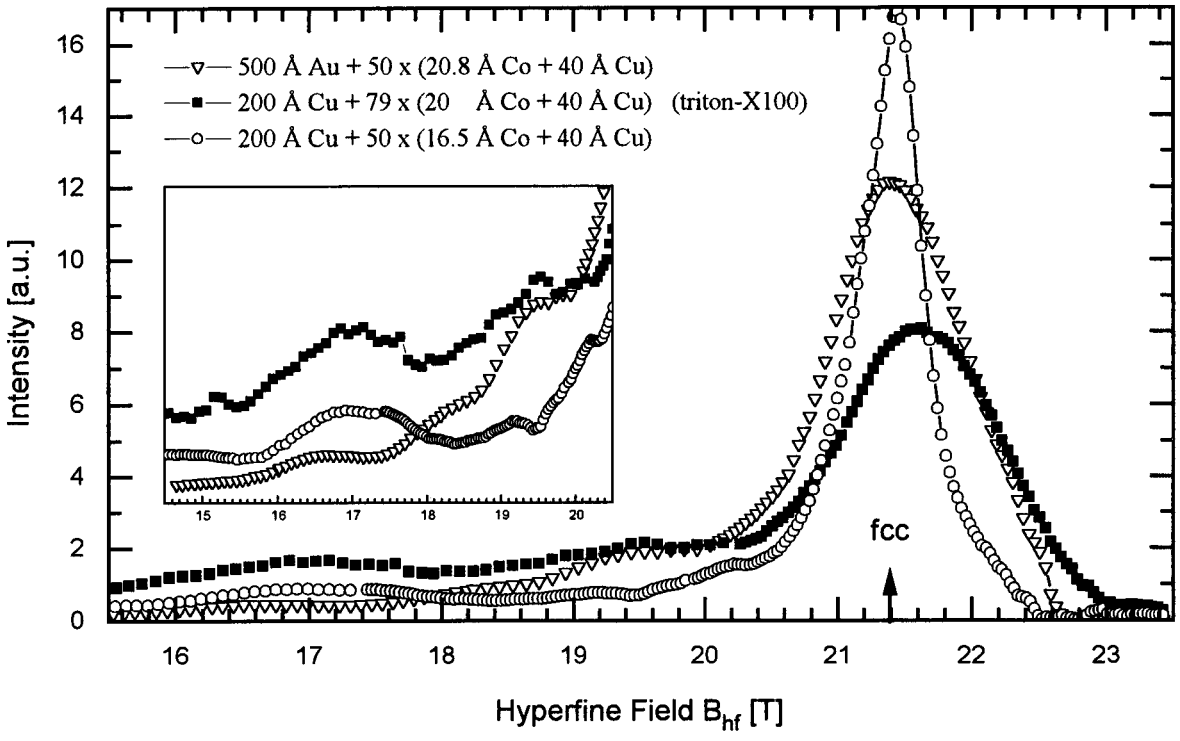


Figure 5.8: *The sample treated with triton-X100 has a Si(100) substrate and a 200 Å Cu base layer. The bilayer consists of a (20 Å Co + 40 Å Cu) layer, which is 79 times repeated. To compare it with similar Co/Cu multilayers, two samples (both not threated with any brightener) having a similar Co thickness and taken from the previous sections are shown: (20.8 Å Co + 40 Å Cu) [111] and (16.5 Å Co + 40 Å Cu) [100]. The spectra are corrected for enhancement and normalized between 14.5 and 23.5 T on their Co layer thickness.*

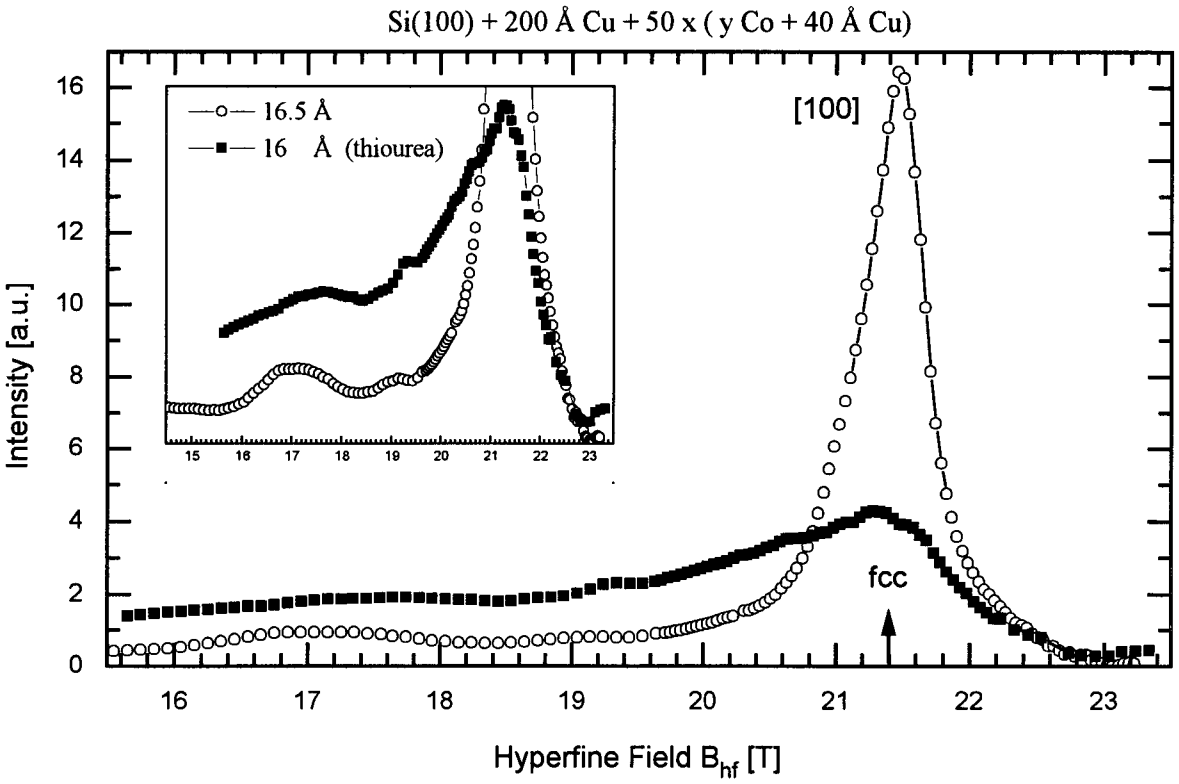


Figure 5.9: *The sample containing thiourea has a Si(100) substrate and a 200 Å Cu base layer. The bilayer consists of a (16 Å Co + 40 Å Cu) layer, which is 50 times repeated. It is compared with a similar Co/Cu multilayer, taken from the [100] series with varying Co layer thickness. The spectra are corrected for enhancement and normalized between 15.5 and 23.5 T on their Co layer thickness.*

In this section the results of NMR measurements on Co/Cu multilayers, which are grown in the presence of an additive, i.e. leveling agent, are presented. The leveling agents are used in order to study the influence of the interface between Co and Cu layer by brightening, i.e. smoothening, it. Two additives are used: thiourea and triton-X100.

In figure 5.8 a NMR spectrum of a (20 Å Co + 40 Å Cu) [100] multilayer, treated with the brightener triton-X100, is shown and compared with NMR spectra of two other Co/Cu multilayers ([100] and [111] textured taken from previous sections). The NMR spectrum of the multilayer treated with triton-X100 is less good defined: the bulk NMR signal shows not only a large FWHM (1.50 T) of the bulk peak (21.63±0.04 T), but also a larger relative contribution of hcp and/or stacking faults even compared to the Co/Cu [111], i.e. having a 500 Å Au base layer[2], multilayer. In spite of the use of a leveling agent,

[2]We compare the triton-X100 treated sample with a Co/Cu multilayer having a different base layer, because this Au base layer caused a worse NMR spectrum, i.e. larger FWHM and more sf and/or hcp in Co films and Co/Cu multilayers, compared to the Cu base layer samples. To emphasize that triton-X100 used as leveling agent causes an even worser spectrum in regard to interface roughness and topology, one

the interface is in regard to topology identical to the (16.5 Å Co + 40 Å Cu) [100] multilayer (the fourth and second satellite are found at 17.2±0.3 T and 19.54±0.09 T respectively). From comparing the integrals of the interface part of the spectrum below about 20.5 T of multilayers grown with triton-X100 and without an additive, one can conclude that a treatment of the multilayer with triton-X100 caused an approximately two times rougher interface!

In figure 5.9 the NMR spectra of two (20 Å Co + 40 Å Cu) [100] multilayers, with and without thiourea as leveling agent, are shown. The thiourea treated sample possesses an even rougher interface than the triton-X100 treated sample shown in the previous section. The NMR spectrum of the multilayer treated with thiourea is the most badly defined: the bulk NMR signal has a huge FWHM (2.8 T) of the bulk peak (21.28±0.04 T), which is identical to the nnn-line hyperfine field value. The relative contribution of hcp and/or stacking faults, though, is not larger than the triton-X100 sample. The interface shows a diluted-alloy patern with peaks at 17.6±0.2 T and 19.6±0.1 T (due to the fourth and the second satellite). This means that the interface of the sample has to be seen structurally as being an alloy of several layers, in which the concentration of (Cu-)impurities per layer increases towards the adjacent Cu layer.

## 5.5 Discussing the results

In this section the most important results are summarized and discussed briefly. In doing this, the section is split in two parts: electrodeposited Co films and Co/Cu multilayers. The Co films are mainly studied to characterize the bulk part of Co/Cu multilayers. The emphasis lays on the multilayers due to their magnetic properties and thus commercial applications.

### Co films and Co-Cu alloys

Of the two (200 Å Cu and 500 Å Au) base layers used, Cu gave us the best NMR results in obtaining information about the 7000 Å Co film, independent of the electrolyte composition (Co bath or Co-Cu bath): the smallest FWHM (0.4 T and 0.3 T in Co-Cu bath respectively Co-bath for the Cu base layer compared to 0.5 T and 0.4 T in Co-Cu bath respectively Co-bath for the Au base layer) measured at the fcc main line, an average distance between successive satellites $\Delta$(sat) = 1.20±0.09 T (in case of the film grown in a Co-Cu bath) showing the first four satellite lines separately, and the best one phase structure, i.e. the relatively fewest presence of hcp and sf. The $\Delta$(sat) value could be used to compare in case of Co/Cu multilayers, though some caution must be taken when using reference results from alloys where impurities are randomly distributed in order to study systems that are topologically different (like multilayers). Besides the number and nature of the nearest neighbours, their position (i.e. the symmetry of the neighbourhood) may also play some role in determining the hyperfine field and thus influencing the distance between the $n^{th}$

phase structure, and FWHM.

and $(n+1)^{th}$ satellite line. Strain was present (a negative shift of 0.08 T occured in samples grown on an Au base layer compared to NMR results of samples grown on a Cu base layer) due to the difference in base layer, independent from the electrolyte composition.

An unexplainable disimprovement of the stabilization of the structure was obtained in measuring the NMR spectrum of a 1000 Å Co film in stead of the normally used 7000 Å Co thickness grown on a Cu base layer. However, the structure of this last-mentioned Co film is comparable with that of MBE grown Co films [dGBvAdJ94, vAdGB+93] and gave even better results compared with the Co-Cu alloys measured by Le Dang et al. and Mény et al., shown and refered in table 5.3. The Co films grown in Co-Cu bath appeared to have satellite lines in the NMR spectra which indicated that they were Co-Cu alloys having no random distribution (at least 2% at. Cu determined from the NMR spectra and 4% at. Cu by XRF [LSGdJ95]). Meny et al. [MJP93b] already found that $Co_{1-x}Cu_x$ alloys (with x = 0.02, 0.06 and 0.10 and compared to other Co-X alloys with X = Ru, Fe, and so on) deviate much more from the binomial law towards segregation (the experimental probability for Co to be surrounded by 12 Co stays quite high) which is in complete agreement with the low miscibility of Cu in Co and with the ratios we measured due to our own NMR results. One can conclude that the NMR spectra of electrodeposited Co/Cu multilayers, which will be talked about shortly, consist of three contributions: (1) a bulk Co contribution causing the main lines, (2) an alloy part contribution to the satellite lines proportional with the Co layer thickness, and we assume (3) an interfacial part, also contributing to the satellite lines but in intensity independent from the Co layer thickness.

## Co/Cu multilayers

The narrow linewidth (especially in case of the (x Co + 40 Å Cu) [100] multilayer series where probable nnn-lines can be distinguished from bulk fcc lines) indicates that a large number of Co atoms are in an undisturbed crystal lattice and proves that a good quality fcc crystal can be grown by electrodeposition on Si(100) substrates containing Cu base layers. The FWHM is used as measurement for determinating the stabilization of the fcc phase, see figure 5.10 a. The Co/Cu [100] multilayer series with varying $t_{Co}$ has a FWHM dependence (smaller with increasing $t_{Co}$) while the FWHM of the Co/Cu [111] multilayer series stays almost unchanged with varying $t_{Co}$. The third series (Co/Cu [100] multilayers with varying $t_{Cu}$) has a FWHM which becomes smaller with increasing $t_{Cu}$. The FWHM behaviour of the [100] series with different $t_{Co}$ demonstrated the presence of the presumably nnn-line, while in case of the [100] series with different $t_{Cu}$ the dependence is caused by partially on one hand an increase of (mainly) sf and hcp with decreasing Cu layer thickness and on the other hand a not exactly constant, i.e. varying about 2 Å, $t_{Co}$ causing an unintended nnn-line influence. The presence of the alloy structure might probably be noticed in a general tendency of the [111] series to have an increase in spin-echo intensity especially between 19 and 21.5 T in their NMR spectra with increasing $t_{Co}/t_{Cu}$, see figure 5.10 b. No similar clear increase in that hyperfine field part is seen in case of [100] series by increasing $t_{Co}/t_{Cu}$. It can not be stated unambiguously that the tendency of increase in satellite intensity for the [100] series with varying $t_{Cu}$ is merely caused by pinholes; the influence

of satellite lines due to hcp and sf might also be a serious possibility. Evidence of strain is not present, especially when one takes the possibility of a nnn-line into account.

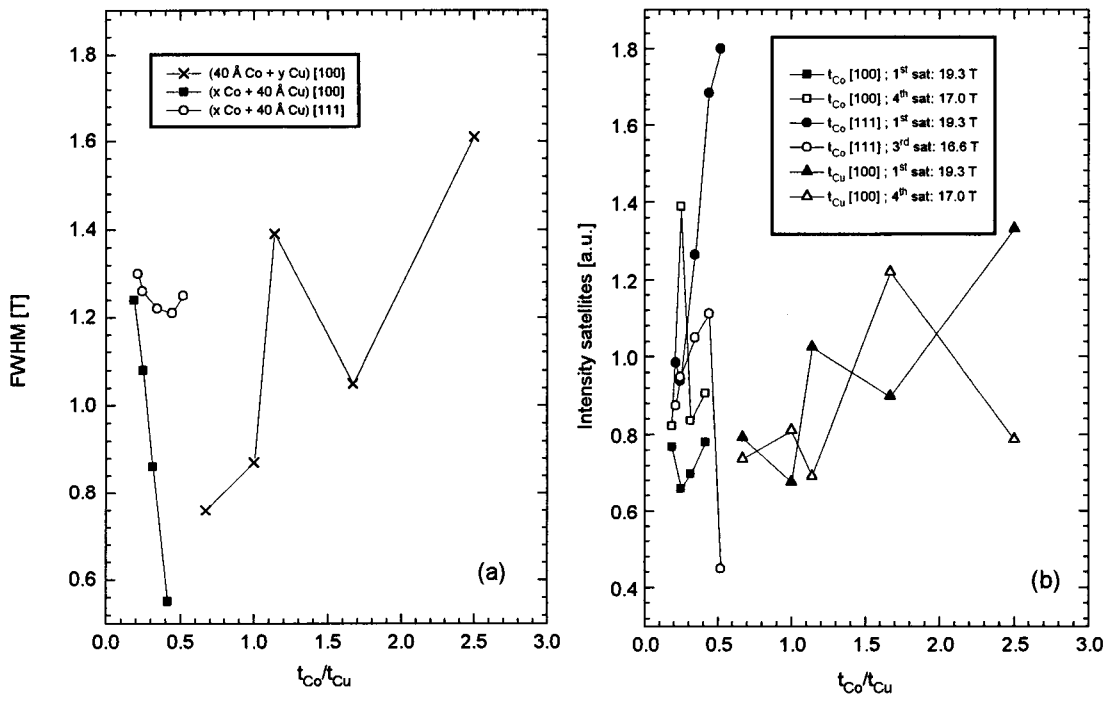


Figure 5.10: *In (a) the full width half maximum (FWHM) of fcc main lines of all three Co/Cu multilayer series as function of the ratio Co to Cu layer thickness ($t_{Co}/t_{Cu}$) is shown. In (b) the intensity of several satellite lines of several Co/Cu multilayer series (varying in $t_{Co}$, $t_{Cu}$, and texture) is plotted as function of $t_{Co}/t_{Cu}$.*

The assumption of a fourth satellite line at 16.6 T in case of the Co/Cu [100] multilayer is based on the result obtained by the 7000 Å Co film, grown in a Co-Cu bath and having an identical substrate Si(100) and base layer of 200 Å Cu. The few Co/Cu [100] multilayer NMR results earlier published by others in literature are ambiguous and are not to be relied on. However, this causes a dilemma, when we confirm the literature results with our own electrodeposited Co/Cu [111] multilayers in stating the third satellite at about 17 T. It implies two values for the average distance $\Delta$(sat) of successive satellite lines: 1.15±0.05 T in case of Co/Cu [100] multilayers (which is in accordance with our own 1.20±0.09 T obtained by a Co-Cu alloy, and 1.54±0.03 T in case of Co/Cu [111] multilayers (which is in accordance with the literature average of 1.5 T). The assumed dependence of $\Delta$(sat) upon the base layer, i.e. upon the difference in texture, remains unexplained.

The shape and position of the main peak of the samples show that the initial stacking of Co layers is fcc in presence of a presumably nnn-line causing the FWHM first to decrease with increasing $t_{Co}/t_{Cu}$ in case of the [100] series with varying $t_{Co}$, then be constant in case of the [111] series, and finally the FWHM increases with increasing $t_{Co}/t_{Cu}$ in case of [100] series with varying $t_{Cu}$. This increase in FWHM with increasing Co to Cu layer thickness

ratio is caused by the fact that growth favours the low-temperature stable hcp phase (due to the relatively small Cu layer thickness) through an increasing spin-echo intensity at hyperfine fields in the vicinity of stacking faults. Although each copper underlayer tends to reinitialize fcc growth, a fcc to hcp transformation already takes place in the first Co layer as observed in spin valves (one Co layer) by Panissod et al. [PM93]. The influence of repeating the Co/Cu layers should be investigated by measuring NMR spectra as function of the number of repetitions. As we have seen in the (15 Å Co + y Cu) [100] series, one can roughly state that a thicker Cu layer causes a better fcc growth in the Co layer.

The interface roughness for both [100] and [111] series is 5±1 Å Co per 2 interface layers. The absence of the perfect interface peak in thin multilayer samples is probably due to the various growth orientations, which result in fluctuations in the chemical coordination shells (according to Panissod et al. [PM93]) even if the interfaces are flat. The nature of the buffer layer deposited on the substrate prior to multilayer growth has a striking effect on the interface topology, as seen in the previous sections.

From their XRD data Lenczowski et al. [LSGdJ95] judged that Co/Cu multilayers electrodeposited on Cu base layers are comparable in quality to multilayers fabricated by sputtering, which is a commonly applied technique for the growth of magnetic multilayers.

The structural quality of the superlattice is reflected in the visibility of (especially) satellite peaks in the interface and/or widths of separate resonance lines, as we used before. Without brighteners, one is able to observe a smaller interface roughness and to distinguish more lines. The addition of triton-X100, and even more the addition thiourea, causes a "bluring" effect, i.e. showing a NMR spectrum with one peak having a large FWHM. This (partial) destruction of the superlattice stacking is also confirmed by XRD. The GMR of above-mentioned multilayers decreases from at least 3% (without leveling agent) to less than 1% (with leveling agent) [LSGdJ95] for similar Co/Cu multilayer configurations.

# Bibliography


[Abr61] A. Abragam. Principles of Nuclear Magnetism. *Oxford Univ. Press, London*, 1961.

[BBF+88] M.N. Baibich, J.M. Broto, A. Fert, F. Nguyen Van Dau, F. Petroff, P. Eitenne, G. Creuzet, A. Friederich, and J. Chazelas. Giant magnetoresistance of (001) Fe / (001) Cr magnetic superlattices. *Phys. Rev. Lett.*, 61(21):pp. 2472–2475, 1988.

[BF94] J. Barnas and A. Fert. Interfacial resistance for perpendicular transport in layered magnetic structures. *Phys. Rev. B*, 49(18):pp. 12835–12838, 1994.

[BGH+92] P. Boher, F. Giron, Ph. Houdy, F. Baudelet, A. Fontaine, J.M. Ladouceur, E. Dartyge, P. Beauvillain, C. Chappert, P. Veillet, and K. Le Dang. Direct experimental evidence of a body-centered-cubic Co phase in radio-frequency-sputtered Co/Fe multilayers. *J. Appl. Phys.*, 71(4):pp. 1798–1801, 1992.

[BH94] Editors: J.A.C. Bland and B. Heinrich. Ultrathin Magnetic Structures, Volume I and II. *Springer Verlag*, 1994. Berlin–Heidelberg.

[BHP46a] F. Bloch, W.W. Hansen, and M. Packard. Nuclear Induction. *Phys. Rev.*, 69:p. 127, 1946. (Letter to the Editor).

[BHP46b] F. Bloch, W.W. Hansen, and M. Packard. The Nuclear Induction Experiment. *Phys. Rev.*, 70(7 and 8):pp. 474–485, 1946.

[Blu21] W. Blum. The structure and properties of alternately electrodeposited metals. *Trans. Am. Electrochem. Soc.*, 40:pp. 307–320, 1921.

[BMDA94] A. Blondel, J.P. Meier, B. Doudin, and J.-Ph. Ansermet. Giant magnetoresistance of nanowires of multilayers. *Appl. Phys. Lett.*, 65(23):pp. 3019–3021, 1994.

[Boy63] E.L. Boyd. Temperature dependence of Nuclear Magnetic Resonance of $Fe^{57}$ in magnetite. *Phys. Rev.*, 129(5):pp. 1961–1964, 1963.

[BR89] P. Bruno and J.-P. Renard. Magnetic surface anisotropy of transition metal ultrathin films. *Appl. Phys. A*, 49:pp. 499–506, 1989.

[BS62] E.L. Boyd and J.C. Slonczewski. Anisotropy of the hyperfine interaction in magnetite. *J. Appl. Phys.*, 33(3):pp. 1077–1078, 1962.

[BW73] J.J. Bartel and E.F. Westrum. Dopant effects upon the Verwey transition in $Fe_3O_4$. In *AIP Conference Proceedings, Part Two: Magnetism and Magnetic Materials, 18th Annual Conference - Denver (1972)*, number 10, pages 1393–1397, 1973.

[CBT+94] R. Clarke, D. Barlett, F. Tsui, B. Chen, and C. Uher. An alternate route to giant magnetoresistance in MBE-grown Co-Cu-superlattices (invited). *Appl. Phys. Lett.*, 75(10):pp. 6174–6177, 1994.

[Col71] J.H.P. Colpa. Dipole fields and electric-field gradients in their dependence on the macroscopic and microscopic crystal parameters for orthorhombic and hexagonal lattices. I. *Physica*, 56:pp. 185–204, 1971.

[CR73] C. Constantin and M. Rosenberg. Electrical properties of pure and substituted magnetite from 4.2 to 300 K. In *AIP Conference Proceedings, Part Two: Magnetism and Magnetic Materials, 18th Annual Conference - Denver (1972)*, number 10, pages 1389–1392, 1973.

[dG93] H.A.M. de Gronckel. The nanostructure of multilayered films, a NMR study. 1993. Ph.D. thesis, Eindhoven University of Technology.

[dGBvAdJ94] H.A.M. de Gronckel, P.J.H. Bloemen, E.A.M. van Alphen, and W.J.M. de Jonge. Structure and local magnetic anisotropy of MBE-grown Co films. *Phys. Rev. B*, 49(16):pp. 11327–11335, 1994.

[dGdJ92] H.A.M. de Gronckel and W.J.M. de Jonge. NMR studies on magnetic multilayers. *internal report*, 1992. Eindhoven University of Technology.

[dGKdJ+91] H.A.M. de Gronckel, K. Kopinga, W.J.M. de Jonge, P. Panissod, J.P. Schillé, and F.J.A. den Broeder. Nanostructure of Co/Cu multilayers. *Phys. Rev. B*, 44(16):pp. 9100–9103, 1991.

[Die94] B. Dieny. Giant magnetoresistance in spin-valve multilayers. *J. Magn. Magn. Mat.*, 136:pp. 335–359, 1994.

[DJML93] J. Dekoster, E. Jedryka, C. Mény, and G. Langouche. Epitaxial growth of bcc Co/Fe superlattices. *J. Magn. Magn. Mat.*, 121:pp. 69–72, 1993.

[DMI+81] A.I. Drokin, T.N. Metlyaev, A.V. Ivanova, G.N. Abelyashev, V.N. Shcherbakov, A.A. Shemyakov, and L.P. Chervenchuk. Effect of magnetostructural changes on the Barkhausen Effect in ferrospinels containing cobalt. *Proceedings of the Second All-Union Seminar on the Barkhausen Effect*, 45(9):pp. 1631–1634, 1981. Izvestiya Akademii Nauk SSSR, Seriya Fizicheskaya.

[DU70] R.H. Dean and R.J. Urwin. The use of nuclear spin-echoes to measure hyperfine field distributions in ferromagnets. *J. Phys. C: Sol. State Phys.*, 3:pp. 1747–1752, 1970.

[DV90] K. Le Dang and P. Veillet. NMR study of interface structure in epitaxial Co/Cu superlattices. *Phys. Rev. B*, 41(18):pp. 12902–12904, 1990.

[DVBC91] K. Le Dang, P. Veillet, P. Beauvillain, and C. Chappert. NMR and magnetization studies of Co/Cu superlattices. *Phys. Rev. B*, 43(16):pp. 13228–13231, 1991.

[DVV+93] K. Le Dang, P. Veillet, E. Velu, S.S.P. Parkin, and C. Chappert. Influence of crystal structure on the magnetoresistance of Co/Cu multilayers. *Appl. Phys. Lett.*, 63(1):pp. 108–110, 1993.

[Fer30] E. Fermi. Ueber die magnetischen Momente der Atomkerne. *Zeit. f. Physik*, 60:pp. 320–333, 1930.

[FGS+76] D. Fekete, A. Grayevskey, D. Shaltiel, U. Goebel, E. Dormann, and N. Kaplan. Test for band ferromagnetism in hcp cobalt: Knight Shift in the ferromagnetic phase of cobalt. *Phys. Rev. Lett.*, 36:pp. 1566–1569, 1976.

[FTK+90a] T. Fujii, M. Takano, R. Katano, Y. Bando, and Y. Isozumi. CEMS study of the growth and properties of $Fe_3O_4$ films. *J. Crystal Growth*, 99:pp. 606–610, 1990.

[FTK+90b] T. Fujii, M. Takano, R. Katano, Y. Bando, and Y. Isozumi. Depth selective Mössbauer spectroscopic study of $Fe_3O_4$ epitaxial films. *J. Appl. Phys.*, 68(4):pp. 1735–1740, 1990.

[FTK+94] T. Fujii, M. Takano, R. Katano, Y. Isozumi, and Y. Bando. Surface and interface properties of epitaxial $Fe_3O_4$ films studied by Mössbauer spectroscopy. *J. Magn. Magn. Mat.*, 130:pp. 267–274, 1994.

[GBDV92] F. Giron, P. Boher, K. Le Dang, and P. Veillet. Microscopic evidence for pseudo-epitaxy in fcc (100) Co/Cu multilayers. *J. Phys. Cond. Mat.*, 4:pp. L425–L428, 1992. (Letter to the Editor).

[GBH+93] F. Giron, P. Boher, Ph. Houdy, P. Beauvillain, K. Le Dang, and P. Veillet. Growth and structure of fcc (100) Co/Cu and Fe/Cu multilayers. *J. Magn. Magn. Mat.*, 121:pp. 24–29, 1993.

[GP59] A.C. Gossard and A.M. Portis. Observation of Nuclear Resonance in a ferromagnet. *Phys. Rev. Lett.*, 3(4):pp. 164–166, 1959.

[GSP+86] P. Grünberg, R. Schreiber, Y. Pang, M.B. Brodsky, and H. Sowers. Layered magnetic structures: Evidence for antiferromagnetic coupling of Fe layers across Cr interlayers. *Phys. Rev. Lett.*, 57(19):pp. 2442–2445, 1986.

[HCR92] A. Haseeb, J.P. Celis, and J.R. Roos. *Trans. Metal finish Assoc. India*, (I):pp. 15–28, 1992.

[IMM+82] S. Iida, K. Mizushima, M. Mizoguchi, K. Kose, K. Kato, K. Yanai, N. Goto, and S. Yumoto. Details of the electronic superstructure of $Fe_3O_4$. *J. Appl. Phys.*, 53(3):pp. 2164–2166, 1982.

[IMU+80] S. Iida, M. Mizoguchi, S. Umemura, J. Yoshida, K. Kato, and K. Yanai. Study of the low temperature phase of $Fe_3O_4$. *J. Magn. Magn. Mat.*, 15–18:pp. 997–998, 1980.

[Jan79] J.F. Janak. Calculated hyperfine fields and their pressure derivatives in Fe, Co, and Ni. *Phys. Rev. B*, 20(5):pp. 2206–2208, 1979.

[KAI66] S. Kobayashi, K. Asayama, and J. Itoh. Nuclear Magnetic Resonance in Co alloys. *J. Phys. Soc. Jpn.*, 21(1):pp. 65–74, 1966.

[Kaw76] M. Kawakami. $Co^{59}$ NMR in hexagonal cobalt-base dilute alloys with 3d transition metals. *J. Phys. Soc. Jpn.*, 40(1):pp. 56–62, 1976.

[KB76] A.J.M. Kuipers and V.A.M. Brabers. Thermoelectric properties of magnetite at the Verwey transition. *Phys. Rev. B*, 14(4):pp. 1401–1405, 1976.

[KB79] A.J.M. Kuipers and V.A.M. Brabers. Electrical transport in magnetite near the Verwey transition. *Phys. Rev. B*, 20(2):pp. 594–600, 1979.

[KKPS82] N.M. Kovtun, A.M. Kotel'va, A.K. Prokopenko, and A.A. Shemyakov. Nuclear Magnetic Resonance of $^{59}Co$ and valence states of ions in cobalt ferrite. *Sov. Phys. - Sol. State*, 24(1):p. 185, 1982.

[KS73a] N.M. Kovtun and A.A. Shamyakov. $Fe^{57}$ NMR spectra in magnetite. *Sol. State Comm.*, 13(9):pp. 1345–1349, 1973.

[KS73b] N.M. Kovtun and A.A. Shemyakov. Nuclear Magnetic Resonance spectra of $Fe^{57}$ in magnetite in the region of a magnetic phase transition. *Sov. Phys. - Sol. State*, 15(5):pp. 1093–1094, 1973.

[KSS73] N.M. Kovtun, E.E. Solov'ev, and A.A. Shemyakov. NMR investigation of electron ordering in magnetite. *Sov. Phys. - Sol. State*, 14(9):pp. 2430–2431, 1973.

[LBC+92] D.M. Lind, S.D. Berry, G. Chern, H. Mathias, and L.R. Testardi. Growth and structural characterization of $Fe_3O_4$ and NiO thin films and superlattices grown by oxygen-plasma-assisted molecular-beam-epitaxy. *Phys. Rev. B*, 45(4):pp. 1839–1850, 1992.

[LKRW93] J.S. Lord, H. Kubo, P.C. Riedi, and M.J. Walker. Nuclear Magnetic Resonance of molecular beam epitaxially grown Co/Cu superlattices that exhibit large magnetoresistance. *J. Appl. Phys.*, 73(10):pp. 6381–6383, 1993.

[LSGdJ95] S.K.J. Lenczowski, C. Schönenberger, M.A.M. Gijs, and W.J.M. de Jonge. Giant magnetoresistance of electrodeposited Co/Cu multilayers. *J. Magn. Magn. Mat.*, 148:pp. 455–465, 1995.

[Lui93] S.B. Luitjens. Magnetische registratie met hoge informatiedichtheden. *Nederlands Tijdschrift voor Natuurkunde*, pages 241–246, (nr. 15) 1993.

[Met95] J.M. Metselaar. Electrodepositie van magnetische multilagen: Ontwerp van opstelling. *internal report*, April 1995. Eindhoven University of Technology.

[MI66] T. Mizoguchi and M. Inoue. Nuclear Magnetic Relaxation in magnetite. *J. Phys. Soc. Jpn.*, 21(7):pp. 1310–1323, 1966.

[MI80] M. Mizoguchi and S. Iida. Characters of the hyperfine fields of $Fe^{3+}$ and $Fe^{2+}$ as seen from the NMR of the low temperature phase of $Fe_3O_4$. *Ferrites: Proc. of the Int. Conf. (Japan)*, pages 149–152, September–October 1980.

[Miz78a] M. Mizoguchi. NMR study of the low temperature phase of $Fe_3O_4$. I. experiments. *J. Phys. Soc. Jpn.*, 44(5):pp. 1501–1511, 1978.

[Miz78b] M. Mizoguchi. NMR study of the low temperature phase of $Fe_3O_4$. II. electron ordering analysis. *J. Phys. Soc. Jpn.*, 44(5):pp. 1512–1520, 1978.

[Miz85a] M. Mizoguchi. Abrupt change of NMR line shape in the low temperature phase of $Fe_3O_4$. *J. Phys. Soc. Jpn.*, 54(11):pp. 4295–4299, 1985.

[Miz85b] M. Mizoguchi. Structure of $Fe_3O_4$ in the low temperature phase as deduced from advanced analysis of the NMR study. *J. Phys. Soc. Jpn.*, 54(6):pp. 2168–2183, 1985.

[MJP+93a] C. Mény, J.P. Jay, P. Panissod, P. Humbert, V.S. Speriosu, H. Lefakis, J.P. Nozières, and B.A. Gurney. Annealed Cu/Co/Cu/NiFe/FeMn spin valves: nanostructure and magnetism. *Mat. Res. Soc. Symp. Proc.*, 313:pp. 289–294, 1993.

[MJP93b] C. Mény, E. Jedryka, and P. Panissod. Satellite structure of $^{59}Co$ NMR spectra in some Co alloys. *J. Phys. Cond. Mat.*, 5:pp. 1547–1556, 1993.

[MPB94] D.T. Margulies, F.T. Parker, and A.E. Berkowitz. Magnetic anomalies in single crystal $Fe_3O_4$ films. *J. Appl. Phys.*, 75(10):pp. 6097–6099, 1994.

[MPH+93] C. Mény, P. Panissod, P. Humbert, J.P. Nozières, V.S. Speriosu, and B.A. Gurney. Structural study of Cu/Co/Cu/NiFe/FeMn spin valves by Nuclear Magnetic Resonance. *J. Magn. Magn. Mat.*, 121:pp. 406–408, 1993.

[MPL92] C. Mény, P. Panissod, and R. Loloee. Structural study of cobalt-copper multilayers by NMR. *Phys. Rev. B*, 45(21):pp. 12269–12277, 1992.

[MS93] S.K. Mishra and S. Satpathy. Energetic stabilization of the Mizoguchi structure for magnetite by band-structure effects. *Phys. Rev. B*, 47(10):pp. 5564–5570, 1993.

[MT65] T. Mizoguchi and Y. Tomono. Nuclear Magnetic Relaxation in magnetite. *J. Appl. Phys.*, 36, Part Two(3):pp. 1020–1021, 1965.

[NSS+93] H. Nakamura, T. Suzuki, M. Shiga, H. Yamamoto, and T. Shinjo. NMR study of $^{59}Co$ in [Cu/Co/Cu/NiFe] superlattices. *J. Magn. Magn. Mat.*, 126:pp. 364–366, 1993.

[NYNM74] S. Nasu, H. Yasuoka, Y. Nakamura, and Y. Muraki. Hyperfine field distribution in Co-Cu alloy: $^{59}Co$ Nuclear Magnetic Resonance. *Acta Metallurgica*, 22:pp. 1057–1063, 1974.

[OM62] S. Ogawa and S. Morimoto. Nuclear Magnetic Resonance of $Fe^{57}$ in various ferrimagnetic oxides. *J. Phys. Soc. Jpn.*, 17(4):pp. 654–659, 1962.

[Pan86] P. Pannisod. Microscopic methods in metals. *Topics in Current Physics*, (chapter 12: Nuclear Magnetic Resonance), 1986. Editor: U. Gonser.

[PGD+94] L. Piraux, J.M. George, J.F. Despres, C. Leroy, E. Ferain, R. Legras, K. Ounadjela, and A. Fert. Giant magnetoresistance in magnetic multilayered nanowires. *Appl. Phys. Lett.*, 65(19):pp. 2484–2486, 1994.

[PJM65] G.J. Perlow, C.E. Johnson, and W. Marshall. Mössbauer Effect of $Fe^{57}$ in a cobalt single crystal. *Phys. Rev.*, 140(3A):pp. 875–879, 1965.

[PLH+93] W.P. Pratt, S.-F. Lee, P. Holody, R. Loloee, J. Bass, and P.A. Schroeder. Giant magnetoresistance with current perpendicular to the multilayer plane. *J. Magn. Magn. Mat.*, 126:pp. 406–409, 1993.

[PLS91] S.S.P. Parkin, Z.G. Li, and D.J. Smith. Giant magnetoresistance in antiferromagnetic Co/Cu multilayers. *Appl. Phys. Lett.*, 58(23):pp. 2710–2712, 1991.

[PM93] P. Panissod and C. Mény. NMR investigations of the nanostructure of ../Cu/Co/Cu/... layers. *J. Magn. Magn. Mat.*, 126:pp. 16–18, 1993.

[PMR90] S.S.P. Parkin, N. More, and K.P. Roche. Oscillations in Exchange Coupling and Magnetoresistance in metallic superlattice structures: Co/Ru, Co/Cr, and Fe/Cr. *Phys. Rev. Lett.*, 64(19):pp. 2304–2307, 1990.

[Pri95] G.A. Prinz. Spin-Polarized Transport. *Physics Today*, pages 58–63, April 1995.

[PTP46] E.M. Purcell, H.C. Torrey, and R.V. Pound. Resonance Absorption by nuclear magnetic moments in a solid. *Phys. Rev.*, 69:pp. 37–38, 1946. (Letter to the Editor).

[RBD+92] J.P. Renard, P. Beauvillain, C. Dupas, K. Le Dang, P. Veillet, and E. Vélu. Large magnetoresistance effects in UHV grown fcc (111) Co/Cu multilayers. *J. Magn. Magn. Mat.*, 115:pp. L147–L151, 1992. (Letter to the Editor).

[RCdB91] J.R. Roos, J.P. Celis, and M. de Bonte. Materials Science and Technology. VCII(15):pp. 148–534, 1991.

[RDR+87] P.C. Riedi, T. Dumelow, M. Rubinstein, G.A. Prinz, and S.B. Qadri. Hyperfine-field spectrum of epitaxially grown bcc cobalt. *Phys. Rev. B*, 36(9):pp. 4595–4599, 1987.

[RF71] M. Rubinstein and D.W. Forester. Investigation of the insulating phase of magnetite by NMR and the Mössbauer effect. *Sol. State Comm.*, 9(19):pp. 1675–1679, 1971.

[RMB83] M.O. Rigo, J.F. Mareche, and V.A.M. Brabers. On the phase transition(s) of magnetite at low temperatures. *Phil. Mag. B*, 48(5):pp. 421–430, 1983.

[RMKZ39] I.I. Rabi, S. Millman, P. Kusch, and J.R. Zacharias. The Molecular Beam Resonance Method for measuring nuclear magnetic moments (The magnetic moments of $_3Li^6$, $_3Li^7$, and $_9F^{19}$). *Phys. Rev.*, 55:pp. 526–535, 1939.

[RS73] M. Rubinstein and G.H. Stauss. Hyperfine field spectra of magnetite ($Fe_3O_4$). In *AIP Conference Proceedings, Part Two: Magnetism and Magnetic Materials, 18th Annual Conference - Denver (1972)*, number 10, pages 1384–1388, 1973.

[SdGG+94] F. Schreiber, H.A.M. de Gronckel, I.A. Garifullin, P.Bödeker, K. Bröhl, and J. Pelzl. Ferromagnetic and Nuclear Magnetic Resonance studies of Co/Cu(111) superlattices: anisotropy and structural properties. *J. Magn. Magn. Mat.*, 148:pp. 152–153, 1994.

[SKY92] Y. Suzuki, T. Katayama, and H. Yasuoka. NMR study of fcc Co/Cu (100) and (111) artificial superlattices. *J. Magn. Magn. Mat.*, 104–107:pp. 1843–1844, 1992.

[Sli78] P. Slichter. Principles of Magnetic Resonance. *Springer-Verlag, Berlin*, 1978. Editors: M. Cardona, P. Fulde, and H.J. Queisser.

[Smi92] J. Smits. Magnetic Multilayers. *Physical World*, pages 48–53, November 1992.

[SMY+87] Y. Suzuki, H. Masuda, M. Yamazaki, K. Takanashi, and H. Yasuoka. Structural and NMR studies of highly oriented Co/Cu artificial superlattices. *Proc. Int. Symp. on Physics of Magn. Mat.*, pages 259–262, April 1987. World Scientific; Sendai, Japan.

[SNG+93] V.S. Speriosu, J.P. Nozieres, B.A. Gurney, B. Dieny, T.C. Huang, and H. Lefakis. Role of interfacial mixing in giant magnetoresistance. *Phys. Rev. B*, 47(17):pp. 11579–11582, 1993.

[STGY93] M. Suzuki, Y. Taga, A. Goto, and H. Yasuoka. The critical thickness of Fe buffer layer in giant magnetoresistance of Co/Cu superlattices. *J. Magn. Magn. Mat.*, 126:pp. 495–497, 1993.

[SvN94] R. Smeets and F. van Nijmweegen. User manual PhyBUS Analog Signal Recorder. *internal report*, (Physical & Technical Laboratory Automation Group), September 1994. Eindhoven University of Technology.

[TB87] T. Terashima and Y. Bando. Formation and magnetic properties of artificial superlattice of CoO-$Fe_3O_4$. *Thin Sol. Films*, pages pp. 455–463, 1987.

[TKL+94] T. Thomson, H. Kubo, J.S. Lord, P.C. Riedi, and M.J. Walker. Field dependence of NMR in MBE grown Co(111)/Cu multilayers. *J. Appl. Phys.*, 76(10):pp. 6504–6506, 1994.

[TM92] K. Takei and Y. Maeda. NMR study on compositional distribution in sputter-deposited Co-Ni thin films. *Jpn. J. Appl. Phys.*, 74(9A):pp.2734–2735, 1992.

[TOY74] T. Tsuda, K. Okada, and H. Yasuoka. Hyperfine field distribution of $Co^{2+}$ ions in Co-Ferrite – $Co^{59}$ NMR. *J. Phys. Soc. Jpn.*, 37:p. 1713, 1974.

[TPP46] H.C. Torrey, E.M. Purcell, and R.V. Pound. B8. Theory of Magnetic Resonance Absorption by nuclear moments in solids. *Phys. Rev.*, 69:p. 681, 1946.

[TRG94] T. Thomson, P.C. Riedi, and D. Greig. Interfacial quality and giant magnetoresistance in MBE-grown Co/Cu(111) superlattices. *Phys. Rev. B*, 50(14):pp. 10319–10322, 1994.

[tV93] S.G.E. te Velthuis. Structural characteristics of Co/Ni, Co/Ag, and Co/Cu multilayers measured with Nuclear Magnetic Resonance. *internal report*, June 1993. Eindhoven University of Technology.

[vAdGB+93] E.A.M. van Alphen, H.A.M. de Gronckel, P.J.H. Bloemen, A.S. van Steenbergen, and W.J.M. de Jonge. Structural dependence of the magnetic anisotropy of Co films. *J. Magn. Magn. Mat.*, 121:pp. 77–78, 1993.

[vAtVdG+94] E.A.M. van Alphen, S.G.E. te Velthuis, H.A.M. de Gronckel, K. Kopinga, and W.J.M. de Jonge. NMR study of the strain in Co-based multilayers. *Phys. Rev. B*, 49(24):pp. 17336–17341, 1994.

[vdH94] P.A.A. van der Heijden. Coherent NMR measurements on as-deposited and annealed Co/Ni, Co/Ag multilayers. *internal report*, April 1994. Eindhoven University of Technology.

[VGJ+93] T. Valet, P. Galtier, J.C. Jacquet, C. Mény, and P. Panissod. Correlation between giant magnetoresistance and the microstructure of [$Ni_{80}Fe_{20}$/Cu/Co] multilayers. *J. Magn. Magn. Mat.*, 121:pp. 402–405, 1993.

[VH41] E. J. W. Verwey and P. W. Haayman. Electronic conductivity and transition point of magnetite ("$Fe_3O_4$"). *Physica*, VIII(9):pp. 979–987, 1941. Erratum 1085.

[vS92] A.S. van Steenbergen. Kernspinresonantie aan 1000 Å Co-films en Co/X (X = Ag, Cu, Mn, V) multilagen. *internal report*, June 1992. Eindhoven University of Technology.

[Wij80] Editor: H.P.J. Wijn. Numerical data and functional relationships in Science and Technology. *Landolt-Börnstein New Series III/19a*, 1980. Editors in Chief: K.-H. Hellwege and O. Madelung; Springer Verlag.

[WWJ67] R.E. Walstedt, J.H. Wernick, and V. Jaccarino. New determination of the nuclear gyromagnetic ratio $\gamma$ of $Co^{59}$. *Phys. Rev.*, 162(2):pp. 301–311, 1967.

[YMI81] K. Yanai, M. Mizoguchi, and S. Iida. Temperature dependence of NMR of magnetite at about 10 K. *J. Phys. Soc. Jpn.*, 50(1):pp. 65–69, 1981.

[ZSP90] J.M. Zuo, J.C.H. Spence, and W. Petuskey. Charge ordering in magnetite at low temperatures. *Phys. Rev. B*, 42(13):pp. 8451–8464, 1990.

# Appendix A

# Reflection as a function of frequency

In the now following figure, the reflection is plotted as a function of the frequency obtaining the NMR spectrum of magnetite sample SP698 at 4.2 K.

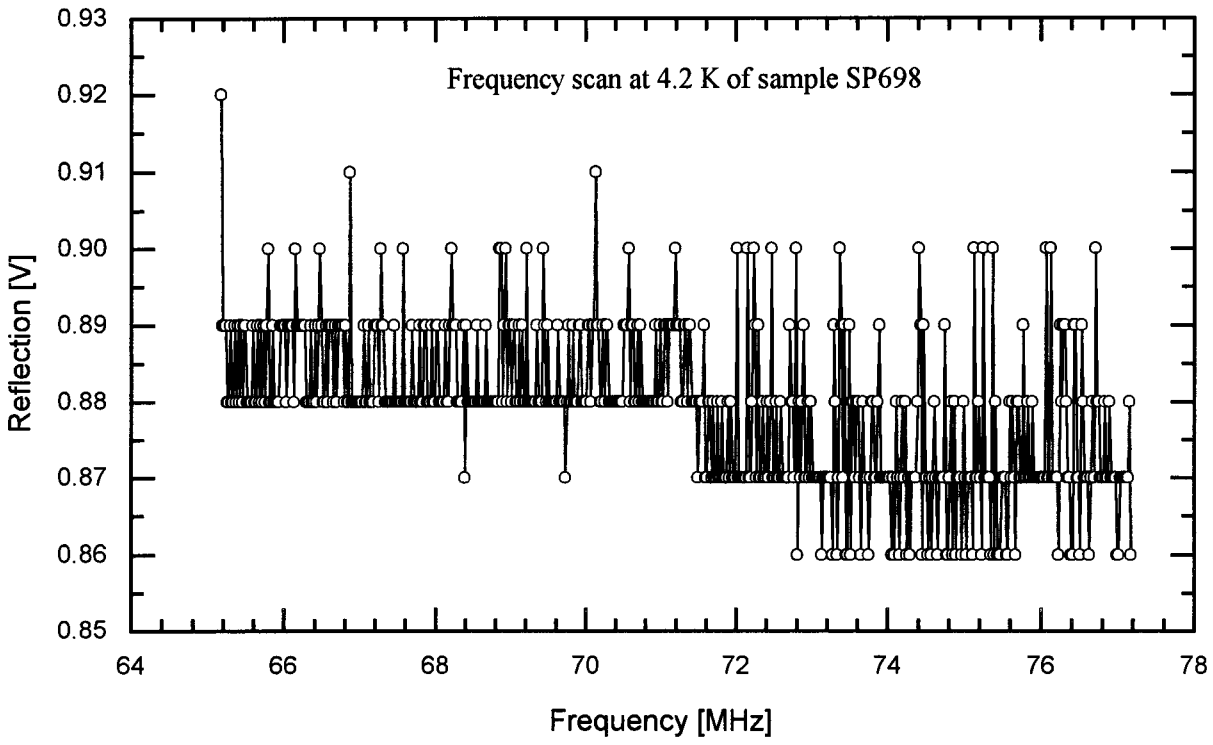


Figure A.1: *Frequency dependence of reflection.*